Doctoral theses at NTNU, 2023:333

Ruben Løland Sælen

Mechanical behaviour and material modelling of an additively manufactured polymer

Doctoral thesis

NTNU
Norwegian University of Science and Technology
Thesis for the Degree of Philosophiae Doctor
Faculty of Engineering
Department of Structural Engineering

NTNU
Norwegian University of Science and Technology

Ruben Løland Sælen

Mechanical behaviour and material modelling of an additively manufactured polymer

Thesis for the Degree of Philosophiae Doctor

Trondheim, October 2023

Norwegian University of Science and Technology
Faculty of Engineering
Department of Structural Engineering

NTNU
Norwegian University of
Science and Technology

NTNU
Norwegian University of Science and Technology

Thesis for the Degree of Philosophiae Doctor

Faculty of Engineering
Department of Structural Engineering

ISBN 978-82-326-7366-7 (printed ver.)
ISBN 978-82-326-7365-0 (electronic ver.)
ISSN 1503-8181 (printed ver.)
ISSN 2703-8084 (online ver.)

Doctoral theses at NTNU, 2023:333

Printed by NTNU Grafisk senter

Preface

This thesis is submitted in partial fulfilment of the degree Philosophiae Doctor (PhD) in Structural Engineering at the Norwegian University of Science and Technology (NTNU). The work has been conducted at the research group Structural Impact Laboratory (SIMLab) at the Department of Structural Engineering, under the supervision of Professor Arild Holm Clausen and Professor Odd Sture Hopperstad.

The research project has been financed partially by the Centre for Advanced Structural Analysis (CASA), a Centre for Research-based Innovation (CRI) hosted by the Department of Structural Engineering and partially by the Faculty of Engineering at the Norwegian University of Science and Technology.

The thesis is written as a monograph.

The author has been responsible for the experimental work, constitutive modelling, numerical work and the writing of this thesis.

Ruben Løland Sælen
Trondheim, Norway
July, 2023

Abstract

This thesis presents the characterisation and constitutive modelling of the mechanical behaviour of a commercial additively manufactured polymer produced with the stereolithography process. The first part of the characterisation procedure consisted of an extensive experimental campaign carried out to provide experimental data for use in the calibration and validation of a constitutive model. The material was studied through tensile and compression tests on smooth and notched axisymmetric specimens. The tests revealed the material to be practically isotropic and to have a strain-rate- and pressure-dependent yield stress. Test specimens failed in tension with a brittle fracture mode, yet the surface logarithmic strains measured with DIC before fracture exceeded 0.4 in all cases. After testing, hardly any permanent deformations were observed which indicates that the mechanical response is primarily viscoelastic. In addition to the tensile and compression tests, tests were performed on more complex 3D-printed structures to provide validation data for the constitutive model implemented as part of this thesis. The first validation test series consisted of quasi-static and dynamic compression tests of octet-strut lattice structures. The results from the quasi-static tests showed the same strain-rate sensitivity as the tensile tests, while the dynamic tests exhibited an extremely brittle failure mode due to the high strain rates. The second validation test series consisted of three-point bending tests of notched beams with two different notch radii. These tests did not reveal anything new about the mechanical behaviour of the material but provided experimental data with more complex stress states than the tension and compression tests.

Based on the experimental results, a constitutive model was formulated and implemented as a user-material in the finite element solver Abaqus/Explicit. The model is hyper-viscoelastic and formulated for large strains using a multiplicative split of the deformation gradient. A stress-based fracture initiation model with stochastic critical stress was employed to model the brittle fracture mode observed in the experiments. The implemented constitutive model was verified by investigating its behaviour in single-element simulations at various stress- and strain states. The model was then calibrated to the experimental results from the tension and compression tests by an inverse modelling approach. The model was able to capture the stress-strain response from the experiments as well as predict the fracture initiation. The validation tests were then simulated with the calibrated material model.

Simulations of the quasi-static octet-strut lattice structures agreed well with the experimental results. Both the force-displacement curves and deformation modes were captured by the model. Simulations of the dynamic lattice compression tests revealed that the combination of a stress-based fracture criterion and the non-linear viscoelasticity of the model was able to predict the same brittle behaviour seen in the experiments. Simulations of the three-point bending tests captured the experimental trends, but the force at yield was underestimated for both specimen types which led to fracture occurring too late. Fracture propagation was not accurately captured by the fracture model as the simulated crack paths were heavily mesh dependent and did not match the experimental results.

Acknowledgements

I would like to start by thanking my supervisors Professor Arild Holm Clausen and Professor Odd Sture Hopperstad for their guidance and support. I'm grateful for the balance of independence and supervision you have provided me these four years.

The experimental work carried out in this work could not have been done without the invaluable help from Trond Auestad. I would also like to thank Dr Torodd Berstad for always being available to answer any questions I might have about constitutive modelling and its numerical aspects. Special thanks go to Dr Petter Holmström for his guidance and support during my research stay at Equinor and for his encouragement during the final stretch of my PhD journey.

My sincerest thanks go to my colleagues and friends at the SIMLab research group for making these last four years enjoyable – both at the office and outside. Though this PhD project hasn't been without its share of hardships, I believe I will always look back at this part of my life fondly thanks to you all. I would particularly like to thank my long-time office mate, and later office neighbour, Jonas Rudshaug for all the valuable discussions we've had and for sharing my dark sense of humour.

Lastly, I would like to thank my family and friends for their encouragement and support over the years.

Contents

Preface **i**

Abstract **iv**

Acknowledgements **v**

1 Introduction **1**
1.1 Background and motivation 1
1.2 Objectives 5
1.3 Scope 5
1.4 Research strategy 6
1.5 Outline of thesis 6
1.6 Contributions 7

2 Theory **9**
2.1 Continuum mechanics 9
2.1.1 Deformation 9
2.1.2 Deformation rates 13
2.1.3 Stress measures 15
2.1.4 Balance laws 17
2.1.5 The second law of thermodynamics 21
2.2 Hyperelasticity 23

3 Material tests **27**
3.1 Material and specimen preparation 27
3.2 Experimental programme 29
3.3 Experimental setup 30
3.4 Processing of results 31
3.4.1 Calculation of stress and strain 31
3.4.2 Temperature measurements 33
3.5 Results 34
3.5.1 Anisotropy and general behaviour 34
3.5.2 Strain-rate dependence 36
3.5.3 Unloading 37
3.5.4 Relaxation 40

3.5.5 Pressure sensitivity . . . 41
3.6 Summary . . . 44

4 Validation tests **45**
4.1 Lattice structure compression tests . . . 45
4.1.1 Experimental programme and setup . . . 45
4.1.2 Results and discussion . . . 50
4.2 Three-point-bending tests . . . 56
4.2.1 Experimental programme and setup . . . 56
4.2.2 Results and discussion . . . 57
4.3 Summary . . . 60

5 Constitutive model: Formulation **61**
5.1 Overview . . . 61
5.2 Part A . . . 63
5.3 Part B . . . 65
5.4 Fracture initiation model . . . 69
5.5 Numerical implementation . . . 72
5.6 Summary . . . 75

6 Constitutive model: Verification **77**
6.1 Simulation procedures . . . 77
6.1.1 Single-element simulations . . . 77
6.1.2 Multi-element simulations . . . 80
6.2 Behaviour of the hyper-viscoelastic model . . . 80
6.2.1 Uniaxial tension . . . 81
6.2.2 Uniaxial compression . . . 86
6.2.3 Simple shear . . . 90
6.2.4 Hydrostatic tension and compression . . . 94
6.2.5 Multi-element torsion-tension simulation . . . 94
6.2.6 Parametric study . . . 96
6.3 Behaviour of the fracture initiation model . . . 101
6.3.1 Fracture energy release . . . 101
6.3.2 Critical stress . . . 103
6.3.3 Assignment mesh . . . 105
6.4 Summary . . . 107

7 Constitutive model: Calibration **109**
7.1 Calibration procedure . . . 109
7.2 Finite element models . . . 109
7.3 Hyper-viscoelastic parameters . . . 112
7.4 Fracture parameters . . . 115

7.5 Numerical investigations . . . 121
7.5.1 The effects of symmetric boundary conditions . . . 121
7.5.2 The effect of mount-eccentricity in the notch compression tests . . . 122
7.6 Summary . . . 124

8 Constitutive model: Validation **127**
8.1 Simulation of the lattice structure compression tests . . . 127
8.1.1 Finite element model . . . 127
8.1.2 Results and discussion . . . 130
8.2 Simulation of the three-point-bending tests . . . 139
8.2.1 Finite element models . . . 139
8.2.2 Results and discussion . . . 142
8.3 Summary . . . 147

9 Conclusions and outlook **149**
9.1 Conclusions . . . 149
9.2 Suggestions for further work . . . 151

Contents

1 Introduction

1.1 Background and motivation

Additive manufacturing (AM), commonly referred to as 3D printing, is the process of creating a physical object from a digital 3D model, typically by joining together multiple thin layers of material. Though the technology has been around since the 80s, it did not see widespread use until the last decade when several patents entered the public domain. This opened the way for commercial 3D printers – popularising AM and pushing the technology further. Consequently, AM has now become an important tool for both industrial and research applications. Out of the different materials applicable to AM, polymers are the most widespread due to their price and ease of handling. Other materials include metals, ceramics and even concrete. In the industry, the main application of AM polymers is rapid prototyping, though AM has also seen use in the manufacture of bespoke parts with complex geometry that would be challenging to produce with traditional methods. In research, one particular topic that has been made easier to study due to AM is that of micro-architectured materials [1]. The precision offered by state-of-the-art polymer 3D printers allows the production of tailor-made cellular materials that offer mechanical properties – such as strength and stiffness – comparable to, or even surpassing, foams with similar densities. Such materials are also relevant for industrial applications, as they allow for lightweight but strong structures.

Of the polymer AM technologies, vat photo-polymerisation (VPP) lends itself the most to the manufacture of complex geometries due to the high accuracy and dimensional stability offered by 3D printers using said technology. VPP encompasses multiple 3D printing techniques which all utilise ultraviolet (UV) radiation to selectively cure photo-polymeric resins and as of 2020 holds the largest market share among AM polymers [2]. Examples of VPP techniques are stereolithography (SLA), digital light processing (DLP) and continuous liquid interphase printing (CLIP). Of the aforementioned techniques, SLA is the most popular as of 2021 [3] and a polymer produced with this method is the topic of this thesis.

Parts produced with SLA have a smooth surface finish and can feature very fine details due to the accuracy of the printing process. Mechanically the parts

can be considered isotropic due to the presence of cross-links both between and within the print layers. However, the print speed of SLA is relatively slow when compared with other 3D printing technologies.

The principles of SLA 3D printing are illustrated in Figure 1.1. During a print, a build platform is submerged in a resin tank until a gap corresponding to the print layer thickness is left between the bottom of the resin tank and the build platform. A UV laser then selectively cures the resin between the resin tank and print platform by reflecting off a programmable scanning mirror. Once the layer is cured, the print bed is elevated – creating a gap between the resin tank and the previous layer, which again is cured by the laser. This process is repeated until a full 3D object is formed.

Before printing, the 3D object needs to be drawn digitally using CAD or digital sculpting software. The 3D model then needs to be divided into print layers and translated into code understood by the 3D printer, which is done through an appropriate *slicing* software. The slicing process also assigns support structures to the 3D object to reduce the warping of overhangs in the print. After the print, any excess uncured resin is washed away by cleaning the printed part in an isopropyl alcohol (IPA) bath. The final part of the SLA 3D print process is to cure the parts in a tempered UV chamber to further improve the mechanical properties of the photopolymer. The entire SLA workflow is illustrated in Figure 1.2.

Polymers formed by SLA are *thermosetting glassy polymers*. Thermosetting polymers, or thermosets, are polymers where long polymer chains are connected by shorter cross-links. The interconnectivity of the polymer chains caused by the cross-links makes thermosets stiffer and stronger than thermoplastics but at the cost of lower ductility [4]. Perhaps the most defining trait of thermosets is that they do not melt but instead burn, which is in contrast to thermoplastics that can be melted and recycled. Glassy polymers are polymers with an amorphous non-crystalline molecular structure that have a *glass transition temperature*, T_g, higher than room temperature. Such polymers are in a glassy state in which relative sliding between polymer chains is restricted. The restricted motions of the polymer chains result in stiff, but brittle polymers.

When it comes to the application of SLA 3D printing to the production of functional, load-carrying parts, the mechanical properties of the chosen material are important. Knowing how to accurately predict the stiffness and strength of materials leads to both more efficient and safer structures. To gain knowledge of the mechanical behaviour of a material, mechanical testing in a laboratory environment is necessary. Over the years, several researchers have reported experimental results from mechanical testing of SLA resins. An early contribution to tensile

Figure 1.1: A graphical representation of the principles of SLA 3D printing [5].

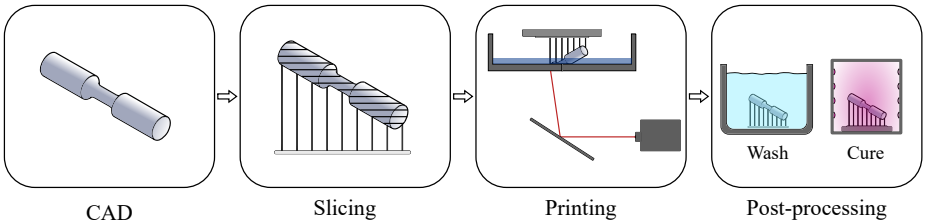

Figure 1.2: The workflow of SLA 3D printing.

testing of SLA specimens was provided by Cheah et al. [6] who found that the ultimate tensile strength, Young's modulus and failure strain were heavily dependent on laser intensity and post-curing. Some years later, Hague et al. [7] studied the effect of print orientation on the mechanical properties of SLA tensile specimens and found that the anisotropy was negligible. Similar results were obtained by Naik and Kiran [8] who also performed tests at different strain rates and found a strong strain-rate sensitivity on the mechanical behaviour of a different SLA resin. The above-mentioned results have been confirmed by several authors for a wide range of SLA resins in recent years [9–12]. Although compressive and tensile tests of SLA resins have been reported in the literature, they are seldom performed on the same resin and the effect of pressure sensitivity is therefore rarely studied.

In addition to understanding the mechanical response of a material, knowing how to model it mathematically is equally important with the prevalence of the finite element method (FEM) in today's engineering problems. Modelling of polymers is complex because large deformations and viscous behaviour typically have to be accounted for. Haward and Thackray [13] pioneered the field by formulating a one-dimensional constitutive model which divided the response of a glassy polymer into two parts: (i) an inter-molecular resistance modelled by energetic Hookean elasticity and viscous Eyring flow [14], and (ii) a network resistance due to the orientation of polymer chains modelled with entropic rubber elasticity. This model was later modified and extended to three dimensions by Boyce et al. [15] and the underlying principles have since been used in several published constitutive models [16–20].

Although the aforementioned models are applicable to glassy polymers, limited research exists regarding the constitutive modelling of SLA polymers. Early work was done by Wu et al. [21] who applied the model of Boyce et al. [15] to simulate the uniaxial compression response of an SLA resin. The model was able to adequately describe the observed strain-rate-dependent yield behaviour and strain hardening of the studied resin. An anisotropic version of the same model was later used by Zhang and To [22] to model another photo-polymeric resin, though this was not manufactured with the SLA method. More recently, Wang et al. [23] used an anisotropic elasto-plastic model to describe the slight anisotropy observed in a quasi-brittle SLA resin with good results. Both studies [22] [23] applied an anisotropic stress-based fracture criterion which agreed well with experiments. However, the fracture models were only used in uniaxial tension and bending problems. Ling et al. [24] applied an isotropic elasto-plastic model to simulate the compression of SLA-manufactured lattice structures and were able to predict the collapse load of the structures, but they did not include any fracture criterion.

1.2 Objectives

The goal of this work is to improve our understanding of the mechanical behaviour of additively manufactured SLA polymers and establish a material model able to describe the most important aspects of the mechanical behaviour. The objectives can be summarised as:

- Establish a comprehensive experimental database which can be used to calibrate a suitable material model.
- Formulate a material model able to describe the most important aspects of the experimentally observed mechanical behaviour of an SLA polymer.
- Calibrate the material model to the experimental data and perform a thorough verification and validation study of the model.

1.3 Scope

This work is limited to the stereolithography process and a single commercial SLA resin. The factors influencing a polymer's mechanical behaviour are many, and as such, some limitations need to be set. The experimental work is thus limited to:

- Room temperature.
- Low to intermediate strain rates.

Additionally, the material modelling is limited to:

- Large-strain (nonlinear) viscoelasticity.
- Isothermal constitutive equations.

The following topics are out of scope, but some are touched upon:

- Small-strain (linear) viscoelasticity.
- Temperature effects.
- Micromechanisms behind fracture.
- Print layer thickness.
- Specimen cure duration.
- Polymer ageing.
- Hygroscopic effects.

1.4 Research strategy

The approach taken in this work follows a typical material characterisation procedure which can be summarised as:

- Carry out a thorough experimental campaign investigating the mechanical properties of the material using axisymmetric specimens tested in tension and compression. The effects of strain rate, triaxiality, stress-relaxation and unloading are investigated.
- Carry out more complex tests on different specimen geometries to provide additional experimental data for the validation of a constitutive model.
- Formulate and implement a constitutive model able to describe the mechanical behaviour observed in the material tests.
- Verify the implementation of the model and document the behaviour of the model.
- Calibrate the constitutive model to the experimental data from the material tests.
- Validate the constitutive model's behaviour against experimental results not used in the calibration of the model.

1.5 Outline of thesis

The thesis is structured as follows:

Chapter 1 provides the background and motivation behind this thesis and establishes the objectives and scope.

Chapter 2 covers the theoretical framework of material modelling at large strains.

Chapter 3 presents the experiments carried out to characterise the material studied in this work and also gives a brief overview of the chosen material.

Chapter 4 presents the experiments performed to provide additional experimental data for the validation of the material model.

Chapter 5 gives a presentation of the constitutive equations and the numerical implementation of the material model developed as part of this work.

Chapter 6 presents a verification study of the implementation of the material model. The behaviour of the model is evaluated for different stress states and the effects of the different material parameters are studied.

Chapter 7 describes how the material model is calibrated to experimental data and compares simulated and experimental results.

Chapter 8 presents simulations of the validation tests and how the simulated results compare with the experimental results.

Chapter 9 rounds off the thesis by providing some concluding remarks and suggestions for further work.

1.6 Contributions

Parts of this thesis have been presented at an international conference and a journal article has been written and submitted for publication in a peer-reviewed international journal.

Journal article:

R. L. Sælen, O. S. Hopperstad, A. H. Clausen. Mechanical behaviour and constitutive modelling of an additively manufactured stereolithography polymer, *Submitted for journal publication*

Conference contribution:

R. L. Sælen, O. S. Hopperstad, A. H. Clausen. Material modelling and mechanical behaviour of an SLA additively manufactured polymer, In: *ECCOMAS Congress 2022*, Oslo, Norway 5th-9th June 2022

2 Theory

2.1 Continuum mechanics

The field of material modelling at large strains is built on continuum mechanics. This section provides an overview of the most important concepts from continuum mechanics used in this thesis. For a more detailed description, see the textbooks by Irgens [25] or Belytschko et al. [26].

2.1.1 Deformation

Consider an undeformed solid body at time t_0 as shown in Figure 2.1. A material point in this body is described by its position vector $\mathbf{X}$. The domain of the body is denoted Ω_0 and is called the *reference configuration*. At a later point in time $t > t_0$ the body is deformed. A material point in this body has a position vector $\mathbf{x}$ and the domain of the body is denoted Ω and is called the *current configuration*. The displacement vector $\mathbf{u}$ is defined by the relation

$$\mathbf{x} = \mathbf{X} + \mathbf{u} \tag{2.1}$$

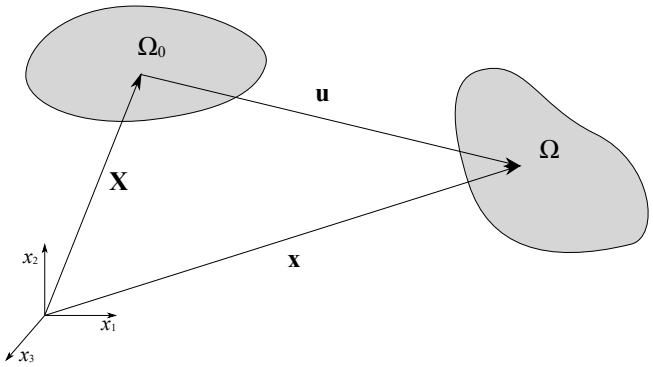

Figure 2.1: A solid body and its reference and current configuration.

The mapping of an infinitesimal line segment, d$\mathbf{X}$, from the reference configuration to the current configuration is performed as

$$\mathrm{d}\mathbf{x} = \mathbf{F} \cdot \mathrm{d}\mathbf{X}, \quad \mathbf{F} = \frac{\partial \mathbf{x}}{\partial \mathbf{X}} \tag{2.2}$$

where $\mathbf{F}$ is a second order tensor called the *deformation gradient*. An alternative expression is obtained by inserting Eq. 2.1 into the expression above

$$\mathbf{F} = \mathbf{I} + \frac{\partial \mathbf{u}}{\partial \mathbf{X}} \tag{2.3}$$

where $\frac{\partial \mathbf{u}}{\partial \mathbf{X}}$ is called the *displacement gradient tensor*.

The determinant of the deformation gradient, $J = \det(\mathbf{F})$ serves an important purpose in that it relates the volume of a material point in the reference configuration to the volume of a material point in the current configuration, viz.

$$J = \frac{\mathrm{d}V}{\mathrm{d}V_0} > 0 \tag{2.4}$$

J is called the *Jacobian determinant* or simply the *Jacobian*. The equation above can be used to express a relation between the area of a surface, $\mathrm{d}S_0$ with normal vector $\mathbf{n}_0$ in the reference configuration and the same surface, $\mathrm{d}S$, with normal vector $\mathbf{n}$ in the current configuration as

$$\mathrm{d}S\mathbf{n} = J\mathrm{d}S_0\mathbf{F}^{-\mathrm{T}} \cdot \mathbf{n}_0 \tag{2.5}$$

The relation above is known as *Nanson's formula*.

Through the polar decomposition theorem, the deformation gradient may be decomposed into the product of two second-order tensors representing pure rotation and pure stretching. The decomposition can be performed in two ways: by first rotating, then stretching and vice versa. The two ways of decomposition are illustrated in Figure 2.2. The deformation gradient is then expressed as

$$\mathbf{F} = \mathbf{RU} = \mathbf{VR} \tag{2.6}$$

where $\mathbf{R}$ is the rotation tensor and $\mathbf{U}$ and $\mathbf{V}$ are the right and left stretch tensors respectively. The rotation tensor is orthogonal, i.e, $\mathbf{R}\mathbf{R}^{\mathrm{T}} = \mathbf{I}$. The stretch tensors are positive definite and symmetric which makes them easier to work with than the generally non-symmetric deformation gradient. For rigid body

motion, $\mathbf{U} = \mathbf{V} = \mathbf{I}$ and $\mathbf{F} = \mathbf{R}$. Similarly, pure stretch is obtained when $\mathbf{R} = \mathbf{I}$, which gives $\mathbf{F} = \mathbf{U} = \mathbf{V}$. Any symmetric tensor can be expressed in terms of its eigenvalues and the dyadic product of its eigenvectors. This is called a *spectral decomposition* of a tensor. The right and left stretch tensors can then be written as

$$\mathbf{U} = \sum_{i=1}^{3} \lambda_i \mathbf{N}_i \otimes \mathbf{N}_i \tag{2.7}$$

$$\mathbf{V} = \sum_{i=1}^{3} \lambda_i \mathbf{n}_i \otimes \mathbf{n}_i \tag{2.8}$$

where λ_i are the eigenvalues, called principal stretches, and $\mathbf{N}_i$ and $\mathbf{n}_i$ are the corresponding eigenvectors of of $\mathbf{U}$ and $\mathbf{V}$ respectively. The eigenvectors are related through

$$\mathbf{n}_i = \mathbf{R} \cdot \mathbf{N}_i \tag{2.9}$$

Note that $\mathbf{U}$ and $\mathbf{V}$ have the same eigenvalues but different eigenvectors. This is because $\mathbf{V}$ contains rotations, whereas $\mathbf{U}$ does not. As such, $\mathbf{V}$ is expressed on the current configuration while $\mathbf{U}$ is expressed on the reference configuration.

The squares of the stretch tensors are called the *Cauchy-Green deformation tensors*. The right Cauchy-Green deformation tensor is defined as

$$\mathbf{C} = \mathbf{F}^{\mathrm{T}}\mathbf{F} = \mathbf{U}^2 = \sum_{i=1}^{3} \lambda_i^2 \mathbf{N}_i \otimes \mathbf{N}_i \tag{2.10}$$

and the left Cauchy-Green deformation tensor is defined as

$$\mathbf{B} = \mathbf{F}\mathbf{F}^{\mathrm{T}} = \mathbf{V}^2 = \sum_{i=1}^{3} \lambda_i^2 \mathbf{n}_i \otimes \mathbf{n}_i \tag{2.11}$$

The stretch tensors are obtained by taking the square root of their respective Cauchy-Green deformation tensor. This requires the computation of eigenvalues, which is a costly operation. Because of this, the Cauchy-Green deformation tensors are preferable to the stretch tensor in material models. Note that, equivalent to $\mathbf{V}$ and $\mathbf{U}$, the basis vectors of $\mathbf{B}$ are expressed in the current configuration, while the basis vectors of $\mathbf{C}$ are expressed in the reference configuration.

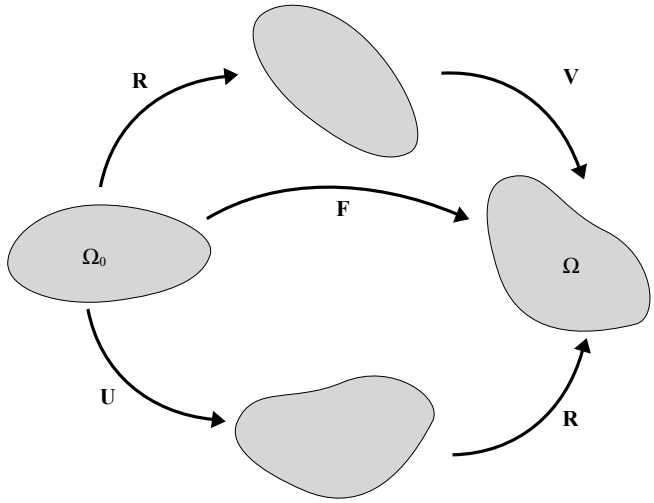

Figure 2.2: Polar decomposition of the deformation of a solid body.

The final class of deformation measures mentioned in this section are *strain tensors*. These differ from the previous deformation tensors in that they should vanish for rigid body motion. One commonly used strain tensor is the *Green strain tensor*, which is defined as

$$\mathbf{E} = \frac{1}{2}(\mathbf{C} - \mathbf{I}) \tag{2.12}$$

and is expressed in the reference configuration. By rewriting the above equation, using the relations $\mathbf{F} = \mathbf{I} + \frac{\partial \mathbf{u}}{\partial \mathbf{X}}$ and $\mathbf{C} = \mathbf{F}^{\mathrm{T}}\mathbf{F}$, the Green strain can be expressed as

$$\mathbf{E} = \frac{1}{2}\left(\frac{\partial \mathbf{u}}{\partial \mathbf{X}} + \left(\frac{\partial \mathbf{u}}{\partial \mathbf{X}}\right)^{\mathrm{T}} + \left(\frac{\partial \mathbf{u}}{\partial \mathbf{X}}\right)^{\mathrm{T}} \frac{\partial \mathbf{u}}{\partial \mathbf{X}}\right) \tag{2.13}$$

For small displacement gradients, i.e., small strains, the last term in the above expression vanishes and the infinitesimal strain tensor is retrieved, viz.

$$\boldsymbol{\varepsilon} = \frac{1}{2}\left(\frac{\partial \mathbf{u}}{\partial \mathbf{X}} + \left(\frac{\partial \mathbf{u}}{\partial \mathbf{X}}\right)^{\mathrm{T}}\right) \tag{2.14}$$

It is apparent that the Green strain tensor, and consequently the infinitesimal strain tensor, are expressed in the reference configuration. One strain tensor expressed in the current configuration is the *Hencky strain tensor* defined as

$$\boldsymbol{\varepsilon}_l = \ln(\mathbf{V}) = \sum_{i=1}^{3} \ln(\lambda_i)\, \mathbf{n}_i \otimes \mathbf{n}_i \tag{2.15}$$

This is commonly referred to as the logarithmic or true strain tensor and is the preferred strain measure in large strain finite element analyses due to its energy conjugacy with the Cauchy stress, which will be discussed in a later section.

2.1.2 Deformation rates

In order to describe rate-sensitive material behaviour, the rate form of the above-mentioned deformation and strain tensors needs to be established. The most basic deformation rate is simply the time derivative of the deformation gradient, which is expressed as

$$\dot{\mathbf{F}} = \frac{\partial \mathbf{v}}{\partial \mathbf{X}} = \frac{\partial \mathbf{v}}{\partial \mathbf{x}} \frac{\partial \mathbf{x}}{\partial \mathbf{X}} = \mathbf{L}\mathbf{F} \tag{2.16}$$

where $\mathbf{L}$ is called the *velocity gradient*. Like $\mathbf{F}$, $\dot{\mathbf{F}}$ and $\mathbf{L}$ are generally non-symmetric tensors. The velocity gradient may be split into a symmetric and anti-symmetric part, viz.

$$\mathbf{L} = \frac{1}{2}(\mathbf{L} + \mathbf{L}^{\mathrm{T}}) + \frac{1}{2}(\mathbf{L} - \mathbf{L}^{\mathrm{T}}) = \mathbf{D} + \mathbf{W} \tag{2.17}$$

where $\mathbf{D}$ is the *rate of deformation tensor* and $\mathbf{W}$ is the *spin tensor*. In a material point free of rotations, the rate of deformation tensor is the time derivative of the Hencky strain tensor viz.

$$\begin{aligned}\dot{\boldsymbol{\varepsilon}}_l = \frac{\mathrm{d}}{\mathrm{d}t}\ln(\mathbf{V}) &= \sum_{i=1}^{3} \frac{\mathrm{d}}{\mathrm{d}t}\ln(\lambda_i)\,\mathbf{n}_i \otimes \mathbf{n}_i \\ &= \sum_{i=1}^{3} \dot{\lambda}_i \lambda_i^{-1} \mathbf{n}_i \otimes \mathbf{n}_i \\ &= \sum_{i=1}^{3} \frac{\mathrm{d}\dot{x}_i}{\mathrm{d}X_i}\frac{\mathrm{d}X_i}{\mathrm{d}x_i} \mathbf{n}_i \otimes \mathbf{n}_i \\ &= \sum_{i=1}^{3} \frac{\mathrm{d}v_i}{\mathrm{d}x_i} \mathbf{n}_i \otimes \mathbf{n}_i = \mathbf{D}\end{aligned} \tag{2.18}$$

The above derivation is only possible when $\dot{\mathbf{n}}_i = \mathbf{0}$, i.e., the principal axes do not rotate. Otherwise, $\mathbf{D}$ is a measure of the rate of stretching in a material point and is not strictly related to any strain measure. The spin tensor, $\mathbf{W}$, can be thought of as a measure of the rate of change of the principal axes of the rate of deformation tensor. In the special case of rigid body rotation, the spin tensor can be written entirely in terms of the entries in the angular velocity vector $\boldsymbol{\omega}$, viz.

$$\mathbf{W} = \begin{bmatrix} 0 & -\omega_3 & \omega_2 \\ \omega_3 & 0 & -\omega_1 \\ -\omega_2 & \omega_1 & 0 \end{bmatrix} \quad , \quad \boldsymbol{\omega} = \begin{bmatrix} \omega_1 \\ \omega_2 \\ \omega_3 \end{bmatrix} \tag{2.19}$$

The rate of deformation tensor can be expressed in terms of the rate of the Green strain tensor by combining the two following equations, viz.

$$\mathbf{D} = \frac{1}{2}(\mathbf{L} + \mathbf{L}^{\mathrm{T}}) = \frac{1}{2}(\dot{\mathbf{F}}\mathbf{F}^{-1} + \mathbf{F}^{-\mathrm{T}}\dot{\mathbf{F}}^{\mathrm{T}}) \tag{2.20}$$

$$\dot{\mathbf{E}} = \frac{1}{2}\frac{\mathrm{d}}{\mathrm{d}t}(\mathbf{F}^{\mathrm{T}}\mathbf{F} - \mathbf{I}) = \frac{1}{2}(\mathbf{F}^{\mathrm{T}}\dot{\mathbf{F}} + \dot{\mathbf{F}}^{\mathrm{T}}\mathbf{F}) \tag{2.21}$$

such that

$$\mathbf{D} = \mathbf{F}^{-\mathrm{T}}\dot{\mathbf{E}}\mathbf{F}^{-1} \tag{2.22}$$

or equivalently

$$\dot{\mathbf{E}} = \mathbf{F}^{\mathrm{T}}\mathbf{D}\mathbf{F} \tag{2.23}$$

Equation 2.22 is an example of a *push-forward operation*. The rate of the Green strain tensor defined in the reference configuration is convected, or pushed forward, to the current configuration. The opposite case is called a *pull-back operation* and is shown in Equation 2.23. The Green strain rate tensor and the rate of deformation tensor evidently describe the same deformation process expressed in the reference configuration and current configuration respectively.

2.1.3 Stress measures

When a solid body is exposed to external loading, internal forces arise in order to satisfy force equilibrium at every material point. This is illustrated in Figure 2.3 where an internal force vector $\mathrm{d}\mathbf{f}$ is acting over the surface segment $\mathrm{d}S$ with a normal vector $\mathbf{n}$. The force vector is the resultant of a *traction*, $\mathbf{t}$, on the surface element $\mathrm{d}S$, viz.

$$\mathrm{d}\mathbf{f} = \mathbf{t}\mathrm{d}S \tag{2.24}$$

The relationship between the traction vector and the mechanical stress in a material point is given by Cauchy's law as

$$\mathbf{t} = \boldsymbol{\sigma} \cdot \mathbf{n} \tag{2.25}$$

where $\boldsymbol{\sigma}$ is the *Cauchy* or *true stress tensor*. As $\boldsymbol{\sigma}$ gives the relation between two vectors, i.e., first-order tensors, it is a second-order tensor and can be written in terms of its principal stresses, σ_i, and principal directions, $\mathbf{n}_i$ as

$$\boldsymbol{\sigma} = \sum_{i=1}^{3} \sigma_i \mathbf{n}_i \otimes \mathbf{n}_i \tag{2.26}$$

The above equation also makes use of the fact that σ is a symmetric tensor, which will be shown later on. Unlike the different strain measures, for which there are no "correct" choices, the Cauchy stress is considered the true stress tensor in the sense that it represents the tractions experienced by a material point in the current configuration. The Cauchy stress is thus the stress measure of choice when studying the strength of materials and is the stress reported by most finite element codes.

There are, however, other stress measures that are useful in material modelling. Stress measures defined on the reference configuration are often required when formulating models or balance laws. The first of the alternative stress measures

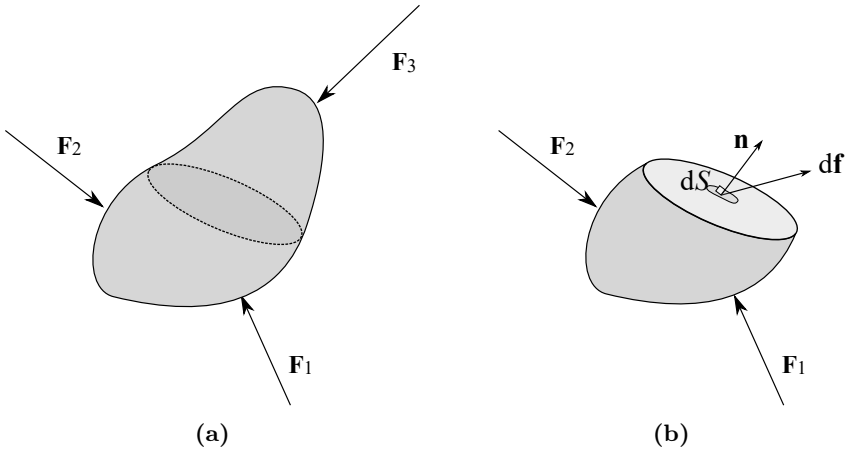

Figure 2.3: A body in the current configuration exposed to external forces illustrating **(a)** global equilibrium and **(b)** local equilibrium between external and internal forces.

mentioned in this section is the *first Piola-Kirchhoff stress*, $\mathbf{P}$, which is defined on the reference configuration as

$$\mathbf{t}_0 = \mathbf{P} \cdot \mathbf{n}_0 \tag{2.27}$$

By considering that the resultant of a traction on a surface in the reference configuration must be equal to the traction resultant on a surface in the current configuration, a relation between the Cauchy stress and the first Piola-Kirchhoff stress is obtained, viz.

$$\begin{aligned} \mathbf{t}_0 \mathrm{d}S_0 &= \mathbf{t} \mathrm{d}S \\ \mathbf{P} \cdot \mathbf{n}_0 \mathrm{d}S_0 &= \boldsymbol{\sigma} \cdot \mathbf{n} \mathrm{d}S \\ \mathbf{P} &= J \boldsymbol{\sigma} \mathbf{F}^{-T} \end{aligned} \tag{2.28}$$

where Nanson's formula was used in the last line. The first Piola-Kirchhoff stress is non-symmetric and has a physical interpretation of relating forces in the current configuration to a surface in the reference configuration.

Another common stress measure expressed in the reference configuration is the

second Piola-Kirchhoff stress, $\mathbf{S}$, which is defined as

$$\hat{\mathbf{t}}_0 = \mathbf{S} \cdot \mathbf{n}_0 \tag{2.29}$$

where $\hat{\mathbf{t}}_0$ is a traction vector on the reference configuration defined by a pull-back operation of a force vector on the current configuration, viz.

$$\hat{\mathbf{t}}_0 \mathrm{d}S_0 = \mathbf{F}^{-1} \cdot \mathbf{t} \mathrm{d}S \tag{2.30}$$

By applying the same procedure as with the first Piola-Kirchhoff stress, the relation between the second Piola-Kirchhoff stress and the Cauchy stress is obtained as

$$\begin{aligned} \hat{\mathbf{t}}_0 \mathrm{d}S_0 &= \mathbf{F}^{-1} \cdot \mathbf{t} \mathrm{d}S \\ \mathbf{S} \cdot \mathbf{n}_0 \mathrm{d}S_0 &= \mathbf{F}^{-1} \boldsymbol{\sigma} \cdot \mathbf{n} \mathrm{d}S \\ \mathbf{S} &= J \mathbf{F}^{-1} \boldsymbol{\sigma} \mathbf{F}^{-\mathrm{T}} \end{aligned} \tag{2.31}$$

The second Piola-Kirchhoff stress tensor is symmetric, unlike the first, and relates forces in the reference configuration to a surface in the same configuration. The relation between the second and first Piola-Kirchoff stress is obtained by combining Eq. 2.28 and Eq. 2.31, viz.

$$\mathbf{P} = \mathbf{F}\mathbf{S} \tag{2.32}$$

The last stress measure considered herein is the *Kirchhoff stress*, which is simply defined as

$$\boldsymbol{\tau} = J \boldsymbol{\sigma} \tag{2.33}$$

and is convenient when dealing with volume integrals containing the Cauchy stress over the reference configuration.

2.1.4 Balance laws

The mechanics of a solid body is governed by several balance laws. These are the balance of mass, momentum and energy.

The balance of mass simply states that the mass of the body in the current configuration must be equal to the mass of the body in the reference configuration. Mathematically, this is stated as

$$\int_{V_0} \rho_0 \mathrm{d}V_0 = \int_V \rho \mathrm{d}V \tag{2.34}$$

A local form is obtained by inserting the definition of the Jacobian, viz.

$$\rho_0 = J\rho \tag{2.35}$$

The balance of linear momentum states that the sum of external forces on a body equals the rate of change in total linear momentum. For a body subjected to traction forces, $\mathbf{t}$, on its surface, S, and body forces, $\mathbf{b}$, over its volume V, the balance law is expressed mathematically as

$$\int_S \mathbf{t} \mathrm{d}S + \int_V \mathbf{b} \mathrm{d}V = \frac{\mathrm{D}}{\mathrm{D}t} \int_V \rho \mathbf{v} \mathrm{d}V \tag{2.36}$$

By inserting Cauchy's law and applying the divergence theorem, the local form of the balance equation is obtained, viz.

$$\nabla \cdot \boldsymbol{\sigma} + \mathbf{b} = \rho \dot{\mathbf{v}} \tag{2.37}$$

where the divergence of an arbitrary second-order tensor, $\mathbf{A}$, in the current configuration is defined as

$$\nabla \cdot \mathbf{A} = \frac{\partial A_{ji}}{\partial x_j} \tag{2.38}$$

The same procedure may be performed in the reference configuration expressed in terms of the first Piola-Kirchhoff stress, $\mathbf{P}$, and body forces $\mathbf{b}_0$. The local form then reads

$$\nabla_0 \cdot \mathbf{P}^{\mathrm{T}} + \mathbf{b}_0 = \rho_0 \dot{\mathbf{v}} \tag{2.39}$$

where ρ_0 is the mass density in the reference configuration and the divergence of an arbitrary second-order tensor, $\mathbf{A}$, second-order tensor in the reference configuration is defined as

$$\nabla_0 \cdot \mathbf{A} = \frac{\partial A_{ji}}{\partial X_j} \tag{2.40}$$

The balance of angular momentum on the current configuration is simply the cross product between the linear momentum and the position vector, $\mathbf{x}$, which reads

$$\int_S \mathbf{x} \times \mathbf{t} \mathrm{d}S + \int_V \mathbf{x} \times \mathbf{b} \mathrm{d}V = \frac{\mathrm{D}}{\mathrm{D}t} \int_V \rho \mathbf{x} \times \mathbf{v} \mathrm{d}V \tag{2.41}$$

By once again applying the divergence theorem and Cauchy's law, the following result is obtained after some algebraic manipulation

$$\boldsymbol{\sigma} = \boldsymbol{\sigma}^{\mathrm{T}} \tag{2.42}$$

i.e., the Cauchy stress tensor is symmetric. By performing the appropriate transformations, the same result can also be expressed in terms of the first and second Piola-Kirchhoff stress tensors as

$$\mathbf{P}\mathbf{F}^{\mathrm{T}} = \mathbf{F}\mathbf{P}^{\mathrm{T}} \tag{2.43}$$

and

$$\mathbf{S} = \mathbf{S}^{\mathrm{T}} \tag{2.44}$$

Energy balance is expressed through the first law of thermodynamics, which states that the rate of change in energy in a system is equal to the sum of the rate of applied heat and the rate of work done by external forces on the system. Put simply, energy can neither be created nor vanish – it is always conserved. The law is expressed in the reference configuration as

$$\begin{aligned} \frac{\mathrm{D}}{\mathrm{D}t} \int_{V_0} (\rho_0 u + \frac{\rho_0}{2} \mathbf{v} \cdot \mathbf{v}) \mathrm{d}V_0 = \int_{S_0} -\mathbf{q}_0 \cdot \mathbf{n}_0 \mathrm{d}S_0 + \int_{V_0} r_0 \mathrm{d}V_0 \\ + \int_{S_0} \mathbf{t}_0 \cdot \mathbf{v} \mathrm{d}S_0 + \int_{V_0} \mathbf{b}_0 \cdot \mathbf{v} \mathrm{d}V_0 \end{aligned} \tag{2.45}$$

where u is the internal energy per unit mass, $\mathbf{q}_0$ is the heat flux through a

surface with normal vector $\mathbf{n}_0$ and r_0 is an internal heat source. A local form of the above balance equation may be achieved by rewriting the three terms. The time derivative of the energy term is calculated as

$$\frac{\mathrm{D}}{\mathrm{D}t}\int_{V_0}(\rho_0 u + \frac{\rho_0}{2}\mathbf{v}\cdot\mathbf{v})\mathrm{d}V_0 = \int_{V_0}(\rho_0\dot{u} + \rho_0\mathbf{v}\cdot\dot{\mathbf{v}})\mathrm{d}V_0 \tag{2.46}$$

The rate of applied heat can be expressed as a volume integral by applying the divergence theorem, viz.

$$\int_{S_0} -\mathbf{q}_0\cdot\mathbf{n}_0\mathrm{d}S_0 + \int_{V_0} r_0\mathrm{d}V_0 = \int_{V_0}(-\nabla_0\cdot\mathbf{q}_0 + r_0)\mathrm{d}V_0 \tag{2.47}$$

A similar exercise can also be performed on the rate of external work, viz.

$$\begin{aligned}\int_{S_0}\mathbf{t}_0\cdot\mathbf{v}\mathrm{d}S_0 + \int_{V_0}\mathbf{b}_0\cdot\mathbf{v}\mathrm{d}V_0 &= \int_{S_0}(\mathbf{P}\cdot\mathbf{n}_0)\cdot\mathbf{v}\mathrm{d}S_0 + \int_{V_0}\mathbf{b}_0\cdot\mathbf{v}\mathrm{d}V_0 \\ &= \int_{V_0}\big(\nabla_0\cdot(\mathbf{P}^{\mathrm{T}}\cdot\mathbf{v}) + \mathbf{b}_0\cdot\mathbf{v}\big)\mathrm{d}V_0 \\ &= \int_{V_0}\big((\nabla_0\cdot\mathbf{P}^{\mathrm{T}})\cdot\mathbf{v} + \mathbf{P}:\dot{\mathbf{F}} + \mathbf{b}_0\cdot\mathbf{v}\big)\mathrm{d}V_0\end{aligned} \tag{2.48}$$

By grouping all the terms together again and recalling the balance of linear momentum, the local form of the balance of energy is obtained, viz.

$$\rho_0\dot{u} = \mathbf{P}:\dot{\mathbf{F}} - \nabla_0\cdot\mathbf{q}_0 + r_0 \tag{2.49}$$

In the case of no heat conduction or heat sources, the above equation reduces to

$$\rho_0\dot{u} = \mathbf{P}:\dot{\mathbf{F}} \tag{2.50}$$

which shows that the first Piola-Kirchhoff stress is power conjugate to the time derivative of the deformation gradient. Other energy conjugate stress and strain tensor pairs are obtained by performing the appropriate transformations. These calculations are demonstrated for the second Piola-Kirchhoff stress and Cauchy stress below.

First, the relation between the first and second Piola-Kirchhoff stress is inserted into the expression for the internal power

$$\mathbf{P} : \dot{\mathbf{F}} = \mathbf{F}\mathbf{S} : \dot{\mathbf{F}} \tag{2.51}$$

Further tensor manipulations yield

$$\mathbf{F}\mathbf{S} : \dot{\mathbf{F}} = F_{ik} S_{kj} \dot{F}_{ij} = S_{kj} F_{ik} \dot{F}_{ij} = \mathbf{S} : (\mathbf{F}^{\mathrm{T}} \dot{\mathbf{F}}) \tag{2.52}$$

As $\mathbf{S}$ is a symmetric tensor and because a tensor contraction between a symmetric and anti-symmetric tensor vanishes, the above expression results in

$$\mathbf{S} : (\mathbf{F}^{\mathrm{T}} \dot{\mathbf{F}}) = \mathbf{S} : \left(\frac{1}{2} (\dot{\mathbf{F}}^{\mathrm{T}} \mathbf{F} + \mathbf{F}^{\mathrm{T}} \dot{\mathbf{F}}) \right) = \mathbf{S} : \dot{\mathbf{E}} \tag{2.53}$$

Thus, the second Piola-Kirchhoff stress tensor is power conjugate with the time derivative of the Green strain tensor. Finally, the rate of deformation measure conjugate to the Cauchy stress tensor is obtained by inserting the relation between the second Piola-Kirchhoff stress and Cauchy stress into the result above, viz.

$$J\mathbf{F}^{-1}\boldsymbol{\sigma}\mathbf{F}^{-\mathrm{T}} : \dot{\mathbf{E}} = J F^{-1}_{ik} \sigma_{kl} F^{-1}_{jl} \dot{E}_{ij} = J \sigma_{kl} F^{-1}_{ik} \dot{E}_{ij} F^{-1}_{jl} = J\boldsymbol{\sigma} : \mathbf{F}^{-\mathrm{T}} \dot{\mathbf{E}} \mathbf{F}^{-1} \tag{2.54}$$

By inserting the relation between $\mathbf{D}$ and $\dot{\mathbf{E}}$ and dividing both sides of the equation by J, we get the result

$$\rho \dot{u} = \boldsymbol{\sigma} : \mathbf{D} \tag{2.55}$$

which shows that the Cauchy stress tensor is power conjugate with the rate of deformation tensor in the current configuration.

2.1.5 The second law of thermodynamics

When formulating constitutive models, care must be taken such that the second law of thermodynamics is not violated. Put simply, the law states that the entropy of a closed system never decreases. Mathematically it is stated as an inequality in the reference configuration as

$$\frac{\mathrm{D}}{\mathrm{D}t}\int_{V_0}\rho_0 s\mathrm{d}V_0 \geq \int_{V_0}\frac{r_0}{\theta}\mathrm{d}V_0 - \int_{S_0}\frac{\mathbf{q}_0}{\theta}\cdot\mathbf{n}_0\mathrm{d}S_0 \tag{2.56}$$

where s is the entropy per unit mass and θ is the absolute temperature. The above equation is commonly referred to as the global form of the Clausius-Duhem inequality. By applying the divergence theorem to the heat flux term, the local form of the Clausius-Duhem inequality is obtained as

$$\rho_0\dot{s} \geq \frac{r_0}{\theta} - \nabla_0\cdot\left(\frac{\mathbf{q}_0}{\theta}\right) \tag{2.57}$$

By combining Eqs. 2.57 and 2.49, the inequality may be written as

$$\rho_0(\dot{s}\theta - \dot{u}) + \mathbf{P}:\dot{\mathbf{F}} - \frac{\mathbf{q}_0}{\theta}\cdot\nabla_0\theta \geq 0 \tag{2.58}$$

which is commonly referred to as the dissipation inequality. To simplify further expressions, we introduce the Helmholtz free energy per unit mass which is defined as

$$\psi = u - s\theta \tag{2.59}$$

The dissipation inequality may then be written as

$$-\rho_0(\dot{\psi} + s\dot{\theta}) + \mathbf{P}:\dot{\mathbf{F}} - \frac{\mathbf{q}_0}{\theta}\cdot\nabla_0\theta \geq 0 \tag{2.60}$$

By assuming that the Helmholtz free energy function has a form of

$$\psi = \psi(\mathbf{F},\theta) \tag{2.61}$$

its time derivative is expressed by the chain rule as

$$\dot{\psi} = \frac{\partial\psi}{\partial\mathbf{F}}:\dot{\mathbf{F}} + \frac{\partial\psi}{\partial\theta}\dot{\theta} \tag{2.62}$$

When inserted into the dissipation inequality, the following expression is obtained

$$-\rho_0\left(s + \frac{\partial\psi}{\partial\theta}\right)\dot{\theta} + \left(\mathbf{P} - \rho_0\frac{\partial\psi}{\partial\mathbf{F}}\right):\dot{\mathbf{F}} - \frac{\mathbf{q}_0}{\theta}\cdot\nabla_0\theta \geq 0 \tag{2.63}$$

which must be satisfied for all thermodynamic processes. This is only possible if

$$\mathbf{P} = \rho_0 \frac{\partial \psi}{\partial \mathbf{F}} \tag{2.64}$$

and

$$s = -\frac{\partial \psi}{\partial \theta} \tag{2.65}$$

It is evident that the Helmholtz free energy acts as a potential function for both the first Piola-Kirchhoff stress tensor and the entropy per unit mass.

2.2 Hyperelasticity

A material in which the stress-strain relationship can be derived from a scalar-valued potential function is called a *hyperelastic* material [25]. This section will expand upon this and present how different stress tensors may be expressed as partial derivatives of the Helmholtz free energy function. Note that for convenience, the Helmholtz free energy is defined per unit *reference volume* in this section and not per unit mass as in the previous section. The term, ρ_0, is thus omitted from the equations below. As shown in the previous section, the first Piola-Kirchhoff stress tensor must be expressed as the partial derivative of the Helmholtz free energy with respect to the deformation gradient to satisfy the dissipation inequality. If we repeat the derivation leading to this result, but express the stress power in terms of the second Piola-Kirchhoff stress tensor and the Green strain rate tensor, the following result is obtained

$$\mathbf{S} = \frac{\partial \psi}{\partial \mathbf{E}} \tag{2.66}$$

By employing the chain rule together with the definition of the Green strain tensor, the above equation can be expressed in terms of the right Cauchy-Green deformation tensor

$$\mathbf{S} = \frac{\partial \psi}{\partial \mathbf{E}} = \frac{\partial \psi}{\partial \mathbf{C}} : \frac{\partial \mathbf{C}}{\partial \mathbf{E}} = 2\frac{\partial \psi}{\partial \mathbf{C}} \tag{2.67}$$

and by inserting the relation between the second Piola-Kirchhoff and Cauchy stress tensors, an expression for the Cauchy stress tensor in terms of the derivative of the Helmholtz free energy function is obtained

$$\boldsymbol{\sigma} = \frac{2}{J}\mathbf{F}\frac{\partial \psi}{\partial \mathbf{C}}\mathbf{F}^{\mathrm{T}} \tag{2.68}$$

To simplify equations and avoid tensor calculus, the Helmholtz free energy function is commonly expressed in terms of the invariants of $\mathbf{C}$ rather than the full tensor itself. These invariants are expressed in terms of the principal stretches as

$$I_1 = \lambda_1^2 + \lambda_2^2 + \lambda_3^2 \tag{2.69}$$
$$I_2 = \lambda_1^2\lambda_2^2 + \lambda_2^2\lambda_3^2 + \lambda_3^2\lambda_1^2 \tag{2.70}$$
$$I_3 = \lambda_1^2\lambda_2^2\lambda_3^2 = J^2 \tag{2.71}$$

By the chain rule, the Cauchy stress tensor is now expressed as

$$\boldsymbol{\sigma} = \frac{2}{J}\mathbf{F}\left(\frac{\partial \psi}{\partial I_1}\frac{\partial I_1}{\partial \mathbf{C}} + \frac{\partial \psi}{\partial I_2}\frac{\partial I_2}{\partial \mathbf{C}} + \frac{\partial \psi}{\partial I_3}\frac{\partial I_3}{\partial \mathbf{C}}\right)\mathbf{F}^{\mathrm{T}} \tag{2.72}$$

The partial derivatives of the invariants read as

$$\frac{\partial I_1}{\partial \mathbf{C}} = \mathbf{I} \tag{2.73}$$
$$\frac{\partial I_2}{\partial \mathbf{C}} = I_1\mathbf{I} - \mathbf{C} \tag{2.74}$$
$$\frac{\partial I_3}{\partial \mathbf{C}} = I_3\mathbf{C}^{-1} \tag{2.75}$$

which when inserted into Eq. 2.72 gives

$$\boldsymbol{\sigma} = \frac{2}{J}\left(\frac{\partial \psi}{\partial I_1} + I_1\frac{\partial \psi}{\partial I_2}\right)\mathbf{B} - \frac{2}{J}\frac{\partial \psi}{\partial I_2}\mathbf{B}^2 + \frac{\partial \psi}{\partial J}\mathbf{I} \tag{2.76}$$

Hyperelastic models implemented in FEM solvers typically use a volumetric-isochoric split of the deformation gradient for computational efficiency [27]. The isochoric deformation gradient is defined as

$$\bar{\mathbf{F}} = J^{-1/3}\mathbf{F} \tag{2.77}$$

and as the name implies, $\det(\bar{\mathbf{F}}) = 1$. The volumetric deformation gradient is defined as

$$\mathbf{F}_{\text{vol}} = J^{1/3}\mathbf{I} \tag{2.78}$$

and the total deformation gradient is expressed as a multiplicative decomposition of the isochoric and volumetric deformation gradients

$$\mathbf{F} = \mathbf{F}_{\text{vol}}\bar{\mathbf{F}} \tag{2.79}$$

The isochoric right Cauchy-Green deformation tensor is defined as

$$\bar{\mathbf{C}} = \bar{\mathbf{F}}^{\mathrm{T}}\bar{\mathbf{F}} = J^{-2/3}\mathbf{C} \tag{2.80}$$

and its first two invariants can be expressed as

$$\bar{I}_1 = J^{-2/3}I_1 \tag{2.81}$$

$$\bar{I}_2 = J^{-4/3}I_2 \tag{2.82}$$

The Cauchy stress from Eq. 2.76 can now be expressed in terms of the isochoric invariants as

$$\begin{aligned}\boldsymbol{\sigma} =& \frac{2}{J}\left(\frac{\partial\psi}{\partial\bar{I}_1}\frac{\partial\bar{I}_1}{\partial I_1} + J^{2/3}\bar{I}_1\frac{\partial\psi}{\partial\bar{I}_2}\frac{\partial\bar{I}_2}{\partial I_2}\right)\mathbf{B} - \frac{2}{J}\frac{\partial\psi}{\partial\bar{I}_2}\frac{\partial\bar{I}_2}{\partial I_2}\mathbf{B}^2 \\ &+ \left(\frac{\partial\psi}{\partial\bar{I}_1}\frac{\partial\bar{I}_1}{\partial J} + \frac{\partial\psi}{\partial\bar{I}_2}\frac{\partial\bar{I}_2}{\partial J} + \frac{\partial\psi}{\partial J}\right)\mathbf{I}\end{aligned} \tag{2.83}$$

Inserting the derivatives of the isochoric invariants gives

$$\boldsymbol{\sigma} = \frac{2}{J}\left(\frac{\partial\psi}{\partial\bar{I}_1} + \frac{\partial\psi}{\partial\bar{I}_2}\bar{I}_1\right)\bar{\mathbf{B}} - \frac{2}{J}\frac{\partial\psi}{\partial\bar{I}_2}\bar{\mathbf{B}}^2 + \left(\frac{\partial\psi}{\partial J} - \frac{2\bar{I}_1}{3J}\frac{\partial\psi}{\partial\bar{I}_1} - \frac{4\bar{I}_2}{3J}\frac{\partial\psi}{\partial\bar{I}_2}\right)\mathbf{I} \tag{2.84}$$

where $\bar{\mathbf{B}}$ is the isochoric left Cauchy-Green deformation tensor

$$\bar{\mathbf{B}} = J^{-2/3}\mathbf{B} \tag{2.85}$$

For materials in which the Helmholtz free energy function is independent of $\bar{I}_2$, we end up with the following simple expression for the Cauchy stress tensor

$$\boldsymbol{\sigma} = \frac{2}{J}\frac{\partial \psi}{\partial \bar{I}_1}\bar{\mathbf{B}}' + \frac{\partial \psi}{\partial J}\mathbf{I} \tag{2.86}$$

where

$$\bar{\mathbf{B}}' = \bar{\mathbf{B}} - \frac{\mathrm{tr}(\bar{\mathbf{B}})}{3}\mathbf{I} \tag{2.87}$$

Equations 2.84 and 2.86 provide relatively simple expressions for the Cauchy stress of a hyperelastic material, which will be useful later on.

3 Material tests

This chapter presents the experimental campaign carried out for the purpose of characterising the material behaviour. The effects of triaxiality, strain rate and print orientation were studied through tensile and compression tests of axisymmetric specimens.

3.1 Material and specimen preparation

The material studied in this work is the Formlabs Durable v2 stereolithographic resin. According to the manufacturer, the Durable resin is suited for parts requiring high impact strength and it has elastic properties similar to high density polyethylene (HDPE) and polypropylene (PP). The resin consists of a proprietary mixture of acrylated and methacrylated monomers and oligomers together with a photoinitiator. When the photoinitiator is exposed to ultraviolet (UV) radiation, it is split into free radicals and a solid polymer is formed through the process of photopolymerisation. The monomers form long polymer chains and the oligomers serve as crosslinking agents, which gives the material its strength.

The test specimens shown in Figures 3.1 and 3.2 were manufactured with a Formlabs 3 SLA printer. The SLA process was described in detail in Chapter 1.1. To limit the scope of the experimental study, all print parameters, except the print orientation, were kept constant in the production of the test specimens. A layer thickness of 50 µm was used for all specimens. After printing, the uncured resin was washed away with isopropyl alcohol (IPA) by using the Formlabs Wash station for 20 minutes. After the specimens were cleaned and dried, they were cured in the Formlabs Cure station for four hours at a temperature of 60 °C and subjected to 405 nm UV light. The manufacturer recommends a cure time of one hour when using the Durable resin, as this yields the optimal trade-off between mechanical performance and cure time. We, however, have chosen to cure the specimens for four hours to minimise any potential curing between printing and testing. When the curing was done, the specimens were immediately taken out of the Form Cure and cooled at room temperature.

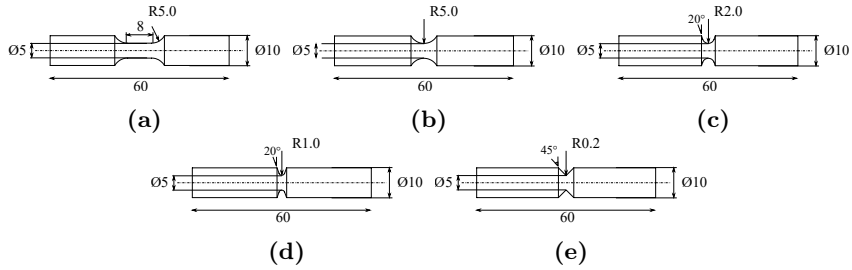

Figure 3.1: Geometries of **(a)** a smooth specimen and specimens with notch radii **(b)** 5.0 mm, **(c)** 2.0 mm, **(d)** 1.0 mm and **(e)** 0.2 mm. Dimensions in mm.

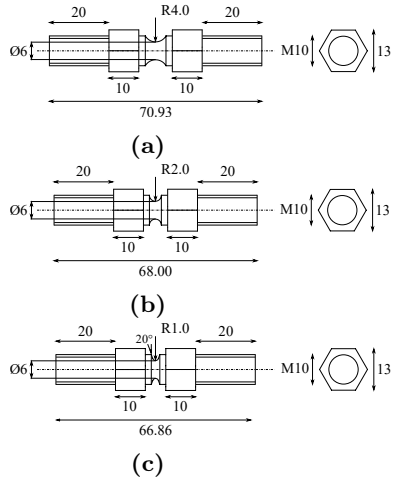

Figure 3.2: Geometries of notched compression specimens with notch radii **(a)** 4.0 mm, **(b)** 2.0 mm and **(c)** 1.0 mm. Dimensions in mm.

3.2 Experimental programme

The experimental programme was divided into four test series studying the effects of (i) print orientation, (ii) strain-rate sensitivity, (iii) unloading, and (iv) pressure sensitivity. Unless otherwise specified, each test was repeated three times. The print orientation series consists of monotonic tensile tests of smooth specimens produced with different print orientations. Print orientations of 0°, 45° and 90° were investigated, and the definition of the angles are shown in Figure 3.3. The tests were performed with a cross-head velocity of 3 mm/min, which results in a nominal strain rate of $\dot{e} = 6.25 \cdot 10^{-3}\,\mathrm{s}^{-1}$ in the parallel section of the specimens.

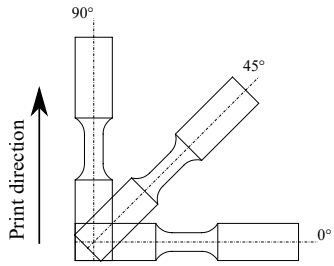

Figure 3.3: The different print orientations studied in the anisotropy test series.

The strain-rate series also consists of monotonic tensile tests of smooth specimens but at three different nominal strain rates. Cross-head velocities of 0.3 mm/min, 3 mm/min and 30 mm/min were used, yielding nominal strain rates in the parallel section of $6.25 \cdot 10^{-4}\,\mathrm{s}^{-1}$, $6.25 \cdot 10^{-3}\,\mathrm{s}^{-1}$ and $6.25 \cdot 10^{-2}\,\mathrm{s}^{-1}$ respectively. All specimens were printed with a 90° orientation. Two repeat tests were performed for each cross-head velocity.

The unloading test series includes two test types: firstly, loading/unloading tests performed at various strain rates and secondly, a single relaxation test. Again, smooth specimens printed with a 90° orientation were applied. In the loading/unloading tests, the specimens were loaded until a cross-head displacement of 5 mm was reached. The specimens were then fully unloaded followed by final reloading until failure. These tests were performed with the same cross-head velocities as the strain-rate test series. Only one test was performed for each cross-head velocity due to the number of specimens at hand. The relaxation test was performed as an arrested loading/unloading test. The procedure was as follows: first, the specimen was loaded to a cross-head displacement of 4 mm and held in place for 10 minutes. The specimen was then loaded to a cross-head displacement of 5 mm, followed by unloading back to 4 mm where it was again held for 10 minutes. Finally, the specimen is fully unloaded. The relaxation test

was performed with a cross-head velocity of 3 mm/min.

In the pressure sensitivity test series, notched specimens with varying notch radii were tested in monotonic tension and compression. The specimens tested in tension were printed with a 0° orientation, while the specimens tested in compression were printed with a 45° orientation due to their more complex geometry. The cross-head velocities applied to the different specimens were determined through preliminary simulations to ensure that the logarithmic strain rate was approximately $5 \cdot 10^{-3}$ s^{-1} at the onset of yielding. For the tensile specimens, these were 1.5 mm/min, 0.68 mm/min, 0.52 mm/min and 0.48 mm/min for the R5, R2, R1 and R0.2 specimens, respectively, while for the compression specimens velocities of 1.0 mm/min, 0.75 mm/min and 0.50 mm/min were used for the R4, R2 and R1 specimens, respectively. The R4 specimens were tested in both tension and compression.

3.3 Experimental setup

All tests covered in this chapter were carried out on an Instron 5944 universal testing system with a 2 kN load cell. Hydraulic clamps were used to grip the tensile specimens, while the compression test specimens were mounted with 3D-printed threads. The use of threads was made to reduce the risk of the specimens buckling during compression by making the boundary conditions more rigid. The compression specimens also featured 3D-printed bolt heads between the threads and notched region to aid with mounting and off-load the threads during compression.

Two digital cameras mounted perpendicular to each other were used to monitor the tests. The logging frequency was selected such that approximately 300 images were obtained from each test. These images were then used in digital image correlation (DIC) and edge trace analyses, which are described in the next section. In addition to digital cameras, the tests performed as part of the strain-rate sensitivity and unloading tests series were monitored with a thermal camera to measure the temperature evolution at the surface of the specimens. The side of the specimens facing the thermal camera was painted black to aid with temperature measurements. The sides facing the digital cameras were painted with a black-and-white speckle pattern to facilitate DIC analyses. The setup is shown in Figure 3.4.

Displacement control was used in the execution of all tests. The tensile tests were loaded until failure, while the compression tests were loaded until the limit of the load cell, 2 kN, was reached. Both test types were performed with a constant cross-head velocity.

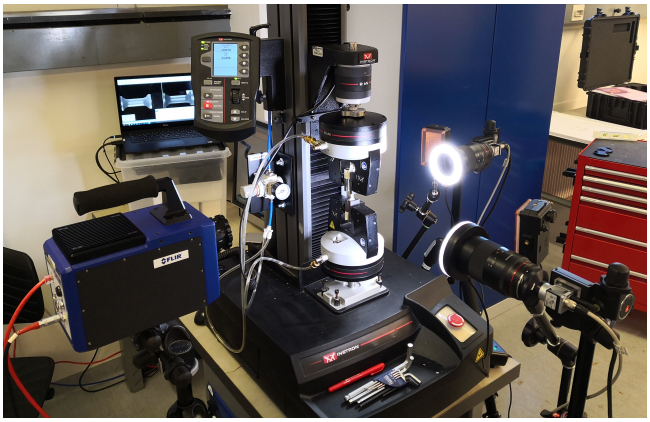

Figure 3.4: Experimental tensile test setup showing a clamped specimen surrounded by two cameras with ring-lighting and one thermal camera.

3.4 Processing of results

3.4.1 Calculation of stress and strain

As the tests presented in this chapter are performed to characterise the mechanical behaviour of the studied material, the most important data obtained from the tests are stress-strain curves. The procedure for calculating stresses and strains is presented in this section.

The surface deformations of the smooth specimens were measured by performing DIC analyses on the images captured with the digital cameras, using the finite element-based DIC python package μDIC [28]. The longitudinal stretch ratio, λ_l, was extracted from the longitudinal component of the right stretch tensor, $\mathbf{U} = \sqrt{\mathbf{F}^\mathrm{T}\mathbf{F}}$, calculated in the DIC analyses. To account for noise in the DIC solution, the longitudinal stretch ratio was averaged over an element column containing n_els elements as

$$\lambda_\mathrm{l} = \frac{\sum_{e=1}^{n_\mathrm{els}} \lambda_{\mathrm{l},e}}{n_\mathrm{els}} \tag{3.1}$$

The element column used in the calculation of the average stretch is shown in Figure 3.5.

To obtain an accurate measure of the radial stretch ratio, both for the smooth

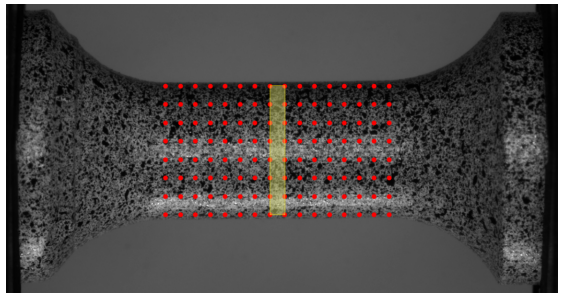

Figure 3.5: A picture of a smooth tensile specimen showing the speckle pattern together with the nodes of the finite element mesh used in the DIC analysis. The element column used in the extraction of the stretch ratios is highlighted.

specimens and the notched specimens, the stretch ratio was calculated from an edge trace routine in Python using the Sobel edge detection algorithm [29]. The edge trace routine measures the current minimum diameter in the gauge area of the specimens, from which the radial stretch ratio is calculated as

$$\lambda_{\mathrm{r}} = \frac{D}{D_0} \tag{3.2}$$

where D is the current minimum diameter and D_0 is the initial diameter. The circumferential stretch ratio, λ_{c}, is equal to the radial stretch ratio due to the axisymmetry of the specimens. This is readily seen in the expressions

$$\lambda_{\mathrm{c}} = \frac{2\pi D}{2\pi D_0} = \frac{D}{D_0} = \lambda_{\mathrm{r}} \tag{3.3}$$

With the stretch ratios of the principal directions at hand, the corresponding logarithmic strain components are calculated as

$$\varepsilon_i = \ln(\lambda_i) \tag{3.4}$$

Logarithmic strain rates, $\dot{\varepsilon}_i$, were then calculated through numerical differentiation in Python.

The stress reported in this work is the net stress defined as

$$\sigma = \frac{F}{A} \tag{3.5}$$

where F is the measured force from the machine and A is the current minimum cross-sectional area calculated as $A = \pi\lambda_r^2 D_0^2/4$.

The stress and strain measures defined above express the Cauchy stress and logarithmic strain experienced by the material in the gauge section of the smooth specimens. In the notched specimens, however, the net stress expresses an average stress over the minimum cross-sectional area, while the logarithmic strain is a measure of the surface strains in the notch root. To avoid relating an average stress measure to a local strain measure for the notched specimens, an average strain measure is used instead. By assuming that a thin, cylindrical slice of material in the notch root deforms homogeneously and with no change in volume, i.e., $\lambda_\mathrm{l}\lambda_\mathrm{r}^2 = 1$, an average logarithmic strain is defined as

$$\bar{\varepsilon}_\mathrm{l} = -2\ln(\lambda_\mathrm{r}) \tag{3.6}$$

This strain measured is hereby referred to as the isochoric logarithmic strain. The assumption of isochoric deformation does not necessarily hold, but the defined strain measure still serves as a measure of the average logarithmic strain through the minimum cross-sectional area.

3.4.2 Temperature measurements

The surface temperature of the specimen monitored by the IR camera is obtained by calculating the mean temperature of an area of interest (AOI). The AOI is chosen such that the gauge area of the tensile specimen remains within the area during the entire test. Figures 3.6 (a) and (b) show a typical AOI for a smooth specimen in the undeformed and deformed configuration respectively. The software FLIR Altair was used for reading the thermal images obtained by the IR camera, as well as retrieving the mean temperature from the AOI.

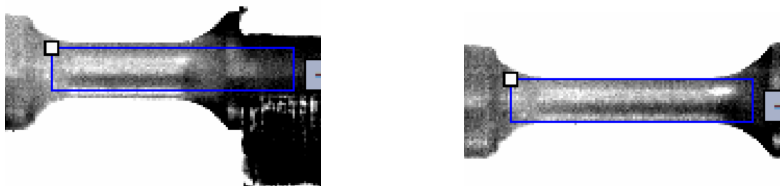

(a) **(b)**

Figure 3.6: Area of interest for temperature retrieval shown for a specimen in the reference configuration **(a)** and deformed configuration **(b)**.

3.5 Results

3.5.1 Anisotropy and general behaviour

The results from the anisotropy test series are shown in Figure 3.7 in terms of net stress vs. logarithmic strain curves. Before turning attention to the effect of print orientation, the overall stress-strain behaviour should be addressed. The material exhibits an initial linear elastic response followed by inelastic flow. After a short plateau following the onset of inelastic flow, rapid strain hardening due to the alignment of the polymer chains is observed. The specimens fail suddenly with a brittle fracture mode; yet, the logarithmic failure strain exceeds 0.4 in all cases. Another noteworthy observation is that no strain localisation is observed due to the amount of strain hardening taking place. Images from a test of a specimen printed with a 90° orientation illustrating the large strains before the brittle fracture mode are shown in Figure 3.8.

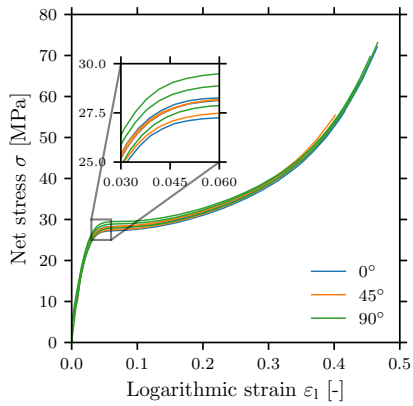

Figure 3.7: Net stress vs. logarithmic strain curves from uniaxial tensile specimens with different print orientations.

The lack of strain localisation can be explained by the Considère criterion which states that a neck forms when the following equation is satisfied

$$\frac{\mathrm{d}\sigma}{\mathrm{d}\varepsilon_\mathrm{l}} = \sigma \tag{3.7}$$

The net stress from a tensile test of a 90° orientation specimen is plotted against its derivative with respect to the longitudinal logarithmic strain in Figure 3.9. It is seen that the two curves cross twice, within a logarithmic strain interval of

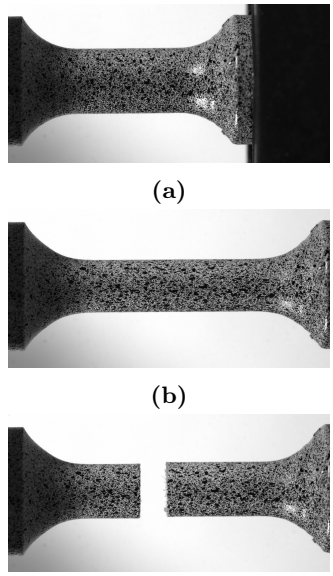

(a) **(b)** **(c)**

Figure 3.8: Images from the tensile test of a smooth specimen printed with a 90° orientation, from **(a)** before the test, **(b)** the final frame before fracture and **(c)** the frame immediately after fracture.

approx. 0.1. This means that a neck is formed, but is quickly stabilised again due to the strain hardening of the material. The stable neck will thus propagate to the shoulders of the specimen such that the entire gauge area in principle forms a stable neck, giving the appearance of no strain localisation.

As for the anisotropy of the material, a slight print orientation dependency is observed for the flow stress, as can be seen in the zoomed-in box in Figure 3.3. The 90° orientation specimens have an average flow stress that is approx. 1 MPa higher than for the other orientations, but otherwise the stress-strain response is close to identical between the different print orientations. The material can thus be considered isotropic – at least for all practical purposes. Surface longitudinal logarithmic strain fields from DIC analyses are shown for one specimen per print orientation in Figure 3.10. The fields are extracted from the point in the test history where the cross-head displacement was 5 mm. The results show that the magnitude of the strains is similar for the different print orientations, but some local inhomogeneities exist.

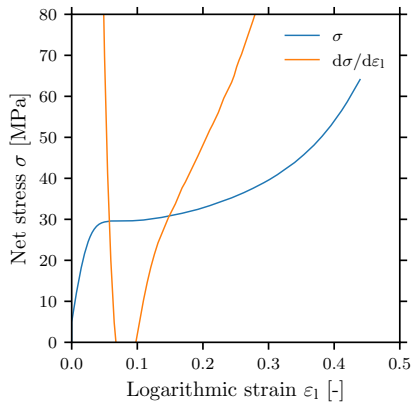

Figure 3.9: Net stress vs. logarithmic strain from a tensile test of 90° orientation specimen plotted together with its derivative with respect to the logarithmic strain.

Another measure of the anisotropy is seen in Figure 3.11, where the ratio between the minimum diameter measured with the two digital cameras, D_1 and D_2, is plotted against the cross-head displacement for all the tests. With the exception of two outlier tests, most of the data points lie within a 0.5% relative difference between the two cameras. This result both confirms the assumption of an axisymmetric deformation made in the previous section and supports the claim of isotropic material behaviour.

As polymers can exhibit a large change in volume, even during uniaxial tension [30], volumetric strains, $\varepsilon_v = \ln(\lambda_l \lambda_r^2)$, are reported in Figure 3.12. The material at hand, however, appears to be inelastically incompressible as the calculated volumetric stains are close to zero for all tests except two outliers.

3.5.2 Strain-rate dependence

The results of the monotonic tensile test at different cross-head velocities are shown in terms of net stress vs logarithmic strain curves in Figure 3.13 (a), while the corresponding logarithmic strain rates are plotted in Figure 3.13 (b). The flow stress is observed to exhibit a strong strain-rate sensitivity, as increasing the strain rate by a decade increases the flow stress by approx. 40%. A strain-rate sensitivity is also observed for the initial elastic stiffness. A strain-rate-dependent softening behaviour is also observed immediately after the onset of inelastic flow. This is especially apparent in the force-displacement curves shown in Figure 3.14.

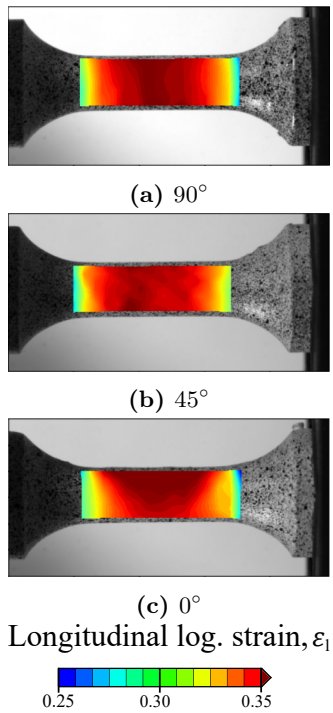

Figure 3.10: Longitudinal logarithmic strain fields from DIC analyses of tensile tests with print orientation **(a)** 90°, **(b)** 45° and **(c)** 0°. The fields are shown for a cross-head displacement of 5 mm.

3.5.3 Unloading

The loading-unloading tests show the same initial strain-rate dependent behaviour as the monotonic tensile tests, as can be seen from the net stress vs. logarithmic strain curves in Figure 3.15 (a). The unloading and subsequent reloading cause hysteresis in the material due to the viscoelastic material behaviour. Even though the cross-head displacement before unloading is equal for the different specimens, the logarithmic strain in the gauge area is not. This suggests that a larger amount of deformation takes place in the shoulder and clamping area of the specimen as the strain rate decreases.

Figure 3.15 (b) shows the change in surface temperature, as measured with the IR camera, for the different strain rates. At the lowest strain rate, the measured temperature increase was less than 1 °C. Because of the long duration of the

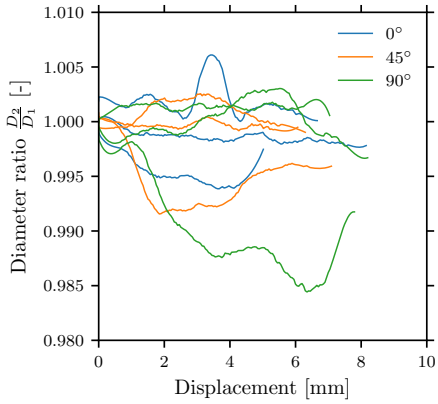

Figure 3.11: Curves from the anisotropy test series showing the ratio between the minimum cross-sectional diameter measured with camera 1 and camera 2 plotted against the cross-head displacement.

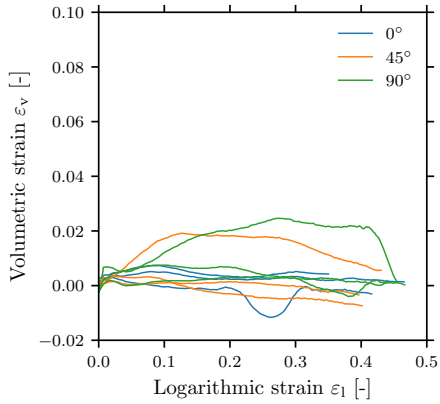

Figure 3.12: Curves from the anisotropy test series showing volumetric strain vs. logarithmic longitudinal strain curves.

test, this may simply be the change in ambient temperature or heating due to the lighting. The two tests performed at higher strain rates show a trend of initial thermoelastic cooling followed by heating due to viscous dissipation. In the unloading phase, the temperature change due to thermoelasticity is reversed, and a temperature increase is observed. In the subsequent reloading phase, the trend of thermoelastic cooling followed by viscous heating is repeated. Overall, the

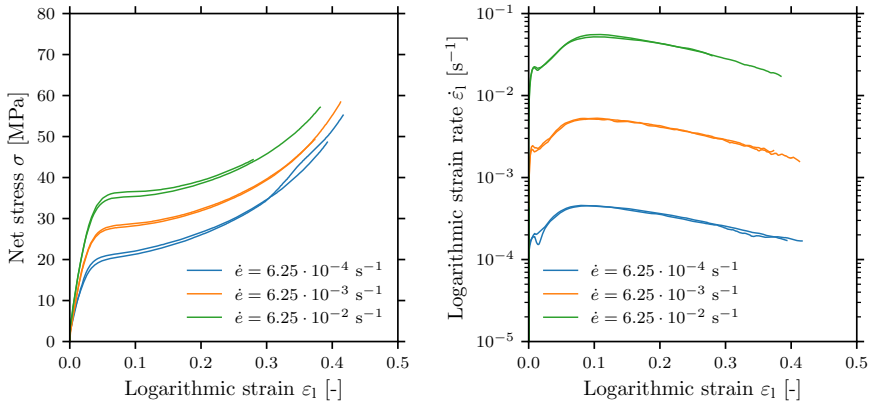

(a) **(b)**

Figure 3.13: **(a)** Net stress vs. logarithmic strain curves from uniaxial tensile tests performed with three different cross-head velocities and **(b)** corresponding logarithmic strain rates.

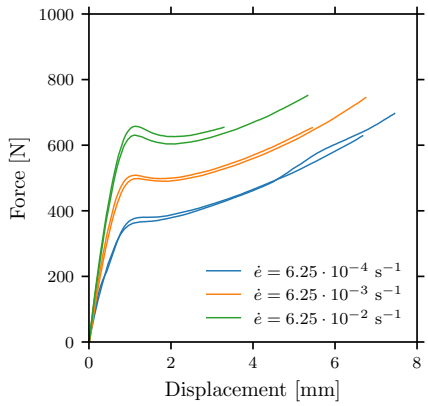

Figure 3.14: Force vs. displacement curves from the strain-rate test series.

self-heating at the studied strain rates is minor and no signs of thermal softening are observed in the stress-strain curves. The effect of thermal softening could, however, be significant for higher strain rates. According to the manufacturer, the heat deflection temperature of the resin is 45 °C [31] which is relatively close to room temperature. The increase in stress levels due to strain rate in combination with the lower loading duration means that a larger amount of work will be dissipated as heat in the material for higher rates, which might affect the strain hardening response.

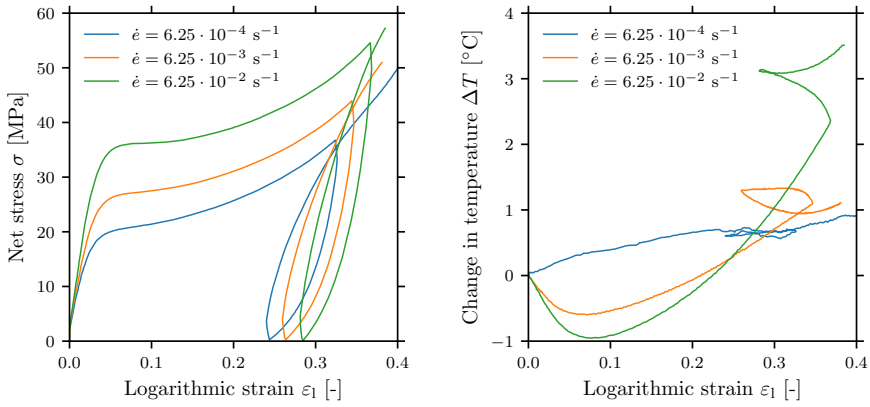

(a) **(b)**

Figure 3.15: **(a)** Net stress vs. logarithmic strain curves from uniaxial tensile tests performed with three different cross-head velocities and **(b)** change in surface temperature measured with an IR camera.

3.5.4 Relaxation

The last assessment of the viscoelastic properties of the material is obtained from the results of the relaxation test. The stress-strain and stress-time curves from the test are shown in Figure 3.16 (a) and Figure 3.16 (b) respectively. A strong stress relaxation effect is observed during the loading phase, where the stress magnitude is nearly halved after allowing the specimen to relax for 10 minutes. In the unloading phase, the stress actually increases during the relaxation. In both the loading and unloading phases, the stress seems to relax towards an equilibrium stress of approx. 15 MPa. The observed relaxation behaviour is the same as reported by Bergström and Boyce [18] for elastomeric materials.

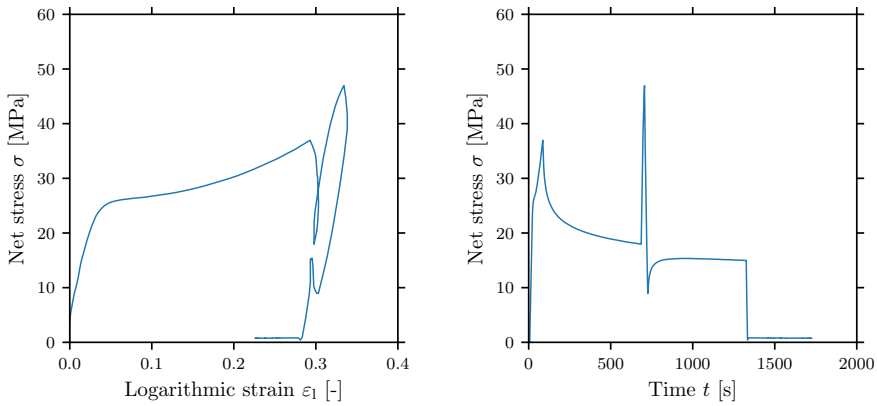

(a) **(b)**

Figure 3.16: Results from the relaxation test in terms of **(a)** net stress vs. logarithmic strain and **(b)** net stress vs time curve.

3.5.5 Pressure sensitivity

Net stress vs isochoric logarithmic strain curves from the notch tensile tests are shown in Figure 3.17 (a). The results from the smooth 0° specimens tested in the anisotropy series are included as a comparison between notched and smooth specimens. An increase in stress level and a reduction in ductility are observed as the notch radius decreases. The reduced ductility stems from the stress localisation at the notch root. Here, large stress levels leading to fracture occur at relatively low cross-head displacements.

The net failure stress is plotted for each specimen type in Figure 3.17 (b). The average failure stress and the spread decrease with the notch radius. Both observations can be explained by the localised deformation caused by the notches. As the notch radius decreases, the strains and stresses become highly localised at the surface of the notch root. When fracture occurs in the localised region, the stress levels in the rest of the specimen are relatively low, which leads to a low average stress, i.e., net stress. The reduced scatter indicates that the fracture of the specimens is governed by a size effect. When compared with the notched specimens, the smooth specimens feature a larger volume in which fracture can occur because the stresses are distributed uniformly through the entire gauge section. With larger volume comes an increased probability of the occurrence of a critical defect which can trigger brittle fracture.

The results from the compression tests are shown in Figure 3.18 (a) in terms

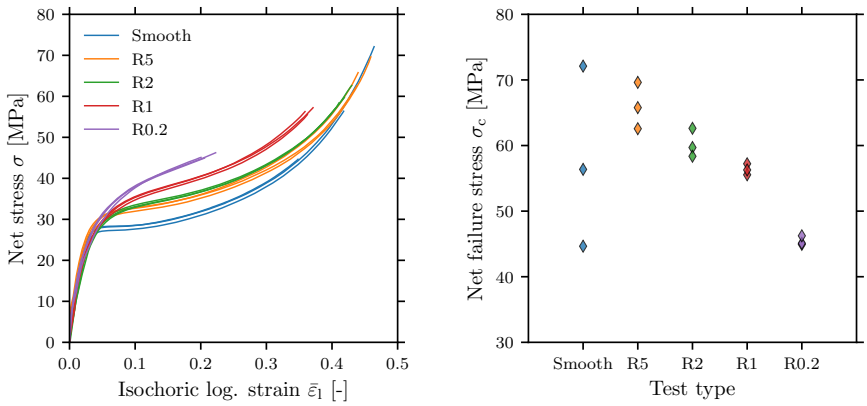

Figure 3.17: Results from notch tensile tests: **(a)** Net axial stress vs. isochoric axial strain and **(b)** net axial failure stress for all specimens.

of absolute net stress vs absolute isochoric logarithmic strain. The logarithmic strains are plotted until the point at which the edge trace routine is no longer able to track the notch edges due to extensive deformations in the notch area. The same trends as in the notch tensile tests are seen, in which the stress levels rise with the sharpness of the notch radius. Figure 3.18 (b) shows a comparison between tensile and compression tests of the R4 specimens. A clear pressure dependency is observed where the net stress at yield is higher in compression than in tension. Reduced strain hardening is seen in the compression tests compared to the tensile tests. A possible explanation for this is that a slight eccentricity between the upper and lower mounts, as seen in Figure 3.19, caused a shear deformation in the compression specimens at large strains, i.e., after yield. A shear deformation mode leads to less extension of the polymer chains than a multiaxial deformation mode, which will also result in less apparent strain hardening.

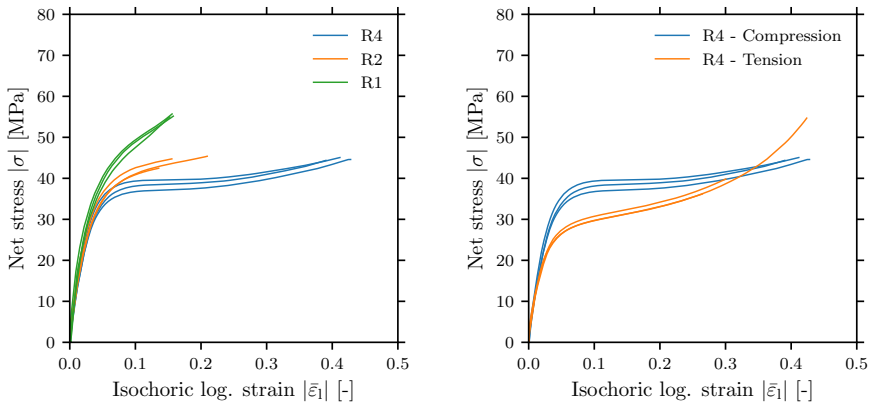

Figure 3.18: Results from notch compression tests: **(a)** Net axial stress vs. isochoric axial strain for all compression tests and **(b)** net axial stress vs. isochoric axial strain for the compression and tensile tests of the R4 specimen.

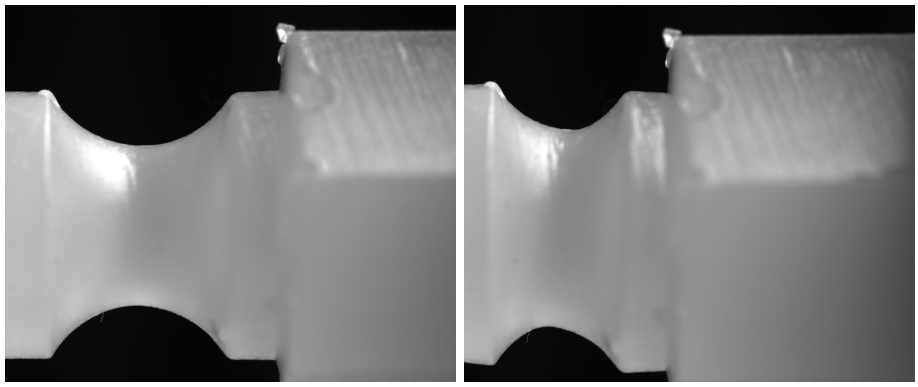

Figure 3.19: Images from an R4 compression test showing **(a)** the undeformed specimen and **(b)** the deformed specimen at the last frame of the test. Note the slight eccentricity in **(b)**.

3.6 Summary

- The studied material exhibited a typical polymer stress-strain response. The initial response was linear elastic, followed by inelastic flow and then strain hardening due to the alignment of the polymer chains. Where the material behaviour differed from most polymers, however, was in the brittle fracture mode occurring after large inelastic strains.
- The print orientation had no significant effects on the mechanical behaviour of the material. The material can thus be considered isotropic.
- The flow stress was found to be heavily strain-rate dependent, as increasing the strain rate by a decade led to a 40% increase in the flow stress. A strain-rate-dependent softening behaviour was observed immediately after the onset of inelastic flow which manifests as a drop in the force levels in the force-displacement curves and a reduction of the tangent modulus in the stress-strain curves. The initial elastic stiffness was also found to be strain-rate sensitive.
- Viscoelastic hysteresis was observed from loading/unloading tests. The measured self-heating was relatively low, as the highest temperature increase was only 4 °C for the highest strain rate tested.
- Significant stress relaxation was observed in an arrested loading/unloading test. The stress seemed to relax towards an equilibrium stress, which interestingly resulted in increased stress levels during the relaxation period in the unloading phase.
- Notch tensile and compression tests revealed a pressure-sensitive flow stress. The tests also showed that the scatter in the net failure stress decreased as the notch radius decreased. This observation suggests that fracture initiation is governed by a size effect, as the volume in which fracture initiates is smaller the sharper the notch radius is.

4 Validation tests

The tests presented in the previous chapter provide a comprehensive experimental database for use in the calibration of a constitutive model. After a constitutive model is calibrated, it should be validated against experimental results outside the calibration data. For this purpose, several validation tests have been performed, which feature more complex stress states than the material tests. This chapter presents the experimental setup and results for the validation tests performed in this work.

4.1 Lattice structure compression tests

Lattice structures are a class of architectured cellular solids with periodic microstructure. Lattice structures can be designed to provide strength- and stiffness-to-weight ratios that surpass natural materials [32] and the production of such structures has been made easier in the last decade thanks to additive manufacturing. One type of lattice structure that has been studied widely due to its potential application in lightweight engineering structures is the so-called octet-truss lattice structure [33, 34]. Due to its relevance for additive manufacturing, as well as its complex geometry, the octet-truss lattice structure is chosen for quasi-static and dynamic compression tests to validate the constitutive model presented later in this work.

4.1.1 Experimental programme and setup

The unit cell of the studied octet-truss lattice structure and its dimensions are shown in Figure 4.1. The relative density of the unit cell, i.e., the ratio of the density of the cell to the density of the bulk material, is 0.235. The full lattice structure is obtained by stacking the unit cells in a $4\times4\times4$ cubic pattern, which results in a lattice structure with dimensions $40\,\text{mm}\times40\,\text{mm}\times40\,\text{mm}$. A CAD model of the full lattice structure is shown in Figure 4.2.

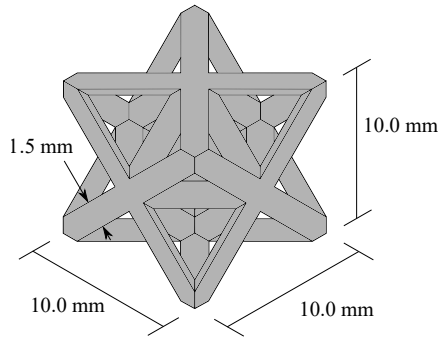

Figure 4.1: Dimensions of the octet-truss unit cell.

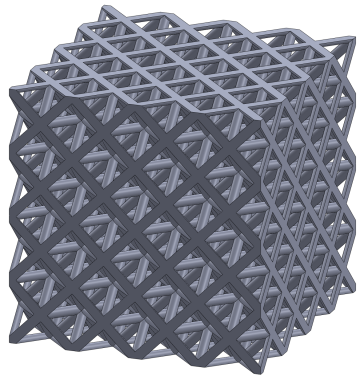

Figure 4.2: CAD model of the octet-truss lattice structure.

Specimens for compression testing were printed with the Form 3 SLA printer using the exact same print parameters and procedures as described in Chapter 3.1.

Quasi-static compression tests were carried out with cross-head velocities of 3 mm/min, 30 mm/min and 300 mm/min, with three repeat tests for each velocity. A cross-head velocity of 300 mm/min is quite high and could arguably not be considered quasi-static, but the test series is still referred to as quasi-static to distinguish it from the dynamic test series. The quasi-static tests were conducted in an Instron 5560 machine with a 10 kN load cell. The tests were monitored with a single camera with a logging frequency chosen such that approx. 600 frames were obtained for each cross-head velocity. Force and cross-head displacements were logged from the machine and synchronised to the image acquisition fre-

quency. The specimens were compressed between two hardened steel platens until the maximum force of the load cell was reached, after which the specimens were unloaded. The experimental setup is illustrated in Figure 4.3.

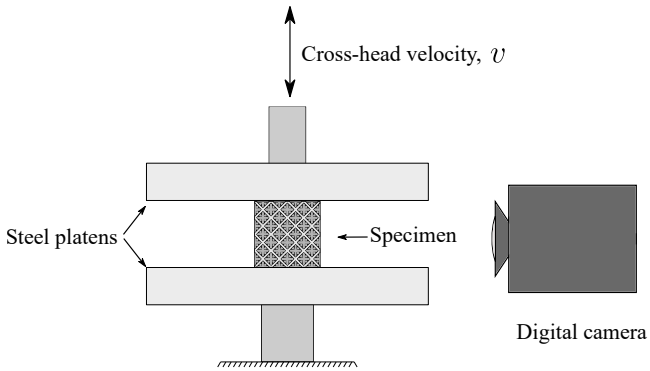

Figure 4.3: Drawing of the quasi-static compression test setup showing the steel platens, specimen and digital camera.

Dynamic tests were carried out in a CEAST 9350 drop tower system as illustrated in Figure 4.4. Three tests with an impact velocity of 5 m/s and two tests with an impact velocity of 4 m/s were performed. All tests featured a total impactor mass of 6.054 kg. The tests were monitored with a Phantom v161 high-speed camera with a frame rate of 25 000 frames per second and the force-time history was measured by a load cell with a frequency of 1 MHz. The setup is similar to the one used by Reyes and Børvik [35] but with a different striker and a flat impactor nose.

The load cell of the drop tower is located above the impactor nose, which leads to an underestimation of the force that is transferred to the test specimen. The force experienced by the specimen, F, can be expressed in terms of the measured force, P, and the mass above and below the load cell, m_1 and m_2 respectively. Applying Newton's second law to the system illustrated in Figure 4.5 gives

$$P - m_1 g = -m_1 a \tag{4.1}$$

and

$$F - P - m_2 g = -m_2 a \tag{4.2}$$

where a is the acceleration of the striker and impactor and g =9.81 m/s^2 is the gravitational acceleration. Combining the two above equations results in

$$F = \left(1 + \frac{m_2}{m_1}\right) P \tag{4.3}$$

The mass under the load cell in the tests performed is 0.818 kg and the mass above the load cell is 5.236 kg which gives $m_2/m_1 \approx 0.156$, i.e., the force experienced by the test specimen is 15.6% higher than the measured force. The drop tower machine only logs the force-time history of a test. To obtain the impactor displacement and velocity, the following integration scheme is used [35]

$$v_{n+1} = v_n - \left(\frac{F_{n+1} + F_n}{2m_p} - g\right) \Delta t, \quad w_{n+1} = w_n + \left(\frac{v_{n+1} + v_n}{2}\right) \Delta t \tag{4.4}$$

where v is the impactor velocity, w is the impactor displacement, Δt is the time increment and $m_p = 6.054$ kg is the total impactor mass. Note that the sign of the velocity and displacement is defined to be positive in the downward direction. To verify the accuracy of the presented integration scheme, the displacement of the impactor nose was also obtained by point tracking using the in-house DIC software eCorr [36] and compared with the integrated displacement. A comparison between the two aforementioned methods of extracting the impactor displacement is shown in Figure 4.6 for one of the tests with an initial velocity of 4 m/s. It is seen that the displacement obtained from the integration scheme closely matches the one obtained from DIC and, as such, is deemed suitable for further use.

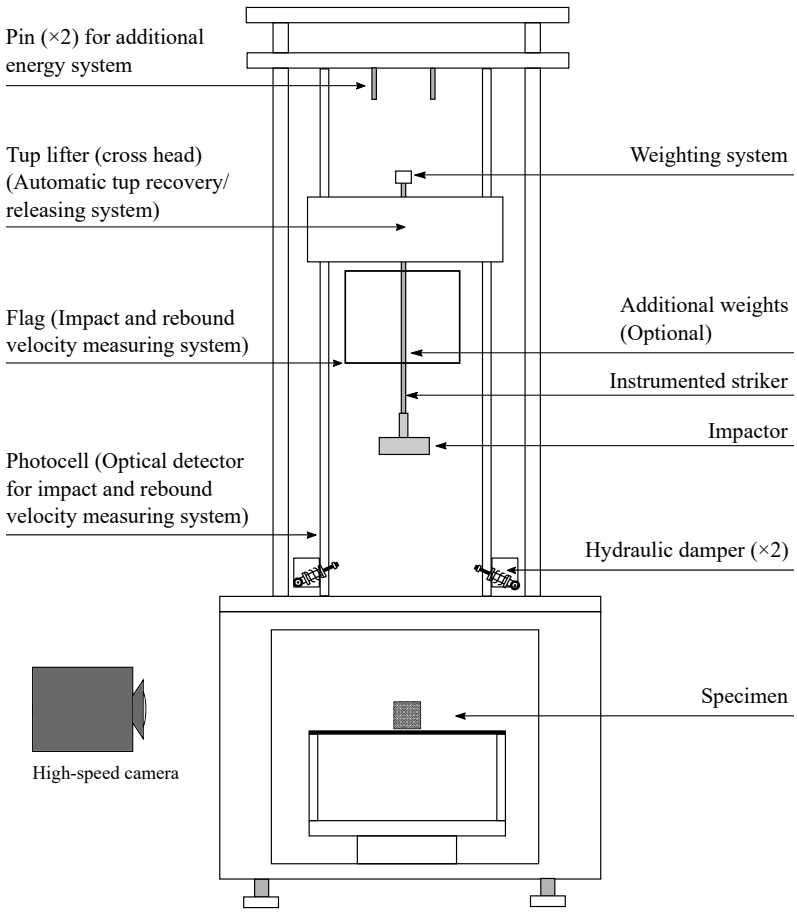

Figure 4.4: Drawing of the dynamic compression test setup showing the CEAST 9350 drop tower machine.

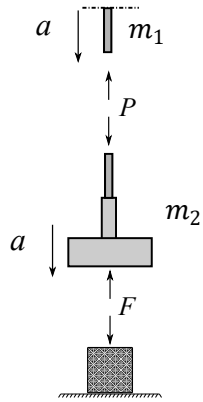

Figure 4.5: Free body diagram of a test specimen impacted in the drop tower machine.

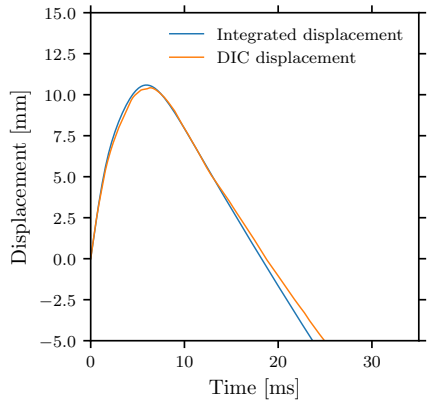

Figure 4.6: Comparison between the impactor displacement obtained from the integration scheme and from DIC.

4.1.2 Results and discussion

The results from the quasi-static compression tests are shown in Figure 4.7 in terms of force vs. displacement curves. The response follows a typical cellular solid behaviour. The initial response is elastic until a peak force is reached. Afterwards, the force levels drop and remain constant for a significant amount of deformation in what is referred to as the plateau region of the force-displacement

curve. The plateau lasts until the densification stage is reached – wherein the struts make contact with each other which significantly increases the stiffness of the structure. The strain-rate sensitive flow stress of the material is seen clearly from the increase in force levels as the cross-head velocity is increased. Strain-rate dependent softening is seen after the peak force is reached similar to what was observed in the tensile tests from Figure 3.14.

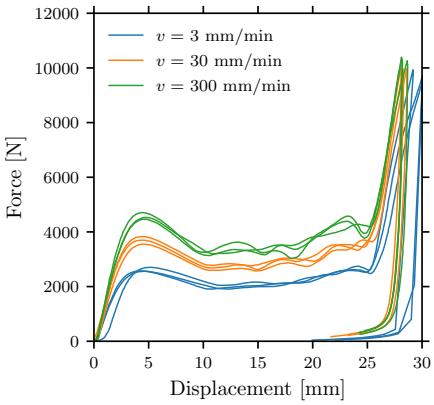

Figure 4.7: Force vs. displacement curves from quasi-static compression tests of octet-truss lattice structures with different cross-head velocities.

Figure 4.8 (a) and (b) shows the amount of deformation the lattice structures undergo during a compression test. Remarkably, most of the deformation is recovered after the test due to the viscoelastic properties of the material, as can be seen in Figure 4.9.

(a) **(b)**

Figure 4.8: Images captured by the digital camera from a compression test with $v = 3\,\mathrm{mm/min}$ from **(a)** before the test started and **(b)** at the point of maximum cross-head displacement.

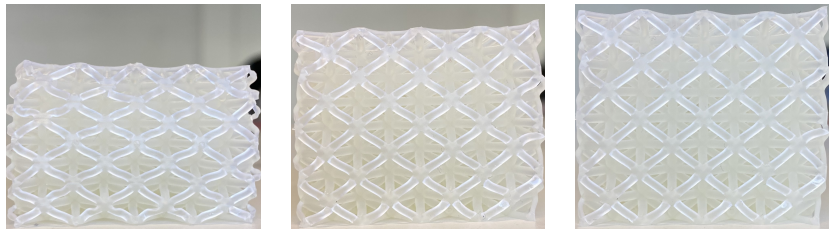

(a) **(b)** **(c)**

Figure 4.9: Images of an octet-truss lattice specimen after being compressed with a cross-head velocity of $v = 3\,\mathrm{mm/min}$ taken **(a)** immediately after testing, **(b)** 10 min after testing and **(c)** 60 min after testing.

The results from the dynamic compression tests are shown in Figure 4.10 in terms of force vs. displacement curves. The peak force in the dynamic tests is much higher than for the quasi-static tests, as is the force drop after the peak force is reached. The first of the previous observations can be attributed to the strain-rate sensitivity of the material, while the second observation stems from the difference in deformation modes between the dynamic and quasi-static tests. For ease of comparison, the force-displacement curve from a $5\,\mathrm{m/s}$ impact test is plotted together with the results from the quasi-static tests in Figure 4.11. The comparison once again demonstrates the strain-rate dependency of the initial elastic stiffness of the material, as the initial slopes of the dynamic tests are higher than those of the quasi-static tests.

The deformation of the lattice structures at the point of peak force and max. displacement for $v_0 = 4\,\mathrm{m/s}$ and $v_0 = 5\,\mathrm{m/s}$ is shown in Figure 4.12 and 4.13 respectively. The images show that the sharp force drop is caused by fractures in the structure, which prevents the neat folding of the struts observed in the quasi-static tests. The difference between an initial velocity of $4\,\mathrm{m/s}$ and $5\,\mathrm{m/s}$ has a significant effect on the maximum impactor displacement and consequently the amount of fracture occurring in the lattice structure. Even though the difference is only $1\,\mathrm{m/s}$, this is still a 25% increase in velocity which again results in a 56.25% increase in kinetic energy. It follows that the work done by the lattice structure on the impactor increases by the same ratio, which results in significantly more deformation of the lattice structure.

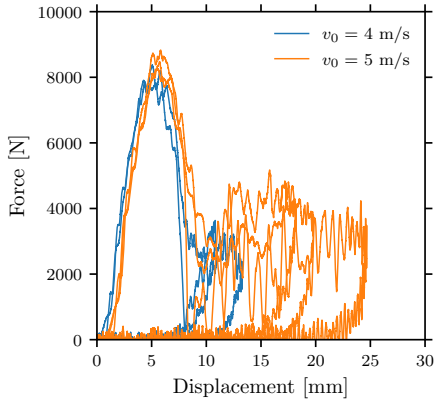

Figure 4.10: Force vs. displacement curves from dynamic compression tests of octet-truss lattice structures with two different impactor initial velocities.

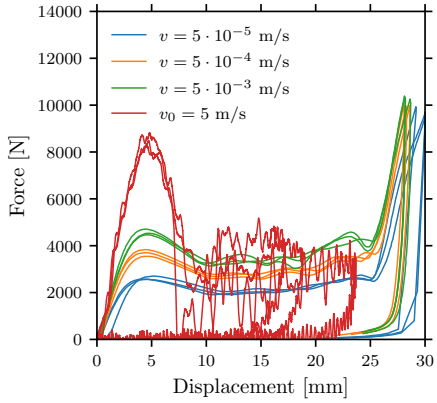

Figure 4.11: Force vs. displacement curves comparing the quasi-static compression tests and dynamic compression tests with $v_0 = 5\,\mathrm{m/s}$.

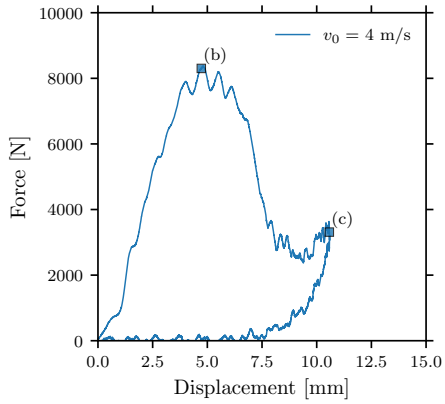

(a)

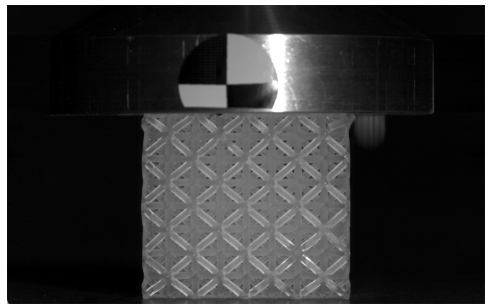

(b)

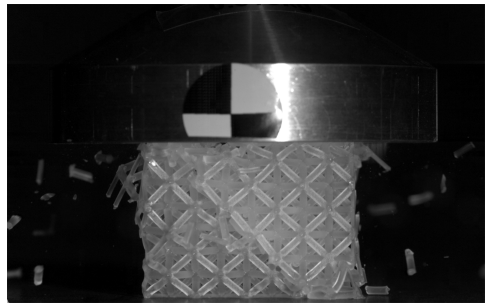

(c)

Figure 4.12: **(a)**: Force vs. displacement curve from a dynamic compression test with $v_0 = 4\,\mathrm{m/s}$ and **(b)-(c)**: the deformed shape of the lattice structure at points in the deformation history indicated in the force vs. displacement curve.

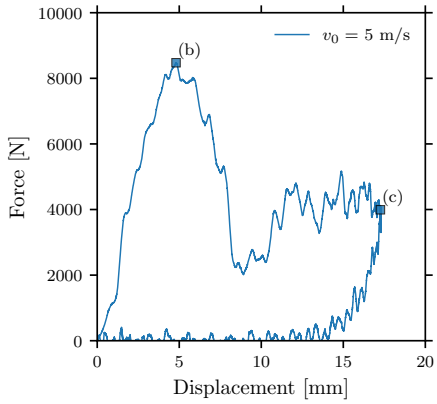

(a)

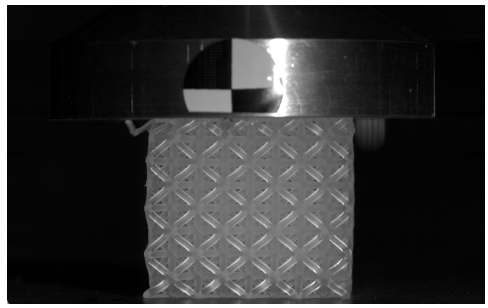

(b)

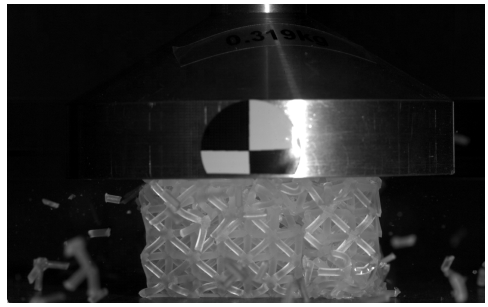

(c)

Figure 4.13: **(a)**: Force vs. displacement curve from a dynamic compression test with $v_0 = 5\,\mathrm{m/s}$ and **(b)**-**(c)**: the deformed shape of the lattice structure at points in the deformation history indicated in the force vs. displacement curve.

4.2 Three-point-bending tests

The lattice structure compression tests provide complex stress states valuable for validation purposes but at the same time, a large part of the mechanical response of such structures is governed by geometric effects like buckling. In order to provide a more controlled validation of the material behaviour itself, three-point bending tests on specimens with off-centre notches were carried out. Such tests provide a mix of compressive and tensile stresses from bending in addition to triaxial effects around the notch. The off-centre notch will also result in slanted crack propagation due to the presence of shear stresses in the notch root, which will provide valuable data for the validation of the fracture model.

4.2.1 Experimental programme and setup

Two specimen types were considered in this experimental programme; one with a notch radius of 1.25 mm and one with a notch radius of 2.5 mm. These are referred to as R1.25 and R2.50 specimens, respectively. The geometry and dimensions of the specimens are shown in Figure 4.14.

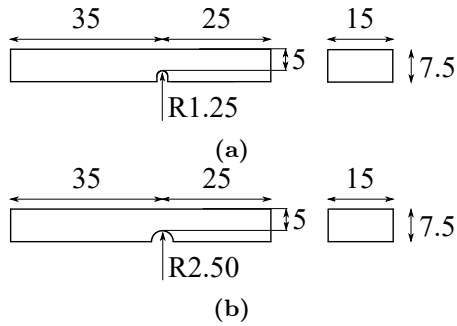

Figure 4.14: Geometries of **(a)** the R1.25 bending specimen and **(b)** the R2.50 bending specimen. Dimensions in mm.

The tests were carried out on an Instron 5944 universal testing system with a 2 kN load cell and a specialised three-point bending rig. The rig consists of a V-shaped punch and two supports. The punch has an internal angle of 60° and a tip radius of 2.5 mm and the supports have circular tips with a radius of 2.5 mm. The centre distance between the supports was 50 mm. The setup is visualised in Figure 4.15 with a photo of the experimental setup and a drawing of the setup with dimensions. The tests were performed with displacement control with a constant cross-head velocity of 3 mm/min. A digital camera with a frame rate of

2 Hz was used to monitor the tests. The specimens were painted with a black-and-white speckle pattern to allow for DIC analyses of the images captured by the camera.

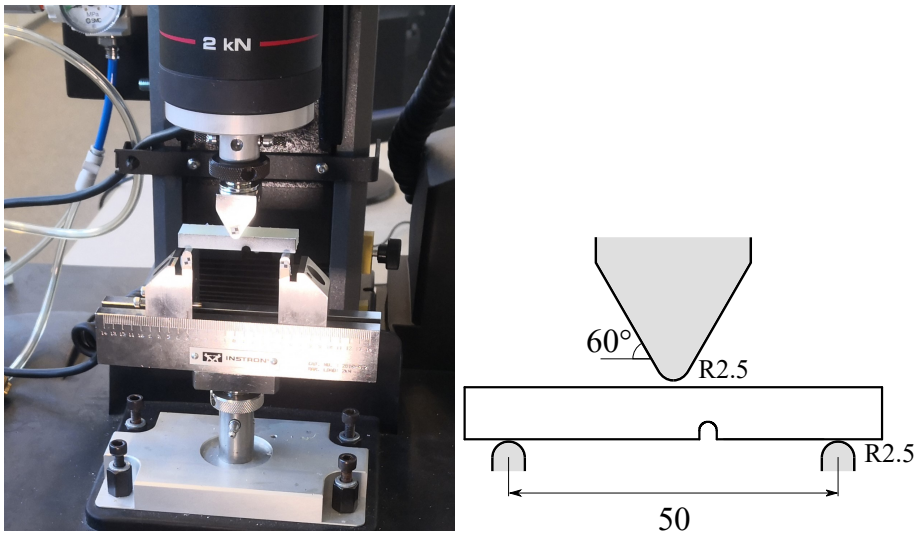

Figure 4.15: **(a)** Experimental setup of the three-point bending tests and **(b)** drawing with dimensions in mm.

4.2.2 Results and discussion

Force vs. displacement curves from the three-point bending tests are shown in Figure 4.16 (a). The general behaviour is similar for both specimen types where an initial elastic response is followed by yielding and subsequent fracture. The same trend as in the notch tension tests is observed, where the specimen with the sharper notch radius exhibits lower ductility and higher force levels. Additionally, the scatter in both the force and displacement at failure is lower in the R1.25 specimen than in the R2.50 specimen, as seen in Figure 4.16 (b). The explanation for this behaviour is the same as for the tension tests, namely that the strains are more localised in the sharpest notched specimen which results in less scatter in the fracture stress.

Field maps of the maximum principal strains from DIC analyses are shown in Figure 4.17 for both specimen types. The DIC analyses were performed in eCorr [36] with a mesh imported from Abaqus CAE. The images are taken from the

point in time corresponding to a cross-head displacement of 5 mm. The results show that the strain magnitude is larger in the R1.25 specimen than in the R2.50 specimen, due to the strain localisation induced by the sharper notch. This observation that the R1.25 specimens experience larger strains for the same cross-head displacement as the R2.50 specimens means that the stresses around the notch are also higher in the R1.25 specimens which again explains why these specimens failed at a lower cross-head displacement than the R2.50 specimens.

Pictures of an R1.25 and R2.50 specimen after fracture are shown in Figure 4.18. Only two specimens are shown, but the fracture patterns were similar in repeat tests. The fracture initiates in the centre of the notches and initially propagates normal to the notch surface before slanting towards the direction of the punch due to shear stresses changing the direction of the major principal stress. The crack changes direction again when approaching the top surface of the specimens as the cross-sectional height becomes so small that the shear stresses become negligible.

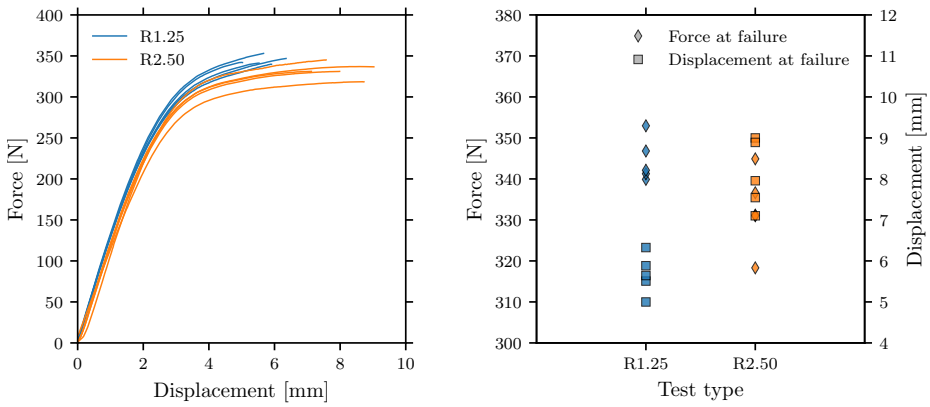

Figure 4.16: **(a)** Force vs. displacement curves from the three-point bending tests with off-centred notched specimens and **(b)** force at failure and displacement at failure from the three-point bending tests with off-centred notched specimens.

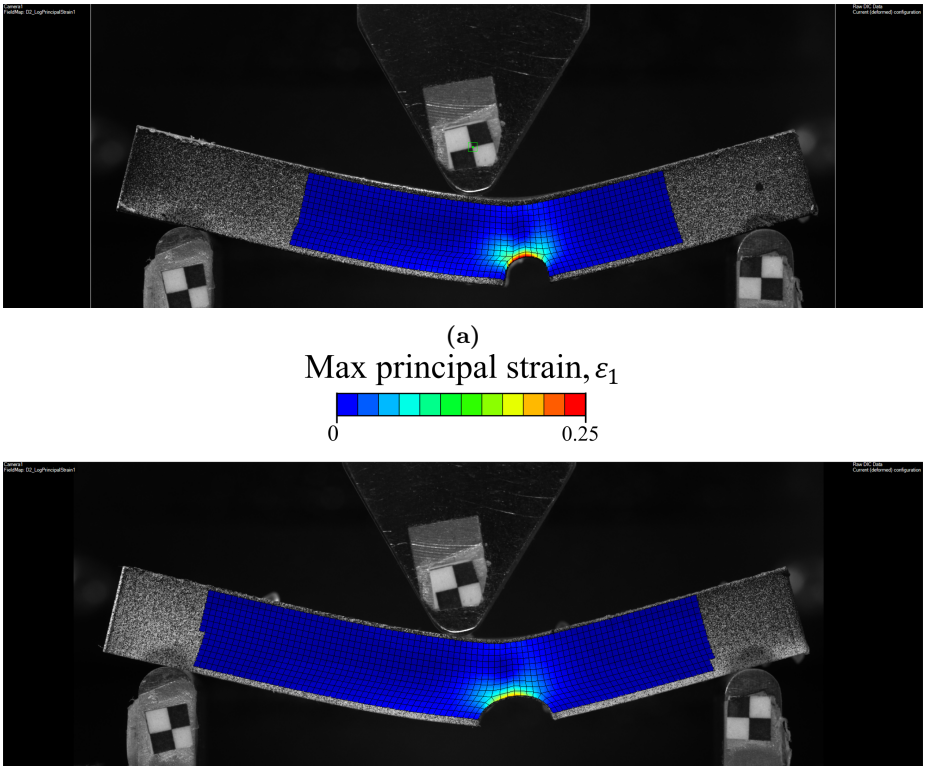

Figure 4.17: Results from DIC analyses of the three-point bending specimens showing field maps of the maximum principal strain from **(a)** the R1.25 specimen and **(b)** the R2.50 specimen. The cross-head displacement was 5 mm for both specimens.

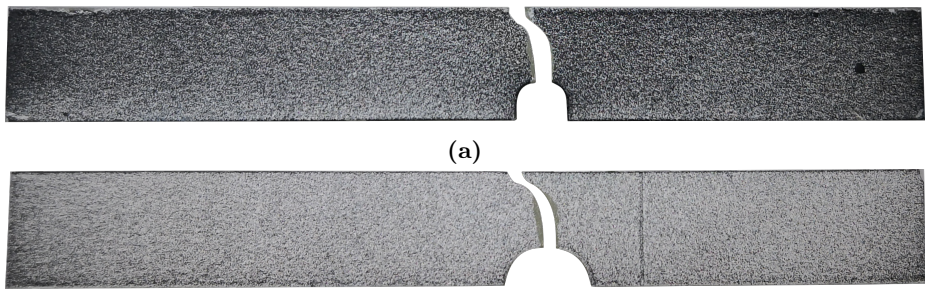

(a)

(b)

Figure 4.18: Fracture path in **(a)** an R1.25 specimen and **(b)** and R2.50 specimen.

4.3 Summary

- Compression tests of octet truss-lattice structures and three-point bending tests on notched beams were performed to obtain experimental data which can be used to validate a constitutive model.
- Quasi-static lattice compression tests exhibited a typical cellular material behaviour and showed the same strain-rate sensitivity as the material tests. The deformation mode was a neat compaction of the structure where the struts buckled and folded together.
- Dynamic lattice compression tests exhibited a very brittle behaviour compared with the quasi-static tests. The strain-rate sensitivity of the material in combination with high strain rates caused the struts to fracture before buckling, which changed the deformation mode.
- The two notched three-point bending specimens exhibited quite similar force-displacement curves, but the R1.25 specimens failed at lower crosshead displacement and at slightly higher force at failure than the R2.50 specimens. These results match the findings from the notch tension test series in the previous chapter.

5 Constitutive model: Formulation

This chapter presents the constitutive model developed during this work. First, an overview of the model is given, followed by a detailed description of the model's constitutive relations and numerical implementation.

5.1 Overview

The experimental results from the material tests presented in Chapter 3 were used as a reference for determining the necessary components of the constitutive model. The model should be able to describe an initial elastic response followed by rate- and pressure-dependent inelastic flow behaviour. Thinking in terms of rheological models, this can be modelled as an elastic spring in series with a non-linear viscoelastic dashpot. As the elastic strains constitute about 10% of the total strains, a hyperelastic formulation should be used to ensure energy conservation in a closed deformation cycle [26]. The strain-hardening response can be modelled by including an elastic spring in parallel with the viscoelastic network [13]. The parallel spring will also act as a rate-independent equilibrium stress, which allows the model to describe the stress-relaxation behaviour observed from the experimental results.

By combining the aforementioned components, we end up with the rheological model shown in Figure 5.1. Both Part A and Part B are governed by the total deformation gradient, viz.

$$\mathbf{F} = \mathbf{F}_{\mathrm{A}} = \mathbf{F}_{\mathrm{B}} \tag{5.1}$$

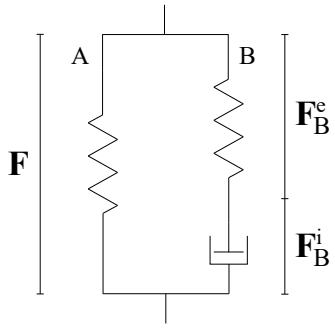

Figure 5.1: Rheological model.

The deformation gradient of Part B is multiplicatively decomposed into an elastic part, $\mathbf{F}_{\mathrm{B}}^{\mathrm{e}}$, and an inelastic part, $\mathbf{F}_{\mathrm{B}}^{\mathrm{i}}$, by the use of an intermediate configuration, viz.

$$\mathbf{F}_{\mathrm{B}} = \mathbf{F}_{\mathrm{B}}^{\mathrm{e}}\mathbf{F}_{\mathrm{B}}^{\mathrm{i}} \tag{5.2}$$

Figure 5.2 illustrates the kinematics of Part B. A material point is mapped from the reference configuration, Ω_0, to the current configuration, Ω, by the total deformation gradient, $\mathbf{F}_{\mathrm{B}}$. We then imagine that the material point in the current configuration is elastically unloaded to an intermediate configuration, $\tilde{\Omega}$, by the inverse of the elastic part of the deformation gradient of Part B, $(\mathbf{F}_{\mathrm{B}}^{\mathrm{e}})^{-1}$. The mapping from the reference configuration to the intermediate configuration is consequently performed by the inelastic part of the deformation gradient of Part B, $\mathbf{F}_{\mathrm{B}}^{\mathrm{i}}$.

The Helmholtz free energy function per unit volume of the model is additively composed as

$$\psi = \psi_{\mathrm{A}} + \psi_{\mathrm{B}} \tag{5.3}$$

which also results in an additive decomposition of the Cauchy stress tensor

$$\boldsymbol{\sigma} = \boldsymbol{\sigma}_{\mathrm{A}} + \boldsymbol{\sigma}_{\mathrm{B}} \tag{5.4}$$

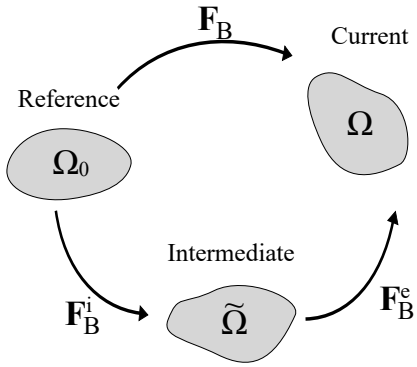

Figure 5.2: The kinematics of Part B.

5.2 Part A

Part A describes the strain hardening of the material due to the alignment of the polymer chains. For this, the well-known Arruda-Boyce eight-chain hyperelastic model [37] is used. The Helmholtz free energy is given as

$$\psi_\mathrm{A} = \theta\mu\lambda_\mathrm{L}^2\left[\frac{\bar{\lambda}_\mathrm{c}}{\lambda_\mathrm{L}}\beta + \ln\left(\frac{\beta}{\sinh(\beta)}\right)\right] \tag{5.5}$$

where θ is the absolute temperature, μ is the initial shear modulus and λ_L is the locking stretch. The effective chain stretch is defined as

$$\bar{\lambda}_\mathrm{c} = \sqrt{\bar{I}_1/3} \tag{5.6}$$

where $\bar{I}_1 = \mathrm{tr}(\bar{\mathbf{B}})$ is the first invariant of the isochoric left Cauchy-Green deformation tensor. The isochoric left Cauchy-Green deformation tensor is defined as $\bar{\mathbf{B}} = J^{-2/3}\mathbf{F}\mathbf{F}^\mathrm{T}$, where $J = \det(\mathbf{F})$ is the Jacobian determinant. The parameter β is defined as $\beta = \mathcal{L}^{-1}(\bar{\lambda}_\mathrm{c}/\lambda_\mathrm{L})$, where the Langevin function is

$$\mathcal{L}(x) = \coth(x) - 1/x \tag{5.7}$$

The expression for the Cauchy stress is then obtained from Eq. 2.86 as

$$\boldsymbol{\sigma}_{\mathrm{A}} = \frac{2}{J}\frac{\partial \psi_{\mathrm{A}}}{\partial \bar{I}_1}\bar{\mathbf{B}}' + \frac{\partial \psi_{\mathrm{A}}}{\partial J}\mathbf{I} \tag{5.8}$$

The first partial derivative is evaluated as

$$\frac{\partial \psi_{\mathrm{A}}}{\partial \bar{I}_1} = \frac{\partial \psi_{\mathrm{A}}}{\partial \bar{\lambda}_{\mathrm{c}}}\frac{\partial \bar{\lambda}_{\mathrm{c}}}{\partial \bar{I}_1} + \frac{\partial \psi_{\mathrm{A}}}{\partial \beta}\frac{\partial \beta}{\partial \bar{\lambda}_{\mathrm{c}}}\frac{\partial \bar{\lambda}_{\mathrm{c}}}{\partial \bar{I}_1} \tag{5.9}$$

We then evaluate the partial derivative $\partial \psi_{\mathrm{A}}/\partial \beta$:

$$\begin{aligned}\frac{\partial \psi_{\mathrm{A}}}{\partial \beta} &= \theta\mu\lambda_{\mathrm{L}}^2\left[\frac{\bar{\lambda}_{\mathrm{c}}}{\lambda_{\mathrm{L}}} + \frac{\sinh(\beta)}{\beta}\left(\frac{\sinh(\beta) - \beta\cosh(\beta)}{\sinh^2(\beta)}\right)\right] \\ &= \theta\mu\lambda_{\mathrm{L}}^2\left[\frac{\bar{\lambda}_{\mathrm{c}}}{\lambda_{\mathrm{L}}} - \coth(\beta) + \frac{1}{\beta}\right]\end{aligned} \tag{5.10}$$

Inserting the relation $\coth(\beta) - 1/\beta = \mathcal{L}(\beta) = \bar{\lambda}_{\mathrm{c}}/\lambda_{\mathrm{L}}$ gives

$$\frac{\partial \psi_{\mathrm{A}}}{\partial \beta} = \theta\mu\lambda_{\mathrm{L}}^2\left[\frac{\bar{\lambda}_{\mathrm{c}}}{\lambda_{\mathrm{L}}} - \frac{\bar{\lambda}_{\mathrm{c}}}{\lambda_{\mathrm{L}}}\right] = 0 \tag{5.11}$$

which means that only the first term of Eq. 5.9 is non-zero. The remainder of the equation is evaluated as

$$\frac{\partial \psi_{\mathrm{A}}}{\partial \bar{I}_1} = \theta\mu\lambda_{\mathrm{L}}\beta\frac{1}{6\bar{\lambda}_{\mathrm{c}}} \tag{5.12}$$

From here on, the temperature dependence of the model will not be considered, as the effect of temperature on the mechanical behaviour of the SLA resin studied in this work is out of scope. An isothermal shear modulus is introduced and defined as $\mu_{\mathrm{A}} = \theta\mu$. Since the Helmholtz free energy function has no dependence on the Jacobian determinant, the Cauchy stress can now be written as

$$\boldsymbol{\sigma}_{\mathrm{A}} = \frac{\mu_{\mathrm{A}}\lambda_{\mathrm{L}}}{3\bar{\lambda}_{\mathrm{c}}J}\mathcal{L}^{-1}\left(\frac{\bar{\lambda}_{\mathrm{c}}}{\lambda_{\mathrm{L}}}\right)\bar{\mathbf{B}}' \tag{5.13}$$

5.3 Part B

Part B describes the non-linear viscoelastic behaviour of the material and consists of a hyperelastic spring in series with a viscous dashpot. The Helmholtz free energy of the hyperelastic spring is given by the neo-Hookean potential as [27]

$$\psi_{\mathrm{B}} = \frac{\mu_{\mathrm{B}}}{2}(\bar{I}^{\mathrm{e}}_{\mathrm{B},1} - 3) + \frac{\kappa}{2}(J^{\mathrm{e}}_{\mathrm{B}} - 1)^2 \tag{5.14}$$

where μ_{B} is the shear modulus of Part B, κ is the bulk modulus, $\bar{I}^{\mathrm{e}}_{\mathrm{B},1} = \mathrm{tr}(\bar{\mathbf{B}}^{\mathrm{e}}_{\mathrm{B}})$ is the first invariant of the isochoric elastic left Cauchy-Green deformation tensor and $J^{\mathrm{e}}_{\mathrm{B}} = \det(\mathbf{F}^{\mathrm{e}}_{\mathrm{B}})$ is the elastic Jacobian determinant.

The Cauchy stress is derived from the energy function as

$$\boldsymbol{\sigma}_{\mathrm{B}} = \frac{2}{J_{\mathrm{B}}}\frac{\partial \psi_{\mathrm{B}}}{\partial \bar{I}^{\mathrm{e}}_{\mathrm{B},1}}\bar{\mathbf{B}}^{\mathrm{e}'}_{\mathrm{B}} + \frac{\partial \psi_{\mathrm{B}}}{\partial J^{\mathrm{e}}_{\mathrm{B}}}\mathbf{I} \tag{5.15}$$

which is straightforward to evaluate as

$$\boldsymbol{\sigma}_{\mathrm{B}} = \frac{\mu_{\mathrm{B}}}{J_{\mathrm{B}}}\bar{\mathbf{B}}^{\mathrm{e}'}_{\mathrm{B}} + \kappa(J^{\mathrm{e}}_{\mathrm{B}} - 1)\mathbf{I} \tag{5.16}$$

The total velocity gradient is defined as

$$\mathbf{L}_{\mathrm{B}} = \dot{\mathbf{F}}_{\mathrm{B}}(\mathbf{F}_{\mathrm{B}})^{-1} = \mathbf{L}^{\mathrm{e}}_{\mathrm{B}} + \mathbf{F}^{\mathrm{e}}_{\mathrm{B}}\tilde{\mathbf{L}}^{\mathrm{i}}_{\mathrm{B}}(\mathbf{F}^{\mathrm{e}}_{\mathrm{B}})^{-1} = \mathbf{L}^{\mathrm{e}}_{\mathrm{B}} + \mathbf{L}^{\mathrm{i}}_{\mathrm{B}} \tag{5.17}$$

where $\tilde{\mathbf{L}}^{\mathrm{i}}_{\mathrm{B}} = \dot{\mathbf{F}}^{\mathrm{i}}_{\mathrm{B}}(\mathbf{F}^{\mathrm{i}}_{\mathrm{B}})^{-1}$ is the inelastic velocity gradient defined on the intermediate configuration and $\mathbf{L}^{\mathrm{e}}_{\mathrm{B}} = \dot{\mathbf{F}}^{\mathrm{e}}_{\mathrm{B}}(\mathbf{F}^{\mathrm{e}}_{\mathrm{B}})^{-1}$ is the elastic velocity gradient defined on the current configuration. The inelastic velocity gradient on the current configuration, $\mathbf{L}^{\mathrm{i}}_{\mathrm{B}}$, is obtained through a push-forward operation on $\tilde{\mathbf{L}}^{\mathrm{i}}_{\mathrm{B}}$ with the elastic deformation gradient.

The elastic and inelastic velocity gradients of Part B are further decomposed into symmetric and antisymmetric parts – those being the rate of deformation tensor, $\mathbf{D}_{\mathrm{B}}$, and spin tensor, $\mathbf{W}_{\mathrm{B}}$, respectively. The expressions for the decomposition are

$$\mathbf{L}^{\mathrm{e}}_{\mathrm{B}} = \mathbf{D}^{\mathrm{e}}_{\mathrm{B}} + \mathbf{W}^{\mathrm{e}}_{\mathrm{B}} \tag{5.18}$$

$$\mathbf{L}_{\mathrm{B}}^{\mathrm{i}} = \mathbf{D}_{\mathrm{B}}^{\mathrm{i}} + \mathbf{W}_{\mathrm{B}}^{\mathrm{i}} \tag{5.19}$$

Both the inelastic rate of deformation tensor and inelastic spin tensor need to be prescribed to achieve a unique solution. Due to isotropic material behaviour, the inelastic spin tensor can be prescribed to be equal to the zero tensor [38, 39], viz.

$$\mathbf{W}_{\mathrm{B}}^{\mathrm{i}} = \mathbf{0} \tag{5.20}$$

The inelastic rate of deformation tensor, on the other hand, is prescribed by a flow rule on the form

$$\mathbf{D}_{\mathrm{B}}^{\mathrm{i}} = \dot{\gamma}_{\mathrm{B}} \mathbf{N}_{\mathrm{B}}^{\mathrm{i}} \tag{5.21}$$

where $\dot{\gamma}_{\mathrm{B}}$ is an effective inelastic strain rate and $\mathbf{N}_{\mathrm{B}}^{\mathrm{i}}$ is the direction of inelastic flow tensor calculated from an inelastic potential function as

$$\mathbf{N}_{\mathrm{B}}^{\mathrm{i}} = \frac{\partial g}{\partial \boldsymbol{\sigma}_{\mathrm{B}}} \tag{5.22}$$

The potential function, g, is taken as the equivalent von Mises stress, viz.

$$g = \sqrt{\frac{3}{2} \boldsymbol{\sigma}'_{\mathrm{B}} : \boldsymbol{\sigma}'_{\mathrm{B}}} = \sigma_{\mathrm{vm,B}} \tag{5.23}$$

The resulting direction of inelastic flow is thus

$$\mathbf{N}_{\mathrm{B}}^{\mathrm{i}} = \frac{3}{2} \frac{\boldsymbol{\sigma}'_{\mathrm{B}}}{\sigma_{\mathrm{vm,B}}} \tag{5.24}$$

From Eqs. 5.21 and 5.24, it is apparent that the trace of the inelastic rate of deformation tensor is zero. Consequently, no increase in volume due to inelastic deformations will occur. This can be seen from the expression for the rate of change of the inelastic Jacobian determinant [25]

$$\dot{J}_{\mathrm{B}}^{\mathrm{i}} = J_{\mathrm{B}}^{\mathrm{i}} \mathrm{tr}(\mathbf{D}_{\mathrm{B}}^{\mathrm{i}}) = 0 \tag{5.25}$$

which also means that the elastic Jacobian determinant is the same as the total Jacobian determinant, viz.

$$J_{\mathrm{B}}^{\mathrm{i}} = 1 \rightarrow J_{\mathrm{B}}^{\mathrm{e}} = J \tag{5.26}$$

The inelastic rate of deformation tensor is not fully prescribed yet, as a constitutive relation is still needed for the effective inelastic strain rate. For this purpose, a non-linear viscoelastic power law is used. The expression reads

$$\dot{\gamma}_{\mathrm{B}} = \dot{\gamma}_0 \left(\frac{\sigma_{\mathrm{vm,B}}}{\bar{\tau}} \right)^m \tag{5.27}$$

where $\dot{\gamma}_0 > 0$ is a reference strain rate, m is a material constant and $\bar{\tau}$ is the effective shear strength. The effective shear strength is taken to depend on hydrostatic stress as

$$\bar{\tau} = \tau - \alpha \sigma_{\mathrm{H,B}} > 0 \tag{5.28}$$

where $\sigma_{\mathrm{H,B}} = \mathrm{tr}(\boldsymbol{\sigma}_{\mathrm{B}})/3$ and α is a pressure sensitivity parameter. Strain softening is captured through the phenomenological evolution of the shear shear strength, τ, proposed by Boyce et al. [15]

$$\dot{\tau} = h \left(1 - \frac{\tau}{\tau_{\mathrm{ss}}} \right) \dot{\gamma}_{\mathrm{B}} \tag{5.29}$$

where h is a softening parameter and τ_{ss} is the saturation value of τ. The initial value of τ is the parameter $\tau_0 > \tau_{\mathrm{ss}}$.

To satisfy the second order of thermodynamics, the inelastic dissipation of the presented model must be non-negative. The dissipation inequality in the current configuration is stated as [26]

$$\mathcal{D} = \boldsymbol{\sigma}_{\mathrm{B}} : \mathbf{D}_{\mathrm{B}}^{\mathrm{i}} \geq 0 \tag{5.30}$$

Inserting the flow rule from Eq. 5.21 and Eq. 5.24 into the equation above gives

$$\mathcal{D} = \dot{\gamma}_{\mathrm{B}} \frac{3}{2} \frac{\boldsymbol{\sigma}_{\mathrm{B}} : \boldsymbol{\sigma}'_{\mathrm{B}}}{\sigma_{\mathrm{vm,B}}} = \sigma_{\mathrm{vm,B}} \dot{\gamma}_{\mathrm{B}} \geq 0 \tag{5.31}$$

which shows that the dissipation inequality is always satisfied since both the equivalent von Mises stress and the effective inelastic strain rate are non-negative

by definition.

The material parameters of the constitutive model are summarised in Table 5.1 and the governing equations are summarised in Box 5.1.

Table 5.1: Hyper-viscoelastic material parameters.

Parameter	Unit	Description
μ_{A}	MPa	Shear modulus Part A
μ_{B}	MPa	Shear modulus Part B
λ_{L}	-	Locking stretch
κ	MPa	Bulk modulus
$\dot{\gamma}_0$	s^{-1}	Reference strain rate
m	-	Strain-rate sensitivity parameter
h	MPa	Softening modulus
τ_0	MPa	Initial shear strength
τ_{ss}	MPa	Saturated shear strength
α	-	Pressure sensitivity parameter

Box 5.1: Governing equations of the hyper-viscoelastic model.

$$\boldsymbol{\sigma}_{\mathrm{A}} = \frac{\mu_{\mathrm{A}}\lambda_{\mathrm{L}}}{3\bar{\lambda}_{\mathrm{c}}J}\mathcal{L}^{-1}\left(\frac{\bar{\lambda}_{\mathrm{c}}}{\lambda_{\mathrm{L}}}\right)\bar{\mathbf{B}}' \qquad \text{Cauchy stress – Part A}$$

$$\boldsymbol{\sigma}_{\mathrm{B}} = \frac{\mu_{\mathrm{B}}}{J_{\mathrm{B}}}\bar{\mathbf{B}}^{\mathrm{e}'}_{\mathrm{B}} + \kappa(J^{\mathrm{e}}_{\mathrm{B}} - 1)\mathbf{I} \qquad \text{Cauchy stress – Part B}$$

$$\mathbf{D}^{\mathrm{i}}_{\mathrm{B}} = \dot{\gamma}_{\mathrm{B}}\frac{3}{2}\frac{\boldsymbol{\sigma}'_{\mathrm{B}}}{\sigma_{\mathrm{vm,B}}} \qquad \text{Inelastic flow rule}$$

$$\dot{\gamma}_{\mathrm{B}} = \dot{\gamma}_0\left(\frac{\sigma_{\mathrm{vm,B}}}{\bar{\tau}}\right)^m \qquad \text{Effective inelastic strain rate}$$

$$\bar{\tau} = \tau - \alpha\sigma_{\mathrm{H,B}} \qquad \text{Pressure sensitive shear strength}$$

$$\dot{\tau} = h\left(1 - \frac{\tau}{\tau_{\mathrm{ss}}}\right)\dot{\gamma}_{\mathrm{B}} \qquad \text{Softening evolution}$$

5.4 Fracture initiation model

The size-dependent scatter in fracture stress observed in the experiments is captured by a stress-based fracture criterion together with a stochastic critical stress. The approach is adapted from the model proposed by Holmström et al [40]. Fracture occurs when an equivalent stress, $\bar{\sigma}$, reaches a critical stress level, $\bar{\sigma}_{\mathrm{c}}$. The equivalent stress is defined as

$$\bar{\sigma} = \sqrt{\sum_{I=1}^{3} \langle \sigma_I \rangle^2} \tag{5.32}$$

where $\langle \cdot \rangle$ is the positive Macaulay bracket and the principal stresses of the Cauchy stress tensor, σ_I, are ordered as $\sigma_1 \geq \sigma_2 \geq \sigma_3$. An equivalent strain measure, $\bar{\varepsilon}$, is defined to be power conjugate with the equivalent stress. Equivalence in mechanical power gives

$$\bar{\sigma}\dot{\bar{\varepsilon}} = \boldsymbol{\sigma} : \mathbf{D} \rightarrow \bar{\varepsilon} = \int_0^t \frac{1}{\bar{\sigma}} \boldsymbol{\sigma} : \mathbf{D} \mathrm{d}t \tag{5.33}$$

where $\mathbf{D}$ is the total rate of deformation tensor, $\mathbf{D} = (\mathbf{L} + \mathbf{L}^{\mathrm{T}})/2$, and $\mathbf{L}$ is the total velocity gradient, $\mathbf{L} = \dot{\mathbf{F}}\mathbf{F}^{-1}$.

When fracture is modelled by the way of element erosion, the energy release associated with fracture is dependent on the size of the eroded elements. To reduce the mesh dependency, a regularisation parameter, G_{f}, is introduced to ensure that the energy dissipated by an element is independent of the element size. The procedure is illustrated in Figure 5.3 where G_{f} is seen to represent the shaded area of the curve, i.e., the energy dissipated at fracture. When the critical equivalent stress is reached, linear strain softening takes place until the equivalent failure strain, $\bar{\varepsilon}_{\mathrm{u}}$, is reached. An expression for $\bar{\varepsilon}_{\mathrm{u}}$ is obtained by equating the fracture energy of the crack surface with the dissipated strain energy of the element [41]

$$G_{\mathrm{f}} A_{\mathrm{el}} = \frac{1}{2} \bar{\sigma}_{\mathrm{c}} (\bar{\varepsilon}_{\mathrm{u}} - \bar{\varepsilon}_{\mathrm{c}}) V_{\mathrm{el}} \tag{5.34}$$

where A_{el} is the area of the crack surface, V_{el} is the volume of the element and $\bar{\varepsilon}_{\mathrm{c}}$ is the equivalent strain corresponding to the critical stress $\bar{\sigma}_{\mathrm{c}}$. By assuming cubic elements with a characteristic size h_{el}, the equivalent failure strain is found as

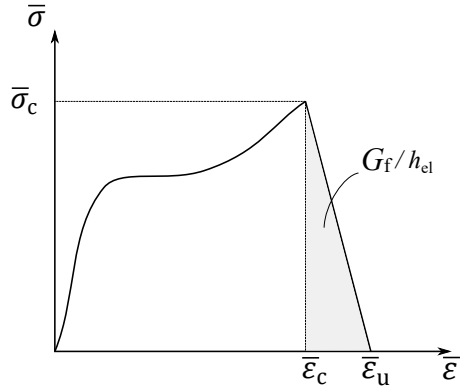

Figure 5.3: Equivalent stress vs equivalent strain curve showing how G_f is related to the dissipated energy at fracture.

$$\bar{\varepsilon}_u = \bar{\varepsilon}_c + \frac{2G_f}{\bar{\sigma}_c h_{el}} \tag{5.35}$$

Thus, the softening is dependent on the characteristic element size such that energy dissipated by fracture is independent of element size as long as the mesh remains regular. In addition to regularising the fracture, the softening behaviour improves the robustness of the material model as convergence issues can occur when an element is immediately eroded after having its critical stress reached. It is emphasised that the fracture energy parameter, G_f, is not related to the material behaviour and is strictly a numerical parameter. The value of G_f must be chosen such that the fracture is brittle enough to describe the experimentally observed brittle fracture without causing convergence issues. To prevent spurious element erosion due to stress waves, the equivalent stress needs to be equal or greater than the critical stress during a critical time interval, Δt_c. Unless stated otherwise, a value of 10^{-4} s is used for the critical time interval in all simulations carried out in this work.

In the softening stage, the stress tensor in the constitutive equations is replaced by an effective stress tensor defined as

$$\boldsymbol{\sigma}_{\text{eff}} = \frac{\boldsymbol{\sigma}}{(1-\delta)} \tag{5.36}$$

where δ is a damage variable defined as

$$\delta = \begin{cases} 0 & \text{for } \bar{\varepsilon} < \bar{\varepsilon}_{\mathrm{c}} \\ 1 - \dfrac{\bar{\varepsilon}_{\mathrm{u}} - \bar{\varepsilon}}{\bar{\varepsilon}_{\mathrm{u}} - \bar{\varepsilon}_{\mathrm{c}}} & \text{for } \bar{\varepsilon} \geq \bar{\varepsilon}_{\mathrm{c}} \end{cases} \tag{5.37}$$

An element is eroded when the damage variable reaches a critical value of $\delta = 0.9$. This value is chosen to provide elements with some residual stiffness before being eroded to mitigate element distortion prior to erosion.

Stochastic fracture is introduced by making the critical equivalent stress, $\bar{\sigma}_{\mathrm{c}}$, follow a left-truncated normal distribution. The probability density function of $\bar{\sigma}_{\mathrm{c}}$ is given as

$$f(\bar{\sigma}_{\mathrm{c}}) = \frac{1}{\bar{\sigma}_{\mathrm{c,std}}\sqrt{2\pi}} \exp\left[-\frac{1}{2}\left(\frac{\bar{\sigma}_{\mathrm{c}} - \bar{\sigma}_{\mathrm{c,mean}}}{\bar{\sigma}_{\mathrm{c,std}}} \right)^2 \right] \tag{5.38}$$

and is made left-truncated through the definition [40]

$$f_{\mathrm{LT}}(\bar{\sigma}_{\mathrm{c}}) = \begin{cases} 0 & \text{for } \bar{\sigma}_{\mathrm{c}} < \bar{\sigma}_{\mathrm{c,min}} \\ \dfrac{f(\bar{\sigma}_{\mathrm{c}})}{\int_{\bar{\sigma}_{\mathrm{c,min}}}^{\infty} f(\bar{\sigma}_{\mathrm{c}}) \mathrm{d}\bar{\sigma}_{\mathrm{c}}} & \text{for } \bar{\sigma}_{\mathrm{c}} \geq \bar{\sigma}_{\mathrm{c,min}} \end{cases} \tag{5.39}$$

The stochastic failure stress is distributed to the material points of a finite element model through an assignment mesh, as proposed by Knoll [42]. The assignment mesh has the shape of a rectangular cuboid and covers the entire finite element model. A random critical stress according to the distribution in Eq. 5.39 is assigned to each element in the assignment mesh. Each integration point in the finite element model that lies inside an element of the assignment mesh is then assigned the critical stress value of the assignment element. It is apparent that the element size of the assignment mesh controls the length scale of $\bar{\sigma}_{\mathrm{c}}$. Figure 5.4 (a) shows the critical stress distribution in a finite element model of a tensile test assigned with an assignment element size twice as large as the finite element size in the gauge area. Figure 5.4 (b) shows a histogram of the fracture stresses together with the nominal distribution used as input to generate the stochastic fracture stress values.

The parameters used in the fracture model are summarised in Table 5.3.

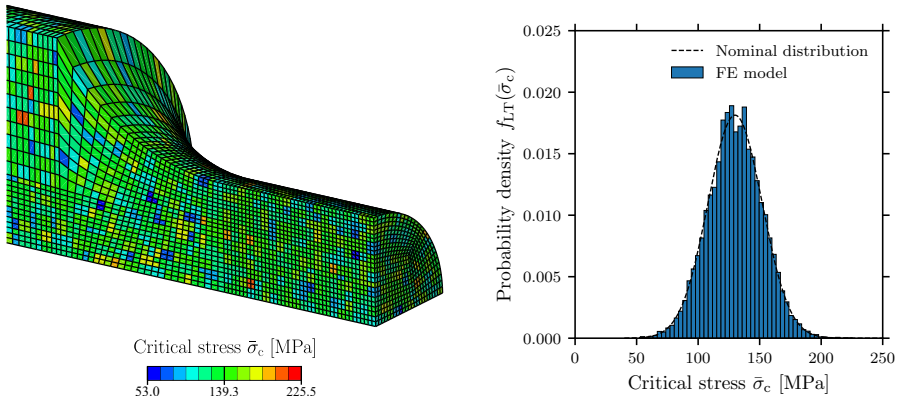

Figure 5.4: **(a)** Critical stress distribution in the gauge area of a FE model of a smooth tensile specimen and **(b)** a comparison between the nominal distribution and the realised distribution in the FE model with a normalised histogram.

Table 5.3: Fracture model parameters.

Parameter	Unit	Description
$\bar{\sigma}_{c,mean}$	MPa	Mean value of the stochastic failure stress
$\bar{\sigma}_{c,std}$	MPa	Standard deviation of the stochastic failure stress
$\bar{\sigma}_{c,min}$	MPa	Minimum value of the stochastic failure stress
G_f	N/mm	Fracture energy release parameter
Δt_c	s	Critical time interval

5.5 Numerical implementation

The constitutive model is implemented in Abaqus/Explicit. A quasi-implicit numerical integration scheme inspired by Johnsen et al. [43] was used to integrate the flow rule in Eq. 5.21. Inserting the relation between the inelastic deformation gradient and the inelastic rate of deformation tensor into the equation gives

$$\dot{\mathbf{F}}_B^i = \dot{\gamma}_B (\mathbf{F}_B^e)^{-1} \mathbf{N}_B^i \mathbf{F}_B^e \mathbf{F}_B^i \tag{5.40}$$

which can be solved with a backward Euler approximation as

$$\mathbf{F}^{\mathrm{i}}_{\mathrm{B},n+1} = \mathbf{F}^{\mathrm{i}}_{\mathrm{B},n} + (\dot{\gamma}_{\mathrm{B}}(\mathbf{F}^{\mathrm{e}}_{\mathrm{B}})^{-1}\mathbf{N}^{\mathrm{i}}_{\mathrm{B}}\mathbf{F})\big|_{n+1}\Delta t_{n+1} \tag{5.41}$$

The above equation may be rearranged and solved iteratively as

$$(\mathbf{F}^{\mathrm{i},I}_{\mathrm{B},n+1})^{-1} = (\mathbf{I} - \dot{\gamma}^{I}_{\mathrm{B},n+1}\Delta t_{n+1}\mathbf{F}^{-1}_{n+1}\mathbf{N}^{\mathrm{i},I-1}_{\mathrm{B},n+1}\mathbf{F}_{n+1})(\mathbf{F}^{\mathrm{i}}_{\mathrm{B},n})^{-1} \tag{5.42}$$

where the superscript I signifies the Ith iteration. Note that in order to avoid equation solving, the direction of inelastic flow, $\mathbf{N}^{\mathrm{i}}_{\mathrm{B}}$, lags one iteration behind the other iterative variables. With the inverse inelastic deformation gradient at hand, the elastic part is calculated as

$$\mathbf{F}^{\mathrm{e},I}_{\mathrm{B},n+1} = \mathbf{F}_{n+1}\left(\mathbf{F}^{\mathrm{i},I}_{\mathrm{B},n+1}\right)^{-1} \tag{5.43}$$

which is used in the calculation of the Cauchy stress tensor $\boldsymbol{\sigma}^{I}_{\mathrm{B,n+1}}$.

The effective inelastic strain rate of the next iteration is calculated using the secant method

$$\dot{\gamma}^{I+1}_{\mathrm{B},n+1} = \dot{\gamma}^{I}_{\mathrm{B},n+1} - \frac{\dot{\gamma}^{I}_{\mathrm{B},n+1} - \dot{\gamma}^{I-1}_{\mathrm{B},n+1}}{r^{I}_{n+1} - r^{I-1}_{n+1}} r^{I}_{n+1} \tag{5.44}$$

where r^{I}_{n+1} is a residual function defined as

$$r^{I}_{n+1} = \dot{\gamma}^{I}_{\mathrm{B},n+1} - \dot{\gamma}_0\left(\frac{\sigma^{I}_{\mathrm{vm,B,n+1}}}{\bar{\tau}^{I}_{n+1}}\right)^{m} \tag{5.45}$$

To start the iteration, values for $\dot{\gamma}^{0}_{\mathrm{B},n+1}$ and $\dot{\gamma}^{1}_{\mathrm{B},n+1}$ are needed. For the first time step, $\dot{\gamma}^{1}_{\mathrm{B},1}$ is taken to be close to zero while $\dot{\gamma}^{0}_{\mathrm{B},1} = 0$. For the remaining time steps, the initial guesses are $\dot{\gamma}^{0}_{\mathrm{B},n+1} = \dot{\gamma}_{\mathrm{B},n}$ and $\dot{\gamma}^{1}_{\mathrm{B},n+1} = \dot{\gamma}_0\left(\frac{\sigma^{0}_{\mathrm{vm,B,n+1}}}{\bar{\tau}^{0}_{n+1}}\right)^{m}$ [44]. Iterations are performed until the absolute value of the residual defined in Eq. 5.45 is less than a defined tolerance.

The evolution of the effective shear strength is solved fully implicitly with the backward Euler method as

$$\tau_{n+1}^{I+1} = \frac{\tau_n + h\dot{\gamma}_{\mathrm{B},n+1}^{I+1}\Delta t_{n+1}}{1 + \dfrac{h}{\tau_{\mathrm{ss}}}\dot{\gamma}_{\mathrm{B},n+1}^{I+1}\Delta t_{n+1}} \tag{5.46}$$

When the material routine has converged and the Cauchy stress tensor for the current time step has been obtained, the damage variable, δ_{n+1}, is calculated in accordance with Eq. 5.37. The stress tensor returned to Abaqus/Explicit at the end of the VUMAT has to be oriented in the reference configuration such that the FE solver can calculate the appropriate objective stress rate. The hyperelastic relations in the presented material model are calculated using the left Cauchy-Green deformation tensor, and the stress tensors are thus oriented in the current configuration. The irrotational Cauchy stress tensor returned to Abaqus at the end of the material routine is

$$\hat{\boldsymbol{\sigma}}_{n+1} = (\mathbf{R}_{n+1})^{\mathrm{T}}\boldsymbol{\sigma}_{\mathrm{eff},n+1}\mathbf{R}_{n+1}(1-\delta_{n+1}) \tag{5.47}$$

where $\mathbf{R}_{n+1}$ is the rotation tensor calculated as $\mathbf{R}_{n+1} = \mathbf{F}_{n+1}\mathbf{U}_{n+1}^{-1}$. The right stretch tensor at the current time step, $\mathbf{U}_{n+1}$, is provided by the Abaqus VUMAT interface.

As the time evolution of the inelastic deformation gradient in Eq. 5.40 is integrated with a first-order approximation, situations may arise where the strain increment provided by the Abaqus VUMAT interface, $\Delta\boldsymbol{\varepsilon}$, is too large for convergence to be achieved. A sub-stepping scheme is introduced to improve the robustness of the model for these cases. The number of sub-steps performed, N_{sub}, is determined by the following expression

$$N_{\mathrm{sub}} = \max\left\{\mathrm{nint}\left[\frac{\Delta\varepsilon_{\mathrm{eq}}}{\Delta\varepsilon_{\mathrm{cr}}}\right], 1\right\} \tag{5.48}$$

where $\mathrm{nint}[\cdot]$ is the nearest-integer function, $\Delta\varepsilon_{\mathrm{eq}}$ is the equivalent deviatoric strain increment calculated as $\Delta\varepsilon_{\mathrm{eq}} = \sqrt{\frac{2}{3}\Delta\boldsymbol{\varepsilon}' : \Delta\boldsymbol{\varepsilon}'}$, $\Delta\boldsymbol{\varepsilon}'$ is the deviatoric part of the strain increment tensor and $\Delta\varepsilon_{\mathrm{cr}}$ is a critical strain increment. The critical strain increment is calculated based on the initial shear strength and shear modulus of Part B as

$$\Delta\varepsilon_{\mathrm{cr}} = \chi\frac{\tau_0}{\mu_{\mathrm{B}}} \tag{5.49}$$

where χ is a numerical parameter that determines the magnitude of the critical strain increment. Unless otherwise stated, a value of 10^{-4} is used for χ for the remainder of this work.

During sub-stepping, the current total deformation gradient, $\mathbf{F}_{n+1}$, in the above expressions is replaced with the total deformation gradient evaluated at time $t_{n+\theta}$ defined as

$$\mathbf{F}_{n+\theta} = \theta \mathbf{F}_{n+1} + (1-\theta)\mathbf{F}_n \tag{5.50}$$

where

$$\theta = \frac{q}{N_{\text{sub}}} \quad \text{for} \quad q \in [0, N_{\text{sub}}] \tag{5.51}$$

Normal-distributed variables in accordance with Eq. 5.39 were generated with the Marsaglia polar method [45] and the left truncation was enforced by rejection sampling.

5.6 Summary

- A constitutive model consisting of a hyper-viscoelastic model together with a stochastic fracture initiation model was presented.
- The hyper-viscoelastic model is divided into two parts acting in parallel. Part A consists of a hyperelastic eight-chain spring, which describes the orientational strain hardening of the material. Part B consists of a hyperelastic neo-Hookean spring in series with a nonlinear viscous dashpot. Part B describes the initial elastic behaviour as well as the strain-rate- and pressure-dependent inelastic flow behaviour.
- The stochastic fracture initiation model is a modified version of the model presented by Holmström et al. [40]. The model utilises an assignment mesh to allocate a stochastic critical stress value to each element in the finite element mesh. When a defined equivalent stress reaches the critical stress in an element, the element is eroded according to the "crack band model" [41].
- The numerical implementation of the model closely follows the work of Johnsen et al. [43].

6 Constitutive model: Verification

The presented constitutive model is complex and it is not immediately obvious how the different components and material parameters interact. To get a better understanding of the effects of the different material parameters as well as the general behaviour of the model, verification simulations in Abaqus/Explicit at different stress states and strain rates have been carried out.

6.1 Simulation procedures

6.1.1 Single-element simulations

The first part of the model verification is performed by prescribing the deformation of single elements. A C3D8R element with dimensions $1 \times 1 \times 1$ mm^3 was used for all simulations. Appropriate boundary conditions were applied to achieve the desired stress states and the prescribed deformation was achieved by prescribing nodal velocities. Mass scaling was used to reduce the computational time of the simulations. The element used in the uniaxial tension simulations is shown as an example in Figure 6.1.

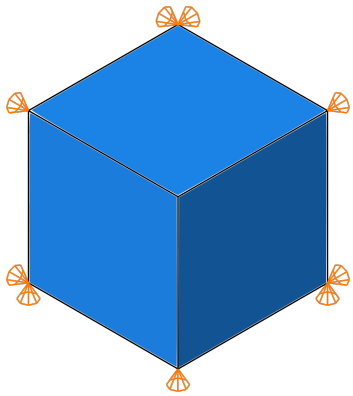

Figure 6.1: Finite element with boundary conditions corresponding to uniaxial tension and compression.

The stress states considered in the single-element simulations are: uniaxial tension, uniaxial compression, simple shear, hydrostatic tension and hydrostatic compression. The deformation state for each stress state as well as the corresponding deformation gradient are as follows.

Uniaxial tension/compression

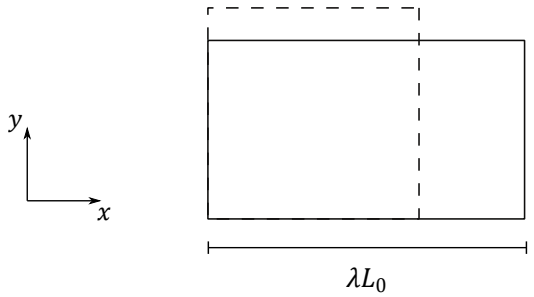

Figure 6.2: 2D sketch of an element experiencing uniaxial tension/compression.

A state of uniaxial stress is achieved by applying a displacement in the x-direction, while the element is allowed to contract elastically and inelastically in the y- and z-directions. This leads to the deformation gradient

$$\mathbf{F}_{\text{uniax.}} = \begin{bmatrix} \lambda & 0 & 0 \\ 0 & \lambda_{\text{t}} & 0 \\ 0 & 0 & \lambda_{\text{t}} \end{bmatrix} \tag{6.1}$$

where the transverse stretch ratio, λ_{t}, is expressed in terms of the inelastic stretch ratio, λ_{i}, as

$$\lambda_{\text{t}} = \lambda^{-\nu}(\lambda^{\text{i}})^{(\nu-0.5)} \tag{6.2}$$

If we assume small elastic deformations, i.e. $\lambda_{\text{i}} \approx \lambda$, the transverse stretch ratio becomes

$$\lambda_{\text{t}} \approx \frac{1}{\sqrt{\lambda}} \tag{6.3}$$

A value of $\lambda > 1$ gives uniaxial tension, while a value of $\lambda < 1$ gives uniaxial compression.

Simple shear

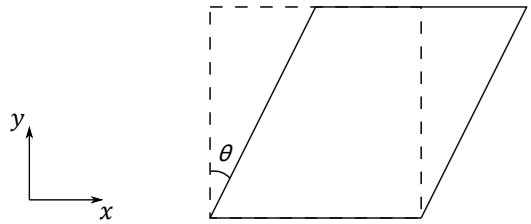

Figure 6.3: 2D sketch of an element experiencing simple shear.

A state of simple shear is achieved by displacing the top face in the x-direction while the element is prevented from contracting in the y- and z-directions – leading to no change in volume. The deformation gradient is thus

$$\mathbf{F}_{\text{shear}} = \begin{bmatrix} 1 & \gamma & 0 \\ 0 & 1 & 0 \\ 0 & 0 & 1 \end{bmatrix} \tag{6.4}$$

where $\gamma = \tan(\theta)$.

Hydrostatic tension/compression

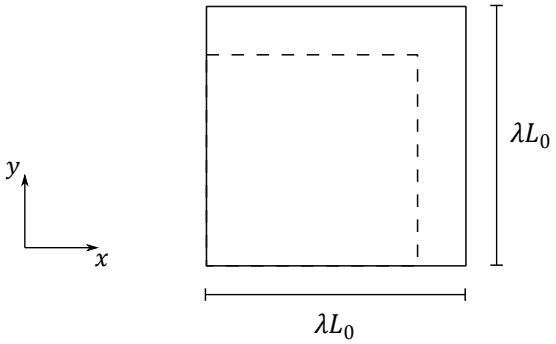

Figure 6.4: 2D sketch of an element experiencing uniaxial tension/compression.

A state of pure hydrostatic stress is achieved by applying the same displacement in all three directions. The resulting deformation gradient is then

$$\mathbf{F}_{\text{hydrostatic}} = \begin{bmatrix} \lambda & 0 & 0 \\ 0 & \lambda & 0 \\ 0 & 0 & \lambda \end{bmatrix} \tag{6.5}$$

A value of $\lambda > 1$ gives hydrostatic tension, while a value of $\lambda < 1$ gives hydrostatic compression.

6.1.2 Multi-element simulations

In addition to single-element simulations, simulations of cubes containing multiple elements were also performed as part of the material model verification. The multi-element models were primarily used to investigate the effects of the assignment mesh element size in the fracture initiation model. In addition, a multi-element simulation was performed to verify the model's stability for complex stress states. Boundary conditions were applied similarly to the single-element simulations. All multi-element analyses were mass-scaled and 10% of the analysis time was spent ramping up the prescribed nodal velocities. The FE-meshes considered are shown in Figure 6.5.

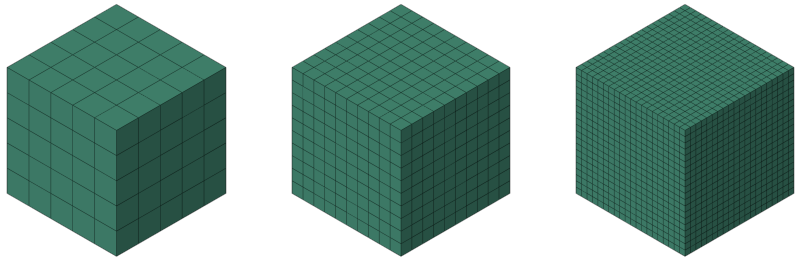

(a) **(b)** **(c)**

Figure 6.5: FE-models of $1 \times 1 \times 1$ mm^3 cubes used in the material model verification simulations discretised with element sizes of **(a)** 0.2 mm, **(b)** 0.1 mm and **(c)** 0.05 mm.

6.2 Behaviour of the hyper-viscoelastic model

The first part of the model verification consists of an overview of the model's behaviour for the stress states described above. The material parameters used in the verification simulations are found in Table 6.1 and were chosen to provide results similar to the experimental results.

Table 6.1: Material parameters used in the verification simulations.

Part A	μ_{A}	λ_{L}						
	[MPa]	[-]						
	5	1.2						
Part B	μ_{B}	κ	$\dot{\gamma}_0$	m	τ_0	τ_{ss}	h	α
	[MPa]	[MPa]	[s^{-1}]	[-]	[MPa]	[MPa]	[MPa]	[-]
	200	2000	10^{-3}	6	15	10	100	0.1

6.2.1 Uniaxial tension

Figure 6.6 shows the results from a uniaxial-tension simulation of a single element at a nominal strain rate of $10^{-3}\,\mathrm{s}^{-1}$. The results are shown in terms of Cauchy stress vs. logarithmic strain and effective inelastic strain rate vs. logarithmic strain. Figure 6.7 (a) shows how the Cauchy stress is further divided into contributions of Part A and Part B, while Figure 6.7 (b) shows how the total logarithmic strain is decomposed into elastic and inelastic parts. The logarithmic strain tensors on the current configuration are calculated from the left stretch tensors as

$$\boldsymbol{\varepsilon}_{\mathrm{B}}^{\mathrm{e}} = \ln\left(\mathbf{V}_{\mathrm{B}}^{\mathrm{e}}\right) \tag{6.6}$$

$$\boldsymbol{\varepsilon}_{\mathrm{B}}^{\mathrm{i}} = \ln\left(\mathbf{V}_{\mathrm{B}}\right) - \ln\left(\mathbf{V}_{\mathrm{B}}^{\mathrm{e}}\right) \tag{6.7}$$

where

$$\mathbf{V}_{\mathrm{B}}^{\mathrm{e}} = \sqrt{\mathbf{F}_{\mathrm{B}}^{\mathrm{e}}(\mathbf{F}_{\mathrm{B}}^{\mathrm{e}})^{\mathrm{T}}} \tag{6.8}$$

$$\mathbf{V}_{\mathrm{B}} = \sqrt{\mathbf{F}_{\mathrm{B}}(\mathbf{F}_{\mathrm{B}})^{\mathrm{T}}} \tag{6.9}$$

The definition of the logarithmic strain tensors ensures an additive decomposition of the total logarithmic strain tensor, $\boldsymbol{\varepsilon} = \ln\left(\mathbf{V}_{\mathrm{B}}\right)$, viz.

$$\boldsymbol{\varepsilon} = \boldsymbol{\varepsilon}_{\mathrm{B}}^{\mathrm{e}} + \boldsymbol{\varepsilon}_{\mathrm{B}}^{\mathrm{i}} \tag{6.10}$$

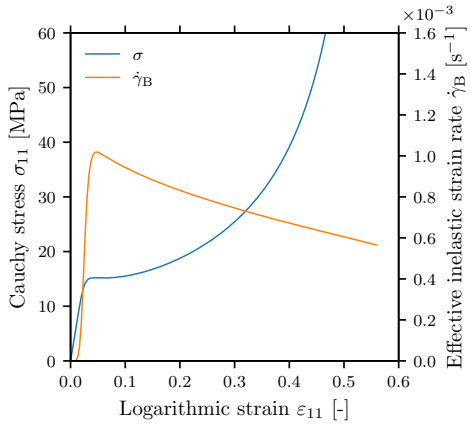

Figure 6.6: Cauchy stress and effective inelastic strain rate plotted against logarithmic strain from a uniaxial tension single element simulation at a nominal strain rate of $10^{-3}\,\mathrm{s}^{-1}$.

The initial stress-strain response is linear elastic. As the von Mises equivalent stress of Part B approaches the value of the effective shear strength, $\bar{\tau}$, the effective inelastic strain rate, $\dot{\gamma}_B$, increases rapidly and the total strain transitions from being pure elastic to being primarily inelastic. Figure 6.7 (a) shows how the onset of inelastic flow causes the stress from Part B to decrease. The reduction in the stress from Part B has two contributions, which can be seen when arranging Eq. 5.27

$$\sigma_{\mathrm{vm,B}} = \bar{\tau}\left(\frac{\dot{\gamma}_B}{\dot{\gamma}_0}\right)^{1/m} \tag{6.11}$$

The first contribution is the reduction of the effective shear strength from the combined effects of strain softening and pressure sensitivity. The second contribution comes from the relation between the effective inelastic strain rate and the kinematics of the problem. In uniaxial tension, the longitudinal part of the inelastic rate of deformation tensor is equal to the effective inelastic strain rate, according to Eq. 5.21 as

$$D^{\mathrm{i}}_{\mathrm{B},11} = \dot{\gamma}_B \tag{6.12}$$

During inelastic flow, the total rate of deformation tensor is approximately equal

to the inelastic rate of deformation tensor, i.e., $\mathbf{D}_{\mathrm{B}} \approx \mathbf{D}_{\mathrm{B}}^{\mathrm{i}}$. The longitudinal component of the total rate of deformation tensor for an element displaced with speed v and with current longitudinal length l is given as

$$D_{\mathrm{B},11} = \frac{\partial v_1}{\partial x_1} = \frac{v}{l} \tag{6.13}$$

which finally results in

$$\dot{\gamma}_{\mathrm{B}} \approx \frac{v}{l} \tag{6.14}$$

i.e, the effective inelastic strain rate is approximately equal to the logarithmic strain rate. As the speed, v, remains constant while the length of the element increases, the logarithmic strain rate, and consequently the effective inelastic strain rate, will decrease. Since the von Mises stress of Part B needs to satisfy Eq. 6.11, it will decrease proportionally to the effective shear strength and effective inelastic strain rate. This, in turn, will lead to a reduction of the deviatoric part of the stress from Part B, which is exactly what is observed in Figure 6.7 (a). The total stress from Part B, however, starts to increase again for large strains and follows a shape similar to the eight-chain spring of Part A. Figure 6.7 (c) shows that the increase in stress is caused by the hydrostatic Part B stress. This behaviour stems from the interaction between the transverse stresses of Part A and Part B.

The deviatoric and hydrostatic parts of the stress tensors during uniaxial tension are

$$\boldsymbol{\sigma}'_{\mathrm{A}} = \boldsymbol{\sigma}_{\mathrm{A}} = \begin{bmatrix} \sigma_{\mathrm{A}} & 0 & 0 \\ 0 & -\frac{\sigma_{\mathrm{A}}}{2} & 0 \\ 0 & 0 & -\frac{\sigma_{\mathrm{A}}}{2} \end{bmatrix} \tag{6.15}$$

$$\boldsymbol{\sigma}'_{\mathrm{B}} = \begin{bmatrix} \sigma'_{\mathrm{B}} & 0 & 0 \\ 0 & -\frac{\sigma'_{\mathrm{B}}}{2} & 0 \\ 0 & 0 & -\frac{\sigma'_{\mathrm{B}}}{2} \end{bmatrix} \tag{6.16}$$

$$\boldsymbol{\sigma}_{\mathrm{B,H}} = \begin{bmatrix} \sigma_{\mathrm{B,H}} & 0 & 0 \\ 0 & \sigma_{\mathrm{B,H}} & 0 \\ 0 & 0 & \sigma_{\mathrm{B,H}} \end{bmatrix} \tag{6.17}$$

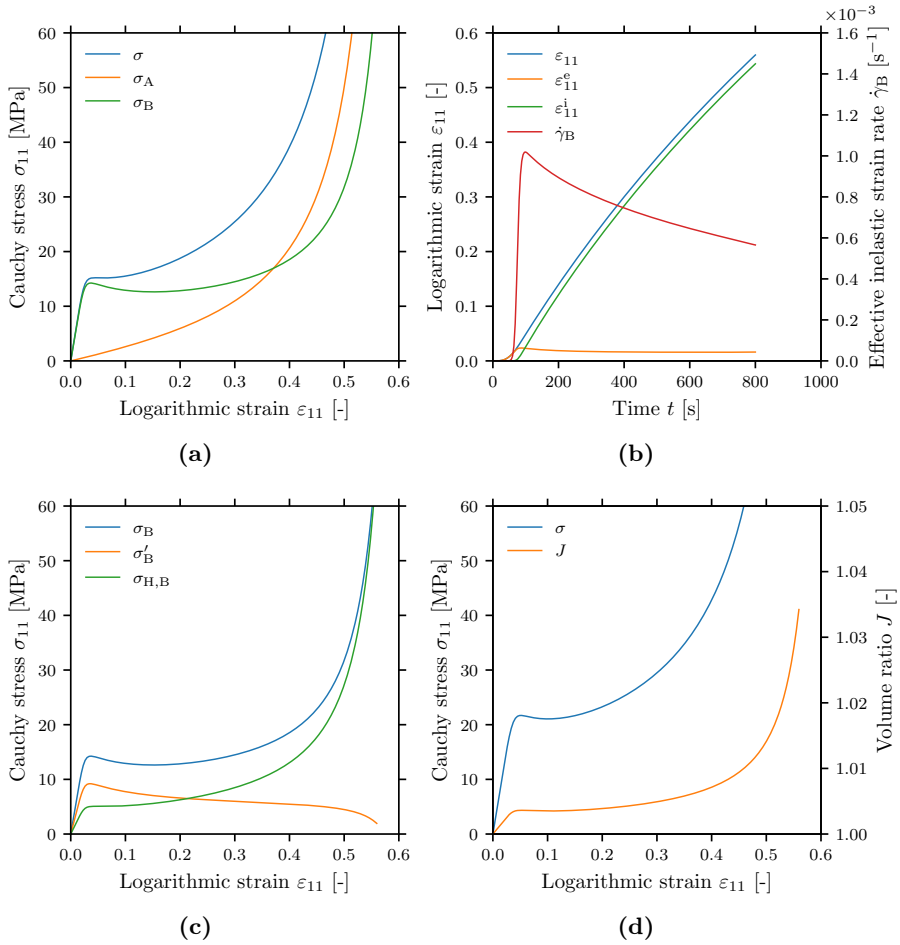

Figure 6.7: Results from a uniaxial tension single element simulation showing: **(a)** The decomposition of the total Cauchy stress in the loading direction into contributions from Part A and Part B, **(b)** the decomposition of the total logarithmic strain component in the loading direction into elastic and inelastic parts vs. time and the effective inelastic strain rate, **(c)** the decomposition of the Part B Cauchy stress in the loading direction into deviatoric and hydrostatic parts, **(d)** the total Cauchy stress in the loading direction and the volume ratio plotted against the longitudinal logarithmic strain.

To satisfy the boundary conditions of no transverse stresses, the following expression must hold

$$-\frac{\sigma_{\mathrm{A}}}{2} - \frac{\sigma'_{\mathrm{B}}}{2} + \sigma_{\mathrm{B,H}} = 0 \tag{6.18}$$

which reveals that the hydrostatic stress of Part B is proportional to the stress of Part A. Consequently, the volume ratio, J, will be subject to the same proportionality, as can be seen when inserting the expression for the hydrostatic stress of Part B into the equation above

$$J = 1 + \frac{1}{2\kappa}(\sigma_{\mathrm{A}} + \sigma'_{\mathrm{B}}) \tag{6.19}$$

which is observed in Figure 6.7 (d).

Figure 6.8 shows the results from uniaxial tension single element simulations at different nominal strain rates, $\dot{e}$. The strain rate sensitivity of the constitutive model is clearly seen in the flow stress, which increases with the strain rate. As the evolution of the strain-softening is dependent on the effective inelastic strain rate in accordance with Eq. 5.29, the magnitude of the strain-softening increases with the strain rate. It is worth noting that the stress-strain curves for the different strain rates converge when the strain approaches the locking strain.

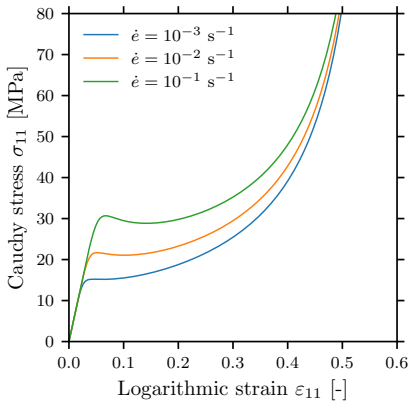

Figure 6.8: Cauchy stress vs. logarithmic strain curves from single element uniaxial tension simulations at different nominal strain rates.

6.2.2 Uniaxial compression

The analysis from the previous section is now repeated for an element subjected to uniaxial compression with a nominal strain rate of $10^{-3}\,\mathrm{s}^{-1}$. Figure 6.9 compares the stress-strain curves for uniaxial tension and uniaxial compression. The curves differ in two ways. Firstly, the yield stress is higher in compression than in tension because of the pressure sensitivity of the model. Secondly, the strain hardening is more rapid in tension than in compression. The difference in the hardening rate comes from the fact that the magnitude of the logarithmic strain required to reach the locking stretch, λ_{L}, is lower in tension than in compression. This result will now be analysed.

If the elastic compressibility of the material is neglected, the deformation gradient for an element subjected to uniaxial tension or uniaxial compression is as follows

$$\mathbf{F} = \begin{bmatrix} \lambda & 0 & 0 \\ 0 & \dfrac{1}{\sqrt{\lambda}} & 0 \\ 0 & 0 & \dfrac{1}{\sqrt{\lambda}} \end{bmatrix} \tag{6.20}$$

which gives an effective chain stretch of

$$\bar{\lambda}_{\mathrm{c}} = \sqrt{\frac{\lambda^2 + \dfrac{2}{\lambda}}{3}} \tag{6.21}$$

The stretch ratios that satisfy the equation $\bar{\lambda}_{\mathrm{c}} = \lambda_{\mathrm{L}} = 1.2$ are then found numerically with the Newton-Raphson scheme. For tension, i.e. $\lambda > 1$, the stretch ratio at locking is $\lambda = 1.79$ which is equivalent to a logarithmic strain magnitude of

$$|\varepsilon_{11}| = |\ln \lambda| = 0.58 \tag{6.22}$$

For compression, i.e. $\lambda < 1$, the stretch ratio at locking is $\lambda = 0.49$ which is equivalent to a logarithmic strain of

$$|\varepsilon_{11}| = |\ln \lambda| = 0.71 \tag{6.23}$$

Thus, the material "locks" quicker in tension than in compression as observed in Figure 6.9.

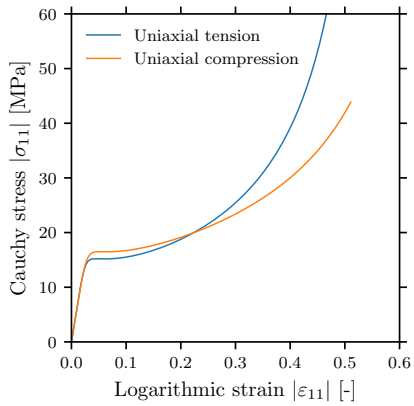

Figure 6.9: Comparison between the results from a uniaxial tension simulation and uniaxial compression simulation of a single element in terms of absolute Cauchy stress vs. absolute logarithmic strain curves.

The stress vs. strain curve from the compression simulation is plotted together with effective inelastic strain rate vs. strain in Figure 6.10. The effective inelastic strain rate is seen to increase with applied strain, which is the opposite of what is observed in uniaxial tension. However, the reason for this behaviour is still the same as for uniaxial tension. As the element is compressed, the length of the element in the loading direction is reduced, which causes the logarithmic strain to increase. According to Eq. 6.14, the effective inelastic strain rate will then also increase.

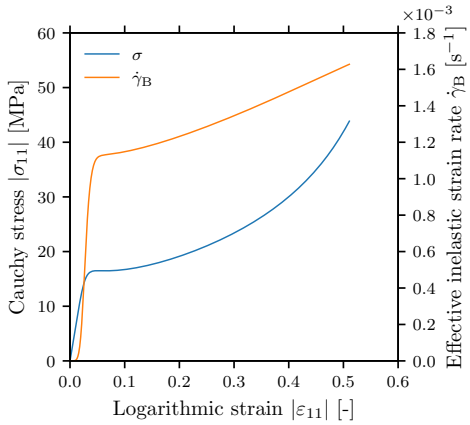

Figure 6.10: Cauchy stress and effective inelastic strain rate plotted against logarithmic strain from a uniaxial compression single element simulation at a nominal strain rate of $10^{-3}\,s^{-1}$.

More results from the uniaxial compression simulation are shown in Figure 6.11 in terms of the same type of plots as presented for the tension simulations. The observed trends follow those observed for the uniaxial tension simulation with the exception of the deviatoric part of the Part B stress. The increasing effective inelastic strain rate during compression counteracts the strain-softening of the viscous dashpot, which results in a flatter stress vs. strain curve for the Part B deviatoric stress.

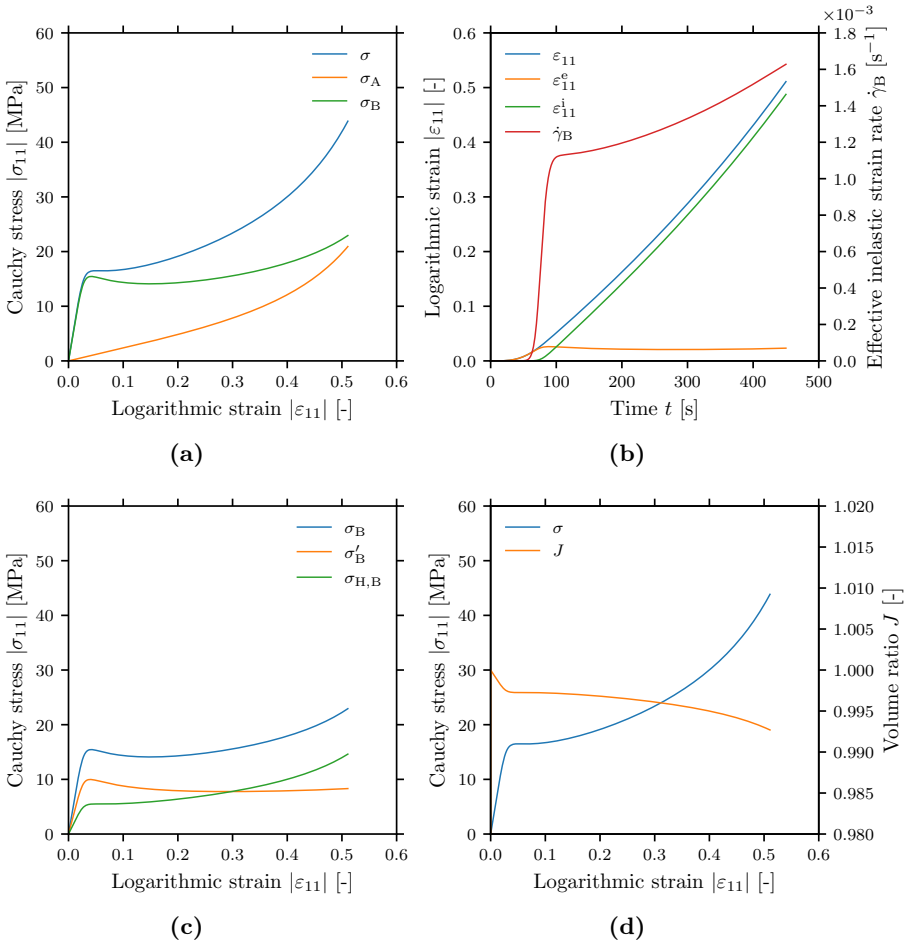

Figure 6.11: Results from a uniaxial compression single element simulation showing: **(a)** The decomposition of the total Cauchy stress in the loading direction into contributions from Part A and Part B, **(b)** the decomposition of the total logarithmic strain component in the loading direction into elastic and inelastic parts vs. time and the effective inelastic strain rate, **(c)** the decomposition of the Part B Cauchy stress in the loading direction into deviatoric and hydrostatic parts, **(d)** the total Cauchy stress in the loading direction and the volume ratio plotted against the longitudinal logarithmic strain.

6.2.3 Simple shear

Results from the simulation of a single element subjected to a simple shear deformation are shown in Figures 6.12, 6.13 and 6.14. The top face of the element is given a velocity of $2 \cdot 10^{-3}$ mm/s, which results in a nominal tensorial shear strain rate of $10^{-3}\,\mathrm{s}^{-1}$. Unlike for the uniaxial stress states, the effective inelastic strain rate remains approximately constant throughout the analysis for the case of simple shear deformation. Otherwise, the general behaviour is similar.

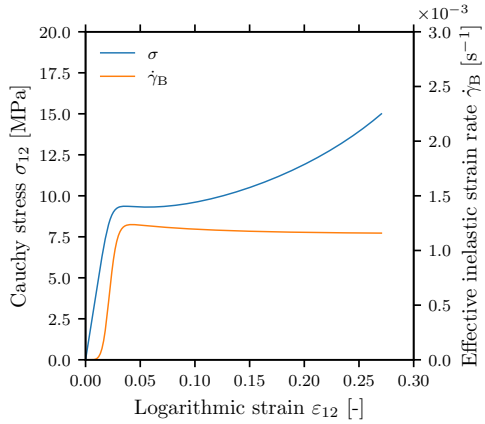

Figure 6.12: Cauchy stress and effective inelastic strain rate plotted against logarithmic strain from a simple shear single element simulation.

Figure 6.13 shows the components of the Cauchy stress tensor and the total logarithmic strain tensor. The graphs illustrate how the simple shear deformation mode results in a pure shear stress state and pure shear strains only for small strains. For large strains, non-linear geometric effects cause the diagonal terms of the stress and strain tensors to become non-zero. This can be shown by analysing the deformation gradient in Eq. 6.4. The left Cauchy-Green deformation tensor for simple shear is

$$\mathbf{B} = \begin{bmatrix} 1+\gamma^2 & \gamma & 0 \\ \gamma & 1 & 0 \\ 0 & 0 & 1 \end{bmatrix} \tag{6.24}$$

and the deviatoric part is

$$\mathbf{B}' = \begin{bmatrix} 2/3\gamma^2 & \gamma & 0 \\ \gamma & -1/3\gamma^2 & 0 \\ 0 & 0 & -1/3\gamma^2 \end{bmatrix} \tag{6.25}$$

If we neglect the elastic-inelastic split of the deformation gradient and assume the Cauchy stress tensor is expressed on the form

$$\boldsymbol{\sigma} = \mu \mathbf{B}' \tag{6.26}$$

the stress tensor for simple shear is

$$\boldsymbol{\sigma} = \mu \begin{bmatrix} 2/3\gamma^2 & \gamma & 0 \\ \gamma & -1/3\gamma^2 & 0 \\ 0 & 0 & -1/3\gamma^2 \end{bmatrix} \tag{6.27}$$

The result $\sigma_{11} = -2\sigma_{22} = -2\sigma_{33}$ from the above equation is seen in Figure 6.13 (a) in the elastic region of approx. $\varepsilon_{12} < 0.03$. When the inelastic flow starts, there is a slight redistribution of the diagonal elements of the Cauchy stress tensor, but Eq. 6.27 is still approximately satisfied. Note that for small deformations, the Cauchy stress tensor is reduced to only contain shear stresses, which is in line with linear elasticity theory, viz.

$$\boldsymbol{\sigma} = \mu \begin{bmatrix} 0 & \gamma & 0 \\ \gamma & 0 & 0 \\ 0 & 0 & 0 \end{bmatrix} \quad \text{for} \quad \gamma \ll 1 \tag{6.28}$$

The total logarithmic strain tensor is calculated as

$$\boldsymbol{\varepsilon} = \frac{1}{2} \ln(\mathbf{B}) \tag{6.29}$$

This calculation is tricky to perform algebraically, but it can be done easily numerically. If we take $\gamma = 0.5$, the resulting logarithmic strain tensor is

$$\boldsymbol{\varepsilon} = \begin{bmatrix} 0.06 & 0.24 & 0 \\ 0.24 & -0.06 & 0 \\ 0 & 0 & 0 \end{bmatrix} \tag{6.30}$$

i.e., $\varepsilon_{11} = -\varepsilon_{22}$ and $\varepsilon_{33} = 0$. This result is seen in Figure 6.13 (b). Similar to

the Cauchy stress tensor, the logarithmic strain tensor is reduced to contain only shear strains for small deformations, viz.

$$\boldsymbol{\varepsilon} = \begin{bmatrix} 0 & \gamma/2 & 0 \\ \gamma/2 & 0 & 0 \\ 0 & 0 & 0 \end{bmatrix} \quad \text{for} \quad \gamma \ll 1 \tag{6.31}$$

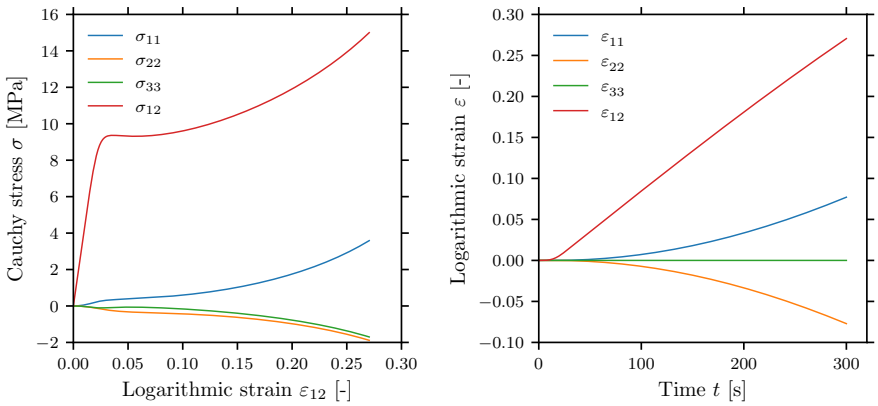

(a) **(b)**

Figure 6.13: Results from a simple shear single element simulation showing: **(a)** The components of the Cauchy stress tensors vs. logarithmic shear strain and **(b)** the components of the logarithmic strain tensor vs. time.

For the sake of completeness, additional results are presented in Figure 6.14 as for the previous two stress states. The main difference between the simple shear simulation and the uniaxial stress simulation is that there is no hydrostatic stress in simple shear due to the geometrically imposed constant volume.

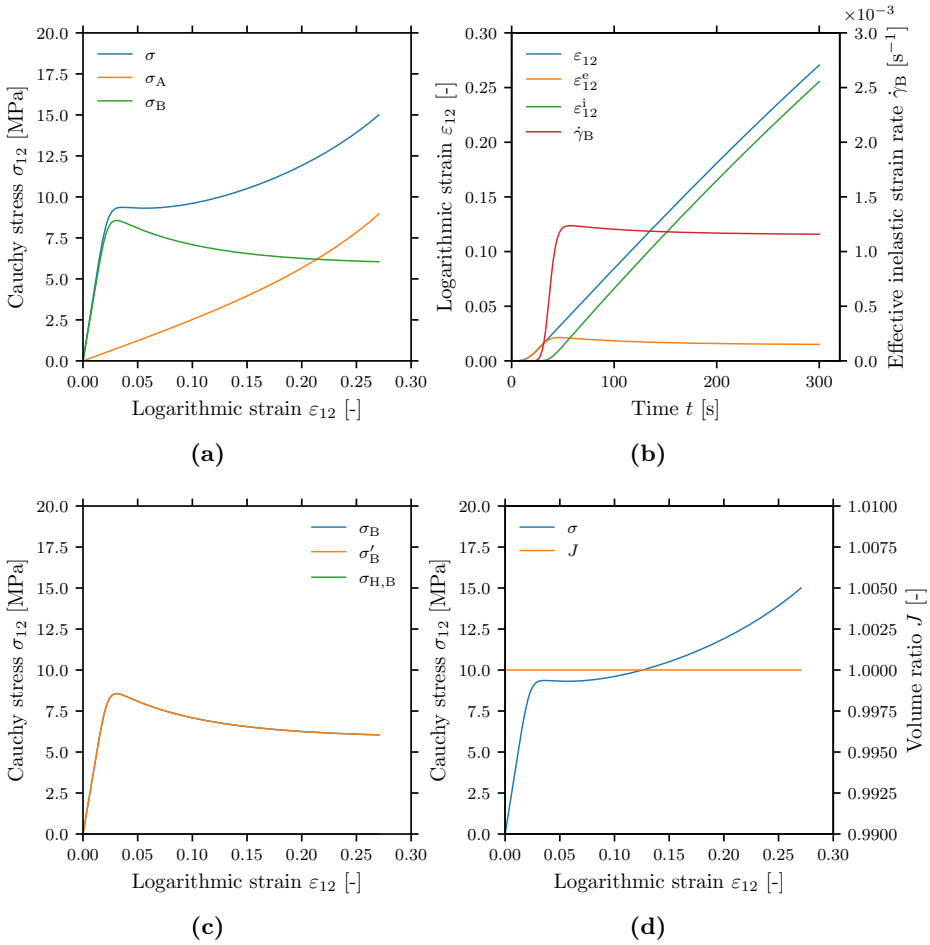

Figure 6.14: Results from a simple shear single element simulation showing: **(a)** The decomposition of the total Cauchy stress in the loading direction into contributions from Part A and Part B, **(b)** the decomposition of the total logarithmic strain component in the loading direction into elastic and inelastic parts vs. time and the effective inelastic strain rate, **(c)** the decomposition of the Part B Cauchy stress in the loading direction into deviatoric and hydrostatic parts, **(d)** the total Cauchy stress in the loading direction and the volume ratio plotted against the logarithmic shear strain.

6.2.4 Hydrostatic tension and compression

Figure 6.15 shows the results from the hydrostatic tension and compression simulations. As deviatoric stresses drive the inelastic flow of the material model, no inelastic flow occurs during a pure hydrostatic stress state. The stress-strain response, in this case, is governed entirely by the hydrostatic stress of Part B, i.e.,

$$\boldsymbol{\sigma} = \kappa(J-1)\mathbf{I} \tag{6.32}$$

The slight nonlinearity in the hydrostatic stress vs. volumetric strain response is a result of plotting the logarithmic volumetric strain while the constitutive relation is formulated in terms of the volume ratio, J.

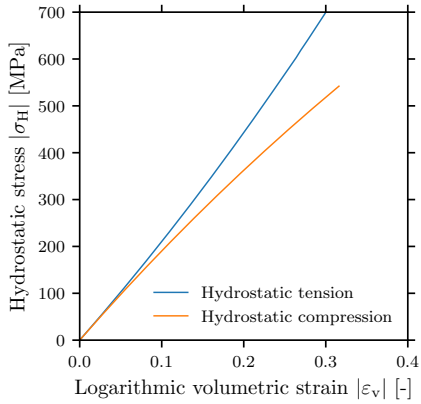

Figure 6.15: Absolute hydrostatic Cauchy stress vs. absolute logarithmic volumetric strain curves from single element simulations of hydrostatic tension and compression.

6.2.5 Multi-element torsion-tension simulation

To test the robustness of the implementation of the constitutive model, analyses with more than one element should be performed. In the single-element simulations studied so far, the nodal displacements have been prescribed, which may suppress any potential bugs in the VUMAT that could manifest if the nodes were free to move. To check if this is the case, the multi-element cube with an element size 0.1 mm shown in Chapter 6.1.2 was subjected to a combined tension and torsion deformation. The deformation was achieved by fixing the bottom-face nodes

and prescribing the motion of the top-face nodes with an MPC beam constraint connected to a master node which was given a velocity of 0.01 mm/s in the vertical direction and an angular velocity of $3.14 \cdot 10^{-2}$ rad/s about the vertical axis. The simulation time was 50 s. The deformed shape of the model throughout the analysis is shown in Figure 6.16. Force vs. displacement and torque vs. rotation curves are shown in Figure 6.17. No instabilities are observed in either the deformed shapes or in the response curves, which indicates that the implementation of the model is robust enough for use in multi-element simulations with complex stress states.

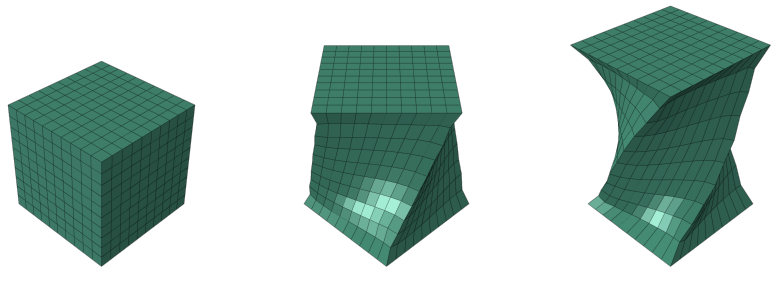

(a) **(b)** **(c)**

Figure 6.16: The tension-torsion FE mesh at simulation time **(a)** 0 s, **(b)** 25 s and **(c)** 50 s.

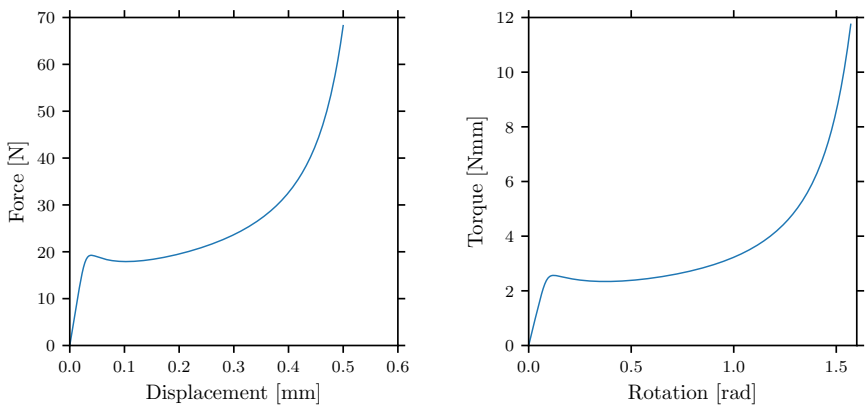

(a) **(b)**

Figure 6.17: Response curves from the torsion-tension simulation showing **(a)** force vs. displacement and **(b)** torque vs. rotation.

6.2.6 Parametric study

With the general behaviour of the constitutive model thoroughly investigated, attention is now turned towards the effects of the different material parameters on the stress-strain response. Single-element simulations were carried out where one material parameter was varied while the other parameters were assigned the values in Table 6.1. The results from the single-element simulations studying the effects of the hyper-viscoelastic material parameters are shown in Figure 6.18, 6.19, 6.20 and 6.21. The main findings are summarised as:

- **The shear modulus of Part A,** μ_{A}, determines the slope of the Part A stress. The effect is most noticeable during inelastic flow when the stress from Part B is no longer increasing.
- **The locking stretch,** λ_{L}, determines the vertical asymptote of the stress-strain curve. It also has a slight effect on the slope of the Part A stress, in accordance with Eq. 5.13.
- **The shear modulus of Part B,** μ_{B}, determines the slope of the initial elastic region of the stress-strain curve.
- **The initial shear strength**, τ_0, determines the flow stress of the material. When the saturated shear strength remains unchanged, the stress-strain curves for the different values of τ_0 converge rather quickly after the inelastic flow occurs.
- **The saturated shear strength**, τ_{ss}, determines the drop in stress after yield due to strain softening.
- **The softening modulus**, h, determines the rate of the strain softening.
- **The strain-rate sensitivity parameter**, m, determines both the strain-rate sensitivity of the flow stress as well as the shape of the stress-strain curve in the transition from pure elasticity to inelastic flow. The last point is seen clearly in Figure 6.20 (b).
- **The pressure sensitivity parameter**, α, determines the difference in flow stress between uniaxial tension and uniaxial compression. Unlike most pressure-sensitive plasticity models, the pressure sensitivity parameter in the implemented model affects the flow stress in tension.

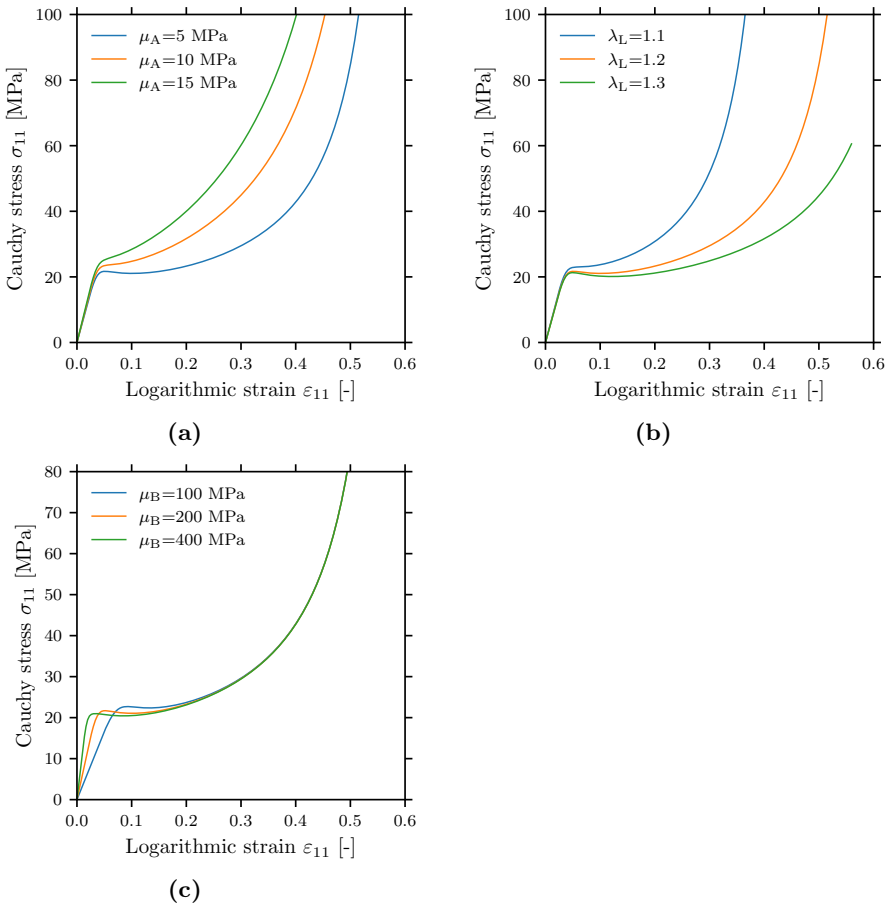

Figure 6.18: Stress vs. strain curves from uniaxial tension single element simulations at a nominal strain rate of $10^{-2}\,\mathrm{s}^{-1}$. The effects of μ_A, λ_L and μ_B on the stress-strain response are shown in **(a)**, **(b)** and **(c)** respectively.

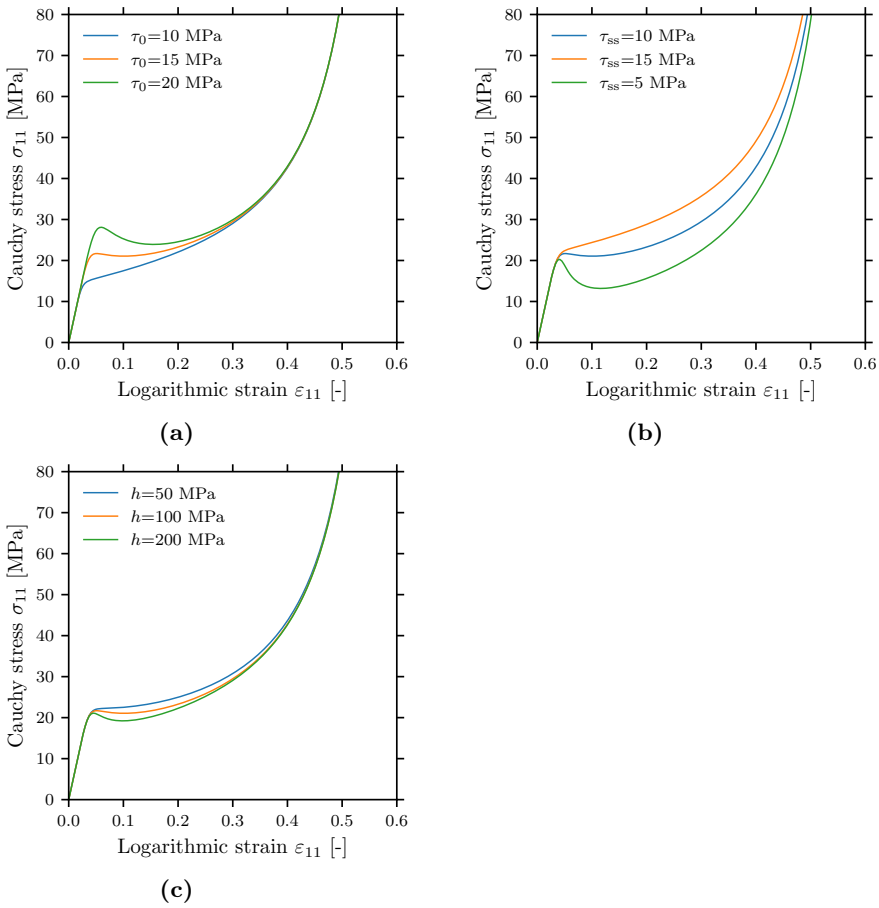

Figure 6.19: Stress vs. strain curves from uniaxial tension single element simulations at a nominal strain rate of $10^{-2}\,\mathrm{s}^{-1}$. The effects of τ_0, τ_{ss} and h on the stress-strain response are shown in **(a)**, **(b)** and **(c)** respectively.

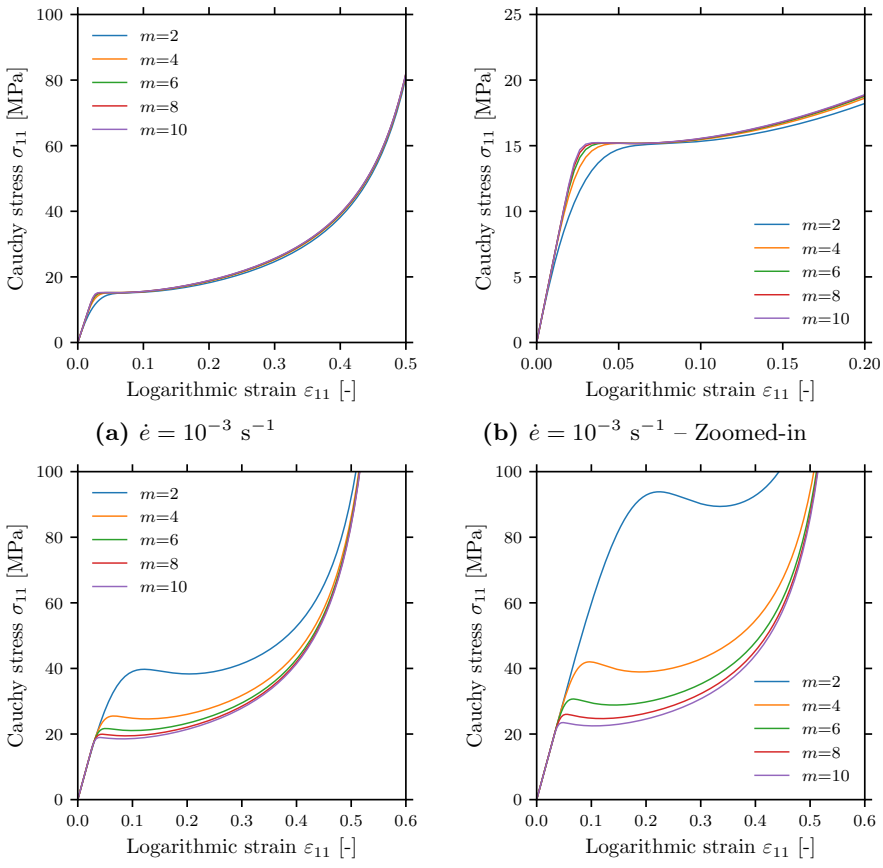

(a) $\dot{e} = 10^{-3}$ s^{-1} **(b)** $\dot{e} = 10^{-3}$ s^{-1} – Zoomed-in

(c) $\dot{e} = 10^{-2}$ s^{-1} **(d)** $\dot{e} = 10^{-1}$ s^{-1}

Figure 6.20: Stress vs. strain curves from uniaxial tension single element simulations showing how the parameter m affects the stress-strain response at different nominal strain rates.

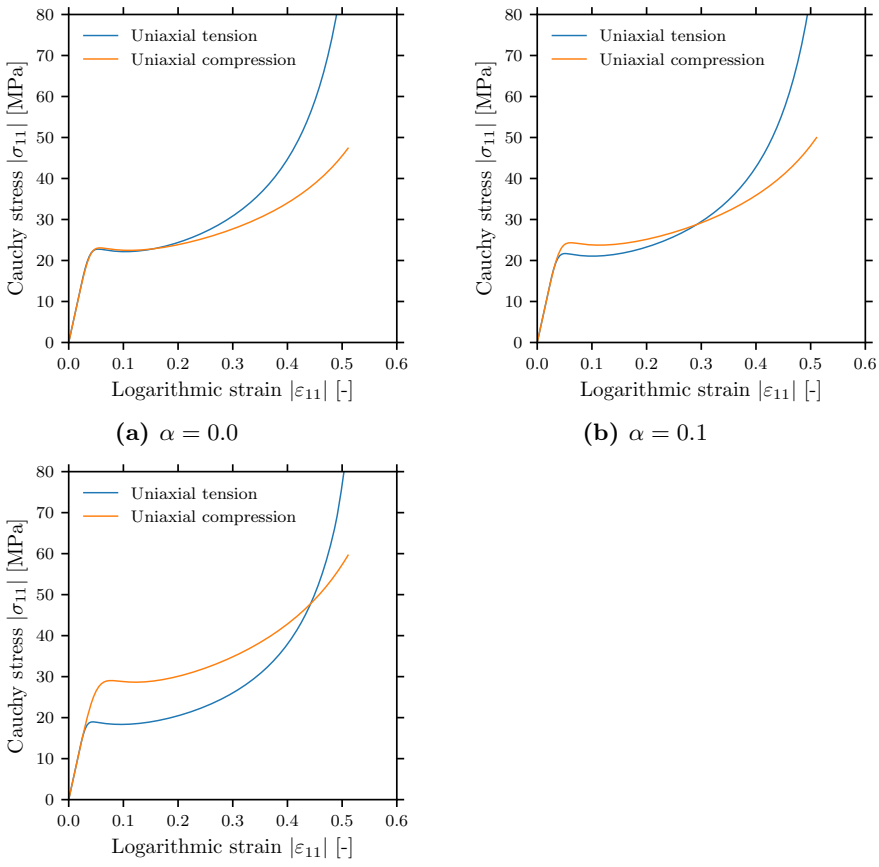

(a) $\alpha = 0.0$

(b) $\alpha = 0.1$

(c) $\alpha = 0.4$

Figure 6.21: Stress vs. strain curves comparing uniaxial tension and uniaxial compression single element simulations for different values of the parameter α. All analyses were performed with a nominal strain rate of $10^{-2}\,\mathrm{s}^{-1}$.

6.3 Behaviour of the fracture initiation model

The second part of the verification of the constitutive model concerns the fracture initiation part of the model. A similar investigation as for the hyper-viscoelastic part is conducted.

6.3.1 Fracture energy release

Figure 6.22 shows how the softening stage of the fracture is affected by the energy release parameter, G_f, and the finite element size, h_el. The results were obtained from uniaxial tension single-element simulations using the hyper-viscoelastic parameters from before. A constant critical stress of 40 MPa was used for all these simulations.

Figure 6.22 (a) shows the results from simulations with constant element size and varying values of G_f. A reduction of the slope of the stress-strain curve in the softening stage, and conversely an increase in dissipated fracture energy, is observed as G_f is increased. The sharp drop in stress level near the end of the softening stage, seen most clearly for $G_\mathrm{f} = 2.00\,\mathrm{N/mm}$, is due to the erosion of the element as the damage parameter, δ, reaches the critical value of 0.9. An interesting result is obtained for $G_\mathrm{f} = 5.00\,\mathrm{N/mm}$, where the stress increases after reaching the critical stress value. Evidently, there exists a value for G_f which causes the softening to be unable to keep up with the strain-hardening of the eight-chain model.

Figure 6.22 (b) shows the results from simulations with a constant of G_f but varying element sizes. As expected from the model, the specific fracture energy, i.e., the area under the stress-strain curve in the softening stage, increases as the element size is reduced.

For uniaxial tension, a criterion for the value of G_f to ensure stress-softening can be derived as follows. Let σ and ε be the axial Cauchy stress and axial logarithmic strain, respectively. Stress-softening requires that

$$\frac{\mathrm{d}\sigma}{\mathrm{d}\varepsilon} < 0 \tag{6.33}$$

Inserting the relation between the Cauchy stress and the effective Cauchy stress from Eq. 5.36 into the above equation gives

$$\frac{\mathrm{d}\sigma}{\mathrm{d}\varepsilon} = \frac{\mathrm{d}\sigma_\mathrm{eff}}{\mathrm{d}\varepsilon}(1-\delta) - \sigma_\mathrm{eff}\frac{\mathrm{d}\delta}{\mathrm{d}\varepsilon} < 0 \tag{6.34}$$

where

$$\frac{\mathrm{d}\delta}{\mathrm{d}\varepsilon} = \frac{1}{\bar{\varepsilon}_\mathrm{u} - \bar{\varepsilon}_\mathrm{c}} \tag{6.35}$$

in accordance with Eq. 5.37. Inserting Eq. 5.35 and Eq. 6.35 into Eq. 6.34 and evaluating the last equation for $\delta = 0,\ \sigma_\mathrm{eff} = \bar{\sigma}_\mathrm{c}$ gives

$$\left.\frac{\mathrm{d}\sigma}{\mathrm{d}\varepsilon}\right|_{\delta=0,\ \sigma_\mathrm{eff}=\bar{\sigma}_\mathrm{c}} = \frac{1}{\bar{\varepsilon}_\mathrm{u} - \bar{\varepsilon}_\mathrm{c}} \left[\frac{\mathrm{d}\sigma_\mathrm{eff}}{\mathrm{d}\varepsilon}\frac{2G_\mathrm{f}}{\bar{\sigma}_\mathrm{c} h_\mathrm{el}} - \bar{\sigma}_\mathrm{c}\right] < 0 \tag{6.36}$$

which when solved for G_f results in

$$G_\mathrm{f} < \frac{\bar{\sigma}_\mathrm{c}^2 h_\mathrm{el}}{2}\left(\frac{\mathrm{d}\sigma_\mathrm{eff}}{\mathrm{d}\varepsilon}\right)^{-1} \tag{6.37}$$

The above result shows that the slope of the effective stress-strain curve constrains the magnitude of G_f required to achieve the desired stress-softening behaviour. As the critical value of G_f is also affected by the element size and the value of the critical stress, a small value should be assigned to G_f to ensure softening after the critical stress is reached.

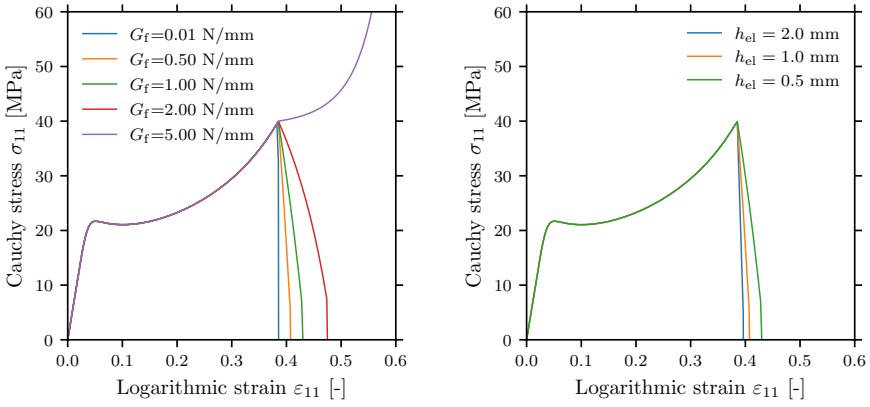

(a) $h_\mathrm{el} = 1$ mm **(b)** $G_\mathrm{f} = 0.5$ N/mm

Figure 6.22: Stress vs. strain curves from uniaxial tension single-element simulations for **(a)** different values of G_f but constant element size and **(b)** varying element size and constant G_f.

6.3.2 Critical stress

Figure 6.23 shows how the value of the critical stress, $\bar{\sigma}_c$, affects the stress-strain response in uniaxial tension, simple shear and hydrostatic tension. A deterministic critical stress is achieved by setting $\bar{\sigma}_{c,std} = 0\,\text{MPa}$ and $\bar{\sigma}_{c,mean} = \bar{\sigma}_c$ in the material input card. All simulations were run with a G_f of $0.5\,\text{N/mm}$. As expected, the critical stress determines the stress level at which fracture occurs. For uniaxial tension and simple shear, the stress decreases linearly after the critical stress is reached until $\delta = 0.9$. The rate of the softening changes with the value of the critical stress such that the dissipated energy remains constant.

In hydrostatic tension, the softening behaviour appears a bit odd. For $\bar{\sigma}_c = 40\,\text{MPa}$ and $\bar{\sigma}_c = 50\,\text{MPa}$, the slope of the stress-strain curves decreases immediately after the critical stress is reached, but not enough to cause the desired softening behaviour. For $\bar{\sigma}_c = 80\,\text{MPa}$, on the other hand, the stress level is reduced immediately after fracture, but not as rapidly and linearly as in the cases of uniaxial tension and simple shear. The peculiar behaviour in hydrostatic tension can be explained by the equations of the fracture model. Let the stress and strain components in the different coordinate directions be denoted σ and ε respectively. By assuming small strains, the stress tensor is given by the material model as

$$\boldsymbol{\sigma} = 3\kappa\varepsilon\mathbf{I} \tag{6.38}$$

which gives an equivalent stress of

$$\bar{\sigma} = \sqrt{3}\sigma \tag{6.39}$$

and an equivalent strain of

$$\bar{\varepsilon} = \sqrt{3}\varepsilon \tag{6.40}$$

Inserting the above equations into Eq. 6.34 and doing the appropriate calculations result in the following inequality which must be satisfied to ensure softening after the critical stress is reached in hydrostatic tension

$$\left.\frac{\mathrm{d}\sigma}{\mathrm{d}\varepsilon}\right|_{\delta=0,\ \sigma_{\text{eff}}=\bar{\sigma}_c} = 3\kappa - \frac{\bar{\sigma}_c^2 h_{\text{el}}}{2G_f} < 0 \tag{6.41}$$

Solving for $\bar{\sigma}_c$ gives

$$\bar{\sigma}_\mathrm{c} > \sqrt{\frac{6\kappa G_\mathrm{f}}{h_\mathrm{el}}} \tag{6.42}$$

If we insert $G_\mathrm{f} = 0.5\,\mathrm{N/mm}$, $\kappa = 2000\,\mathrm{MPa}$ and $h_\mathrm{el} = 1\,\mathrm{mm}^3$ into the inequality above, we get the condition $\bar{\sigma}_\mathrm{c} > 77.45\,\mathrm{MPa}$ which explains why only the simulation performed with $\bar{\sigma}_\mathrm{c} = 80\,\mathrm{MPa}$ produces stress softening immediately after fracture.

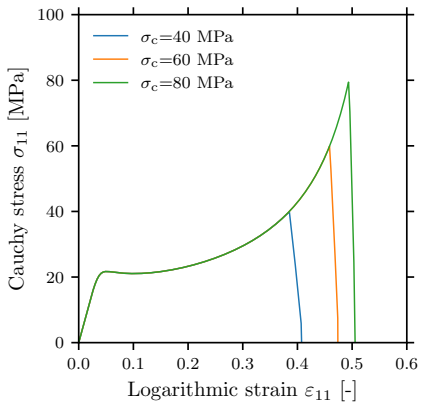

(a) Uniaxial tension

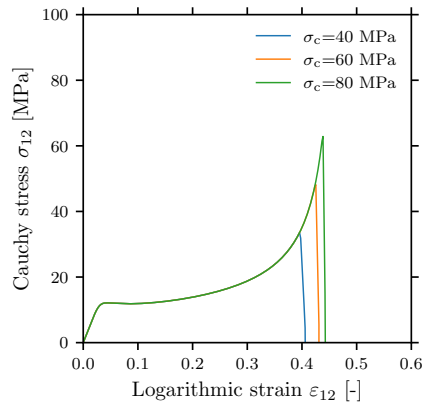

(b) Simple shear

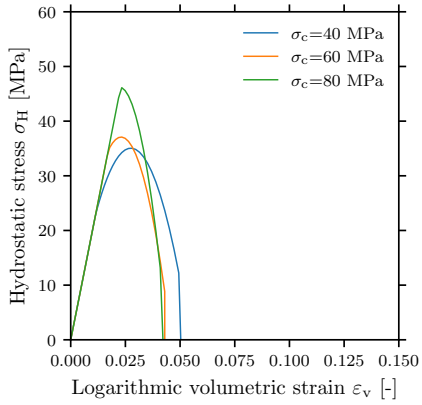

(c) Hydrostatic tension

Figure 6.23: Stress vs. strain curves from single-element simulations with varying values for the critical stress, $\bar{\sigma}_\mathrm{c}$ for **(a)** uniaxial tension, **(b)** simple shear and **(c)** hydrostatic tension.

6.3.3 Assignment mesh

The last part of the fracture model verification concerns the assignment mesh. As Holmström [46] already performed a thorough investigation of the assignment mesh in his PhD thesis, this section is kept brief.

Table 6.2: Fracture parameters used in multi-element verification simulations.

$\bar{\sigma}_{\mathrm{c,mean}}$ [MPa]	$\bar{\sigma}_{\mathrm{c,std}}$ [MPa]	$\bar{\sigma}_{\mathrm{c,min}}$ [MPa]	G_{f} [N/mm]
100	20	40	0.5

The interrelation between the assignment mesh element size, $h_{\bar{\sigma}_{\mathrm{c}}}$, and the FE mesh element size, h_{el}, is demonstrated in Figure 6.24 and Figure 6.25 for multi-element cube models. Figure 6.24 shows how the distribution of the critical stresses remains unchanged when the assignment mesh is kept constant and the FE mesh is refined. Figure 6.25 shows how the element size of the assignment mesh alters the physical length scale of the critical stress distribution when the FE mesh is kept constant and the assignment mesh is refined. The fracture parameters used in the simulations are shown in Table 6.2.

The effect of the element sizes of the FE mesh and assignment mesh is further studied by simulating the models shown in Figures 6.24 and 6.25 in uniaxial tension. The results from repeat simulations with different realisations of the distribution of the critical stress are shown in Figure 6.26 in terms of the net fracture stress defined as $F_{\max}/A$ where $F_{\max}$ is the force at failure and A is the cross-sectional area of the model. As can be seen from the results, the stochastic critical stress produces a scatter in the net fracture stress in repeat simulations. Figure 6.26 (a) shows that the mean net fracture stress is reduced when $h_{\bar{\sigma}_{\mathrm{c}}}$ is kept constant and h_{el} is reduced, while Figure 6.26 (b) shows that the scatter in the net fracture stress increases when h_{el} is kept constant and $h_{\bar{\sigma}_{\mathrm{c}}}$ is increased.

The results from the simulations presented here are not conclusive enough to give any recommendations for an optimal ratio between the element sizes of the FE mesh and the assignment mesh but show that the size of the assignment mesh elements can affect both the mean fracture stress and the scatter of the fracture stress. In a sense, $h_{\bar{\sigma}_{\mathrm{c}}}$ can be treated as a parameter of the fracture initiation model to be determined from calibration to help achieve experimentally observed results.

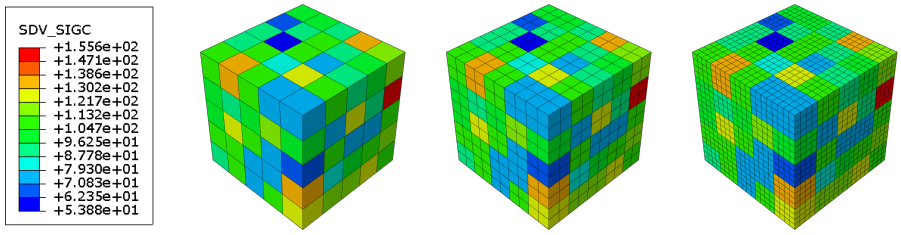

Figure 6.24: Distributed critical stress in models with a constant assignment mesh and varying FE mesh.

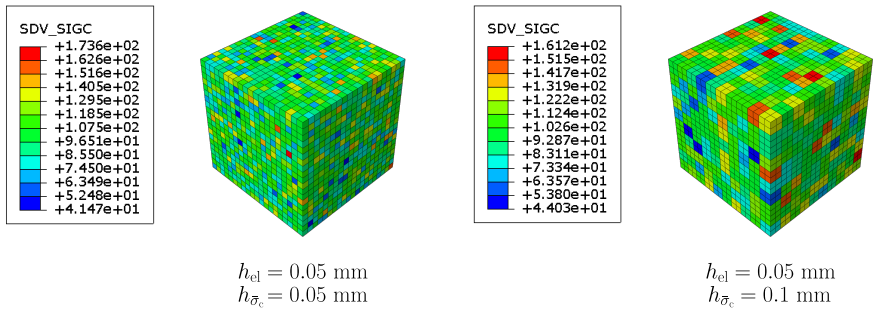

Figure 6.25: Distributed critical stress in models with varying assignment mesh and a constant FE mesh.

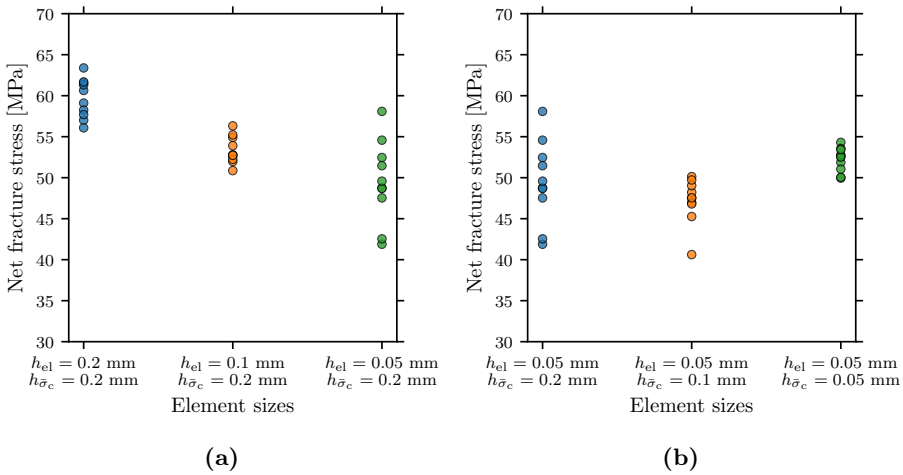

Figure 6.26: Net fracture stress from repeat simulations of multi-element cubes with varying assignment mesh element size and FE mesh element size.

6.4 Summary

- The implementation of the constitutive model has been verified through single-element simulations at different stress states and strain rates. All results could be explained by the constitutive relations, which indicates that the model has been implemented properly.
- A multi-element simulation with complex loading was performed to assess the robustness of the implementation. No instabilities were observed in the simulation.
- The effects of the material parameters on the stress-strain response were studied in a parameter study.
- A brief investigation of the assignment mesh was conducted. For a more thorough study, the reader is referred to Petter Holmström's PhD thesis [46].

7 Constitutive model: Calibration

Now that the constitutive model has been properly verified, the material parameters should be calibrated to real experimental results. This chapter describes the calibration procedure employed in this work and shows a comparison between numerical and experimental results.

7.1 Calibration procedure

The calibration of the constitutive model was done by inverse modelling. The procedure consists of simulating the material tests presented in Chapter 3 and comparing the numerical results with the experimental results. The material parameters were then manually tweaked until a satisfactory agreement between the simulations and the experiments was obtained. Axisymmetric FE models were used in the initial calibration of the hyper-viscoelastic parameters for computational efficiency. After the material parameters were determined, the material tests were simulated again with 3D FE models. The same 3D models were used in the calibration of the fracture parameters. The axisymmetric models featured meshes and boundary conditions similar to their 3D counterparts. As such, only the 3D models are described in the following section.

7.2 Finite element models

The test specimens were modelled with reduced-integration C3D8R elements and "combined" hourglass control in Abaqus. Due to symmetry, only one-eighth of the specimens were modelled. A characteristic element size of 0.1 mm was employed in the gauge area of the smooth specimen and in the notch area of the notched specimens. To achieve proper strain localisation behaviour in the notched specimens, it was necessary to include the clamping region of the specimens. Symmetry was enforced through appropriate boundary conditions on the symmetry planes. A prescribed velocity matching the experimental machine cross-head velocity was applied to the end of the clamping region. The threaded region of the R4 notched compression specimen was modelled when simulating the specimen in tension to achieve the correct initial elastic stiffness. For the compression simulations, the threaded region was omitted and prescribed displacements were applied directly

to the end of the nut region. The hexagonal nuts were idealised as cylinders in the simulations. 10% of the analysis time was spent ramping the velocity to avoid oscillations. All the simulations in this chapter were mass scaled to achieve reasonable computation times when applying the experimental cross-head velocities. The kinetic energy was checked for each simulation and was found to be negligible compared to the external work. The FE models of the test specimens are shown in Figures 7.1 and 7.2.

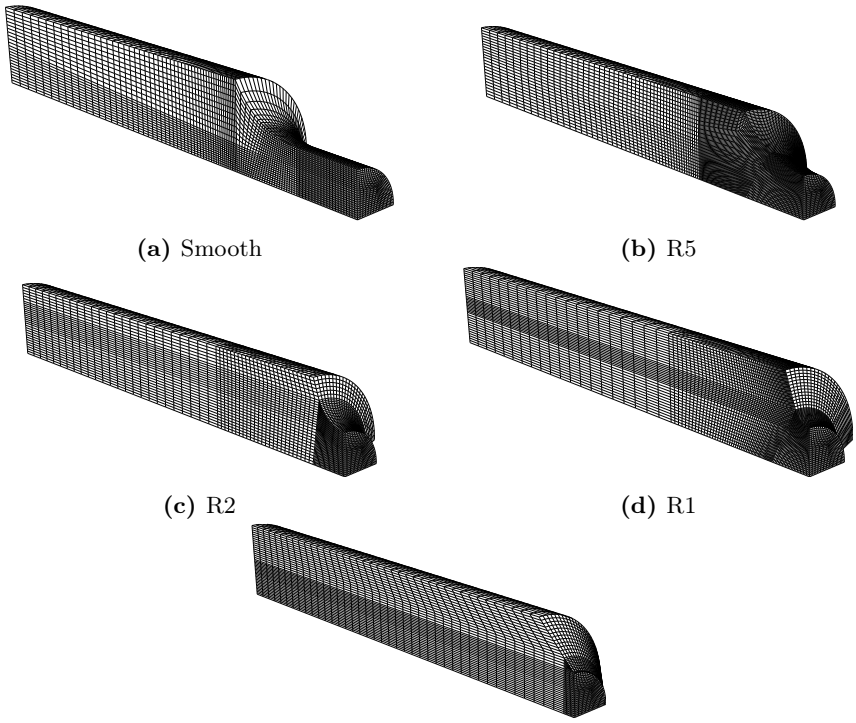

(a) Smooth **(b)** R5

(c) R2 **(d)** R1

(e) R0.2

Figure 7.1: Finite element models of the tensile specimens.

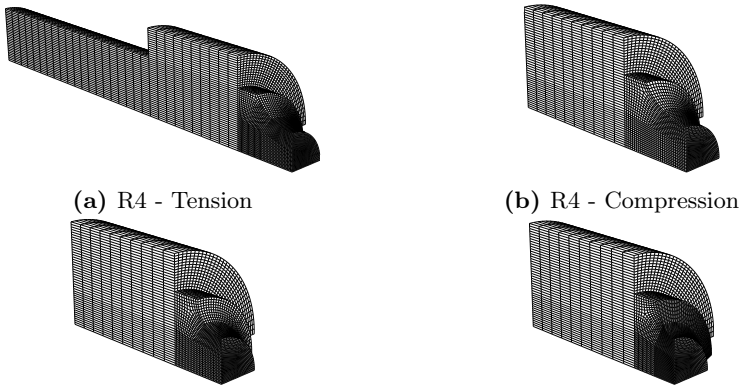

(a) R4 - Tension **(b)** R4 - Compression

(c) R2 **(d)** R1

Figure 7.2: Finite element models of the compression specimens.

The net stress and logarithmic strain components were extracted analogously to the experiments as described in Chapter 3. The current radius, r, of the specimens was extracted by tracking the displacement of a node at the specimen surface, as illustrated in Figure 7.3. The resultant reaction force, F, was calculated by summing the nodal reaction forces in the longitudinal direction. The net stress is then calculated as

$$\sigma = \frac{F}{\pi r^2} \tag{7.1}$$

For the smooth specimens, the longitudinal logarithmic strain component, ε_{l}, was taken as the average longitudinal logarithmic strain at the integration points of four surface elements, as shown in Figure 7.4. For the notched specimens, the isochoric logarithmic strain described in Chapter 3 is employed. The strain measure is calculated from the current radius, r, and reference radius, r_0 as

$$\bar{\varepsilon}_{\mathrm{l}} = -2\ln(r/r_0) \tag{7.2}$$

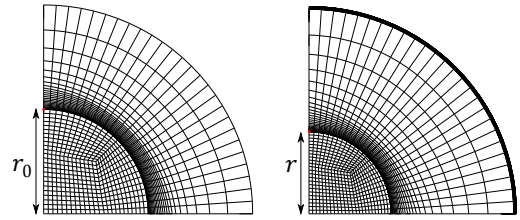

Figure 7.3: The undeformed and deformed cross-section of the FE model of the smooth specimen showing the initial and current radius, r_0 and r, respectively.

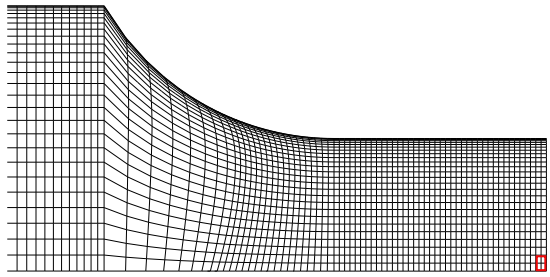

Figure 7.4: The gauge area of the FE mesh of the smooth specimen. The longitudinal logarithmic strain component is extracted from the highlighted elements.

7.3 Hyper-viscoelastic parameters

The results of the calibration of the hyper-viscoelastic parameters are shown in Figures 7.5, 7.6, 7.7 and 7.8 in terms of stress-strain curves and the corresponding material parameters are shown in Table 7.1. In the case of monotonic tension, shown in Figure 7.5 (a), the strain-rate dependent inelastic flow is well described by the model. The strain hardening also agrees with the experiments, though the simulated response curves start to deviate from the experimental ones at large strains. The strain-rate sensitivity is also well captured in the simulations of the loading/unloading tests, as seen in Figure 7.5 (b), but the simulated unloading and subsequent reloading do not reproduce the experimentally observed hysteresis. The relaxation behaviour of the model, as seen in Figure 7.6, replicates the experimental trends where the stress relaxes downwards in the loading phase and upwards in the unloading phase. However, the magnitude of the stress relaxation is underestimated by the model. More accurate relaxation and unloading results could most likely be achieved by expanding the constitutive model to take multiple relaxation times into account, i.e., adding more dashpots, like in the models

by Bergström and Bischoff [47] or van Breemen et al. [48].

Figure 7.7 compares results from the simulations of the notch tensile tests with the experimental data. The pressure dependency of the model is able to adequately describe the net stress at yield for all the notch radii, where the largest deviation is seen in the sharpest notched specimen.

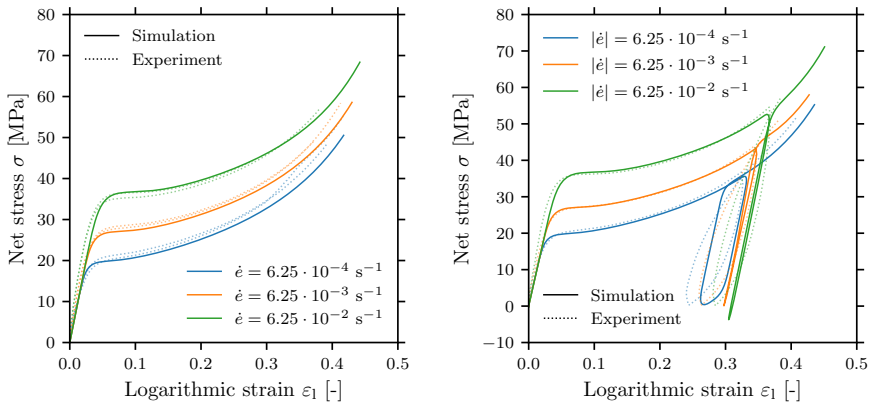

Figure 7.5: Comparison between numerical and experimental stress-strain curves from tensile tests on smooth specimens at different strain rates with **(a)** monotonic loading and **(b)** loading/unloading.

Figure 7.8 (a) shows a comparison between the experimental and numerical results for the compression tests. The yield stress is well predicted for these tests as well, but the strain hardening is overestimated in the simulation of the R4 specimen. This could be a result of the threefold symmetry used in the FE model. In the experiments, the specimens started to experience some small shear deformations due to an eccentricity between the mounts, while the simulated specimens experienced a pure compressive triaxial deformation throughout the entire analysis. The effective chain stretch would thus be overestimated in the simulations, which again would lead to an overestimation of the strain hardening. This effect is studied in more detail in Chapter 7.5.2. Figure 7.8 (b) shows how simulations of the R4 specimens in tension and compression compared with the experimental results. Once again, the yield stress is well described, while a deviation is observed in the strain hardening. In this case, the discrepancy stems from the model itself.

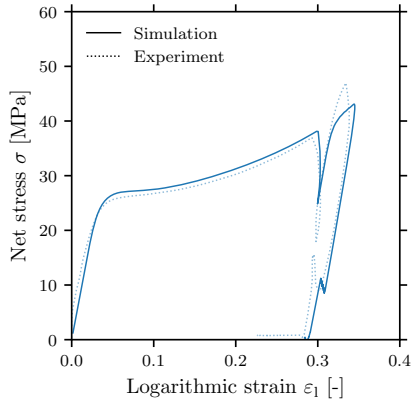

Figure 7.6: Comparison between numerical and experimental stress-strain curve from the simulation of the relaxation test.

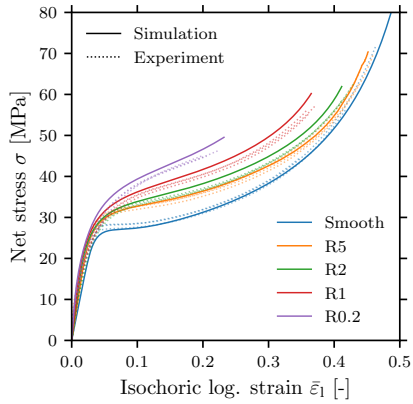

Figure 7.7: Comparison between numerical and experimental stress-strain curves from notch tensile tests.

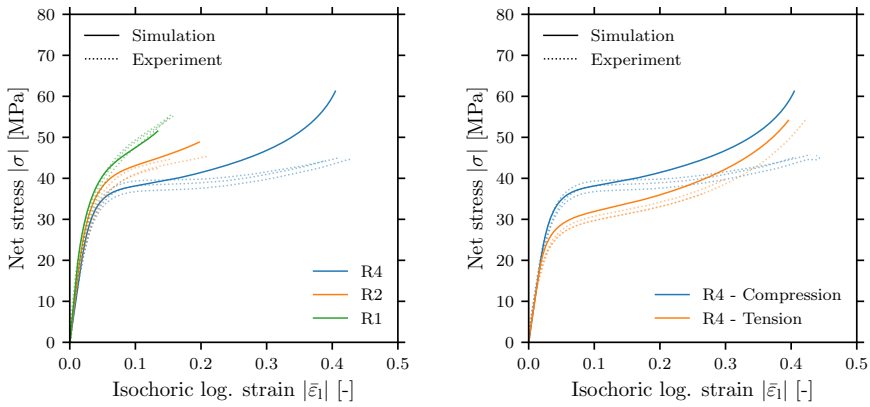

Figure 7.8: Comparison between numerical and experimental stress-strain curves from **(a)** notch compression tests and **(b)** compression and tensile tests on R4 compression specimens.

Table 7.1: Calibrated hyper-viscoelastic parameters.

Part A	μ_A	λ_L						
	[MPa]	[-]						
	6.3	1.22						
Part B	μ_B	κ	$\dot{\gamma}_0$	m	τ_0	τ_{ss}	h	α
	[MPa]	[MPa]	[s^{-1}]	[-]	[MPa]	[MPa]	[MPa]	[-]
	262	2500	10^{-4}	6.7	15.3	13	300	0.1

7.4 Fracture parameters

The calibrated fracture model parameters are compiled in Table 7.2. The mean critical stress was taken as the largest principal stress value observed in a simulated R0.2 specimen at a force level corresponding to the experimental force at fracture. The standard deviation of the fracture stress was determined through a trial-and-error approach. An assignment element size of 0.2 mm, i.e., twice the finite element size, was used in all numerical simulations. The chosen assignment element size provided a scatter in the net failure stress similar to the experimental results while keeping the fracture mode relatively brittle. The results from simulations of the notch tensile tests with the calibrated fracture model are shown in

Figure 7.9. Six repeat simulations with different realisations of the distribution of the critical stress were performed for each test type. Fracture in the simulated tests in Figure 7.9 (a) is indicated by a solid circle. The model captures the experimental trends where both the average net failure stress and the scatter of the failure stress are reduced as the notch radius is decreased. The scatter in the failure stress of the smooth specimen, however, is underestimated.

A comparison between the experimental and simulated fracture modes for the different tensile specimens is shown in Figures 7.10, 7.11, 7.12, 7.13 and 7.14. Note that the results from the FE model have been mirrored for the purpose of visualisation in the aforementioned figures. It is observed that the fracture mode is well described by the model. A clear mesh dependency is seen in the results from the simulation of the R5 specimen, where the crack follows the pattern of the mesh – giving the appearance of a cup and cone fracture.

Even though the numerical results from the R0.2 specimen look similar to the experimental results in Figure 7.14, the simulated crack velocity is magnitudes slower than the experimental one. This can be seen by looking at the force vs. displacement curves in Figure 7.15 (a). Figure 7.15 (b)-(e) show the deformed FE model throughout the fracture process. Fracture is seen to initiate in the surface elements before propagating slowly towards the centre of the specimen. The slow fracture propagation comes from the highly localised stresses in the R0.2 specimen and the stochastic fracture stress distribution. Due to the sharp notch, the principal stresses in the surface elements are much higher than in the internal elements. When surface elements are eroded, the reduction in cross-sectional area will cause an increase in stress levels for the next elements in line to be eroded. However, the fracture stress still needs to be exceeded for fracture to occur in these elements. With the stochastic fracture stress distribution, it is not guaranteed that the fracture stress of an internal element is equal to or lower than that of a surface element. In fact, Figure 7.16 shows how the fracture stresses of most internal elements along the symmetry plane in the radial direction are larger than that of the surface element. In this case, the fracture will propagate slowly until the increase in stress levels from the reduction in cross-sectional area becomes great enough for a brittle fracture to occur. This corresponds to point (d) on the force-displacement curve in Figure 7.15 (a).

Table 7.2: Calibrated fracture parameters.

$\bar{\sigma}_{\mathrm{c,mean}}$ [MPa]	$\bar{\sigma}_{\mathrm{c,std}}$ [MPa]	$\bar{\sigma}_{\mathrm{c,min}}$ [MPa]	G_{f} [N/mm]
130	22	40	0.5

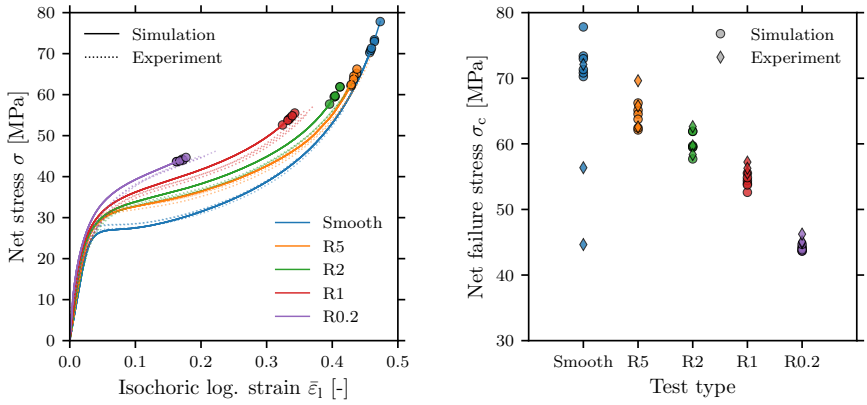

Figure 7.9: Numerical results from repeat simulations of fracture in smooth and notched tensile specimens showing **(a)** net stress vs. isochoric axial strain and **(b)** net failure stresses for each specimen geometry.

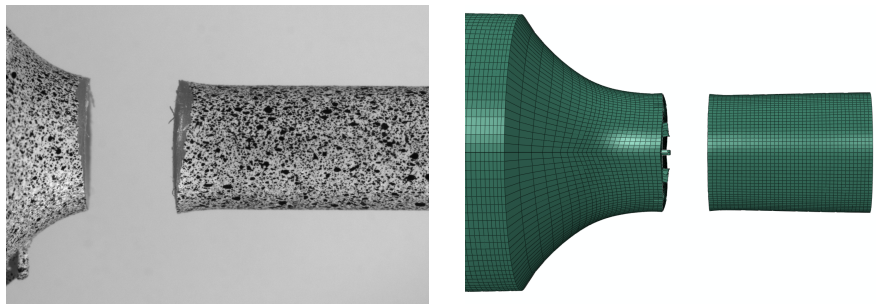

Figure 7.10: Comparison between the fracture mode in **(a)** a tensile test of a smooth 90° specimen and **(b)** the corresponding simulation with the fracture model.

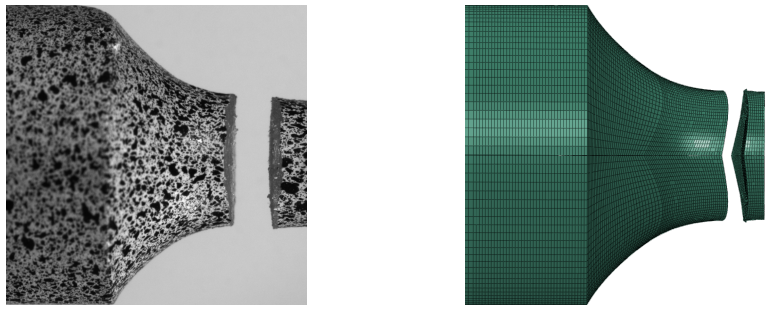

(a) **(b)**

Figure 7.11: Comparison between the fracture mode in **(a)** a tensile test of an R5 specimen and **(b)** the corresponding simulation with the fracture model.

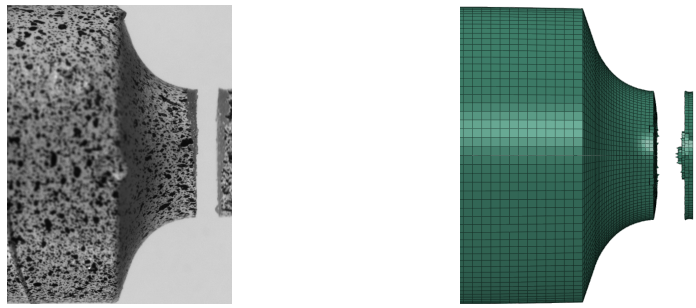

(a) **(b)**

Figure 7.12: Comparison between the fracture mode in **(a)** a tensile test of an R2 specimen and **(b)** the corresponding simulation with the fracture model.

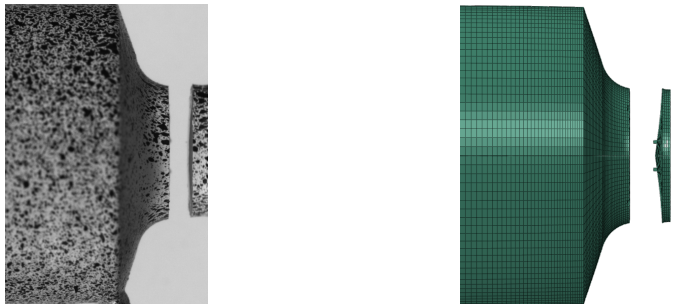

(a) **(b)**

Figure 7.13: Comparison between the fracture mode in **(a)** a tensile test of an R1 specimen and **(b)** the corresponding simulation with the fracture model.

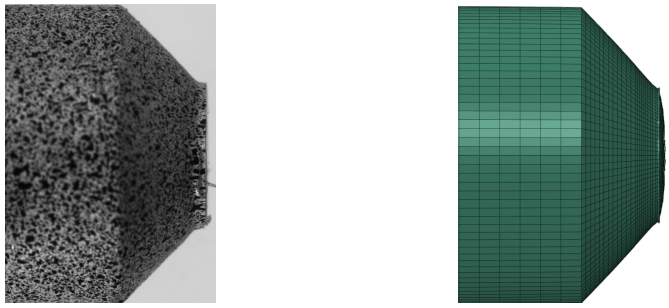

(a) **(b)**

Figure 7.14: Comparison between the fracture mode in **(a)** a tensile test of an R0.2 specimen and **(b)** the corresponding simulation with the fracture model.

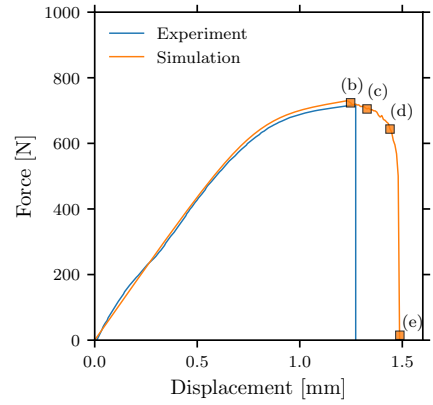

(a)

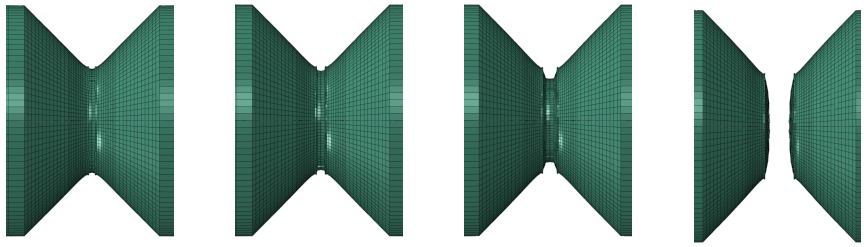

(b) **(c)** **(d)** **(e)**

Figure 7.15: **(a)**: Comparison between the experimental and simulated force vs. displacement curve from an R0.2 notch tensile test and **(b)**-**(e)**: the deformed FE model at force and displacement levels indicated in **(a)**.

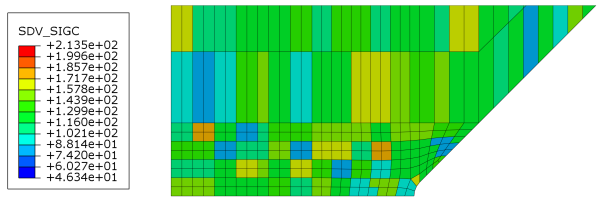

Figure 7.16: Fracture stress distribution in a longitudinal cross-section of an R0.2 FE model.

7.5 Numerical investigations

7.5.1 The effects of symmetric boundary conditions

For the sake of computational efficiency, only one-eighth of the material test specimens were modelled. This is not expected to influence the general stress-strain behaviour in any major way, as the experimental deformation modes were symmetric. However, it could affect the fracture initiation since the simulated volume is only one-eighth of the physical volume of the test specimens which would reduce the likelihood of encountering low critical stresses. This effect is expected to be most noticeable in the smooth specimens, due to their relatively large gauge area. To check the effects of modelling the tensile tests with symmetric boundary conditions, additional simulations of the full smooth tensile specimens were performed with different realisations of the distribution of the critical stresses. The mesh of the full smooth specimen is shown in Figure 7.17.

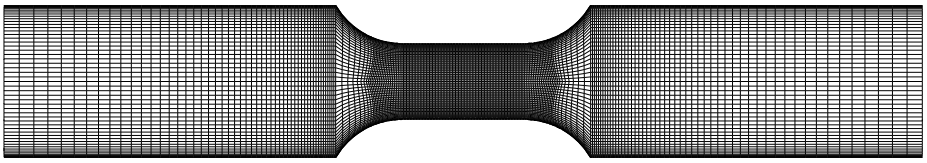

Figure 7.17: FE mesh of the full smooth tensile specimen.

The results from the simulations are shown in Figure 7.18 **(a)** and **(b)** in terms of net stress vs. isochoric logarithmic strain curves and a plot of the net failure stresses respectively. As expected, the stress-strain curves from the simulations of the full tensile specimen are identical to the results from the simulations performed with symmetric boundary conditions before fracture. One of the full-specimen simulations produced a noticeably lower net failure stress than any of the simulations with symmetry. To study whether this is an effect of the larger volume of the FE model or simply a fluke, additional simulations should be performed to draw any meaningful conclusions. However, due to time and computational constraints, this investigation will not be pursued any further.

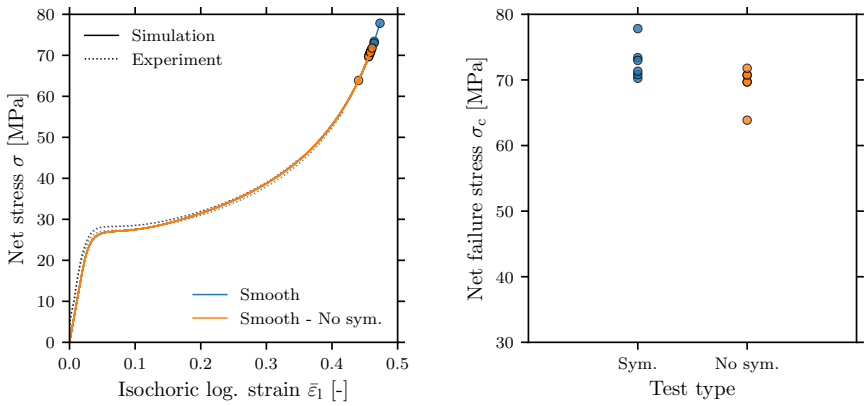

Figure 7.18: Results from simulations of a smooth tensile test modelled with and without symmetry showing **(a)** stress vs. strain curves and **(b)** net failure stresses from repeat simulations.

7.5.2 The effect of mount-eccentricity in the notch compression tests

In Chapter 7.3 it was hypothesised that the simulated and experimental stress-strain curves from the R4 compression tests deviated due to an eccentricity in the mounts in the experimental setup. To test this hypothesis, the R4 compression test is simulated once more, but with the entire specimen modelled and by including a small transverse component to the displacement in addition to the longitudinal component. The mesh and boundary conditions of the full R4 compression model are shown in Figure 7.19. The boundary conditions are enforced by applying MPC beam constraints to the left- and rightmost nodes and constraining them to follow the motion of their respective master node. The left-hand master node in Figure 7.19 is fixed against displacements and rotations in all directions. The right-hand master node has a prescribed velocity in the x- and y-directions while all other degrees of freedom are fixed. The transverse master node velocity is $v_y = 0.002\,\mathrm{mm/s}$, which produced a final transverse displacement, i.e., eccentricity, of 0.44 mm. The minimum cross-sectional diameter of the full R4 model was calculated in Python by looping through nodes on opposite sides of the notch root in the xy-plane and calculating the distance between them in the y-direction. This procedure is analogous to the edge tracing performed in the experiments.

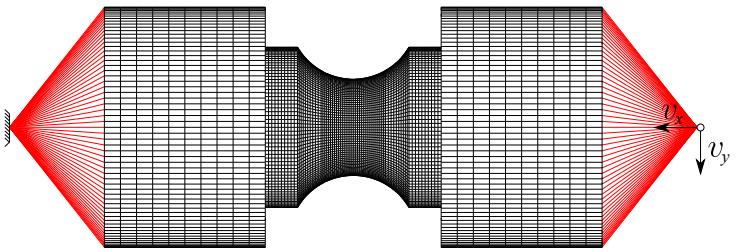

Figure 7.19: FE mesh of the full R4 compression specimen. MPC beam constraints are shown in red.

The deformed shape of the full R4 compression simulation is shown in Figure 7.20 **(b)** together with the results from the simulation performed with symmetric boundary conditions in Figure 7.20 **(a)**. The stress-strain curves from both simulations are plotted together with the experimental stress-strain curves in Figure 7.20 **(c)**. The results reveal no noticeable difference between the two simulations, besides two small jumps in strain levels in the curve from the simulation with an eccentricity. These strain jumps are simply artefacts from the routine used to calculate the minimum diameter of the model. The effect of the mount-eccentricities can therefore not explain the discrepancy between the simulated and experimental stress-strain curves. Another explanation could be that the eight-chain model is not able to describe the strain-hardening behaviour of the material in compression.

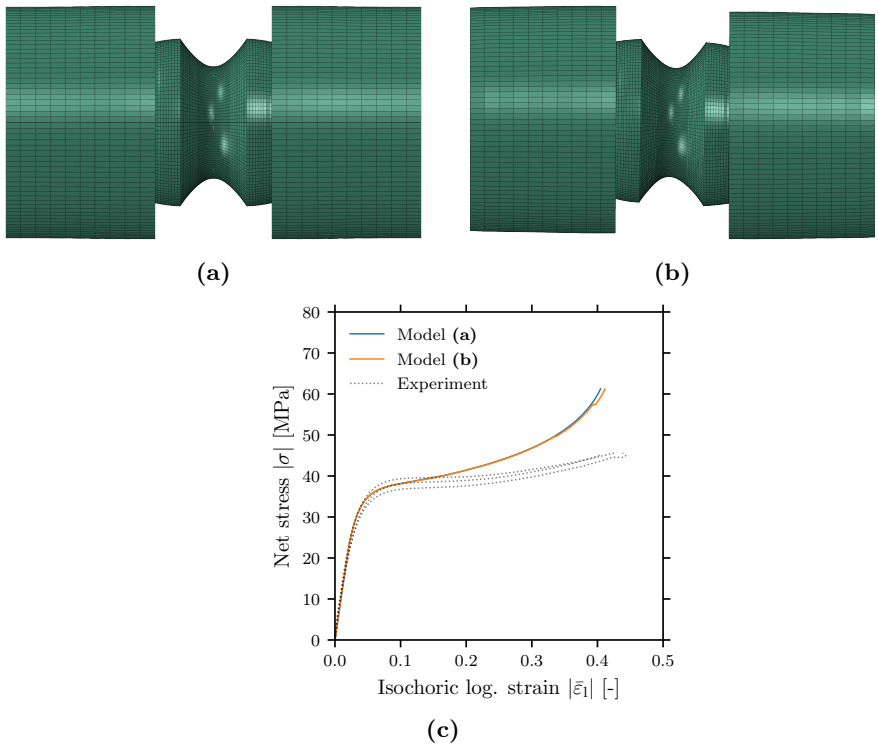

Figure 7.20: Deformed geometry of the FE model of **(a)** the R4 compression test modelled with symmetric boundary conditions and **(b)** the R4 compression test modelled with full geometry and a slight eccentricity together with **(c)** their corresponding stress vs. strain curves. Note that the mesh in **(a)** has been mirrored for the purpose of visualisation.

7.6 Summary

- An inverse modelling approach was used to calibrate the parameters of the constitutive model to experimental data.
- The general stress vs. strain behaviour is captured well by the model. The model is able to describe both the strain-rate dependency and the pressure dependency of the flow stress. The stress-relaxation behaviour, however, is only captured qualitatively, as the magnitude of the stress-relaxation is underestimated by the model.

- The stochastic fracture initiation model captures the trend in which both the scatter and the magnitude of the net failure stress are reduced as the notch radius is decreased.
- The brittle fracture mode is captured by the fracture model, but the crack velocity is underestimated.

8 Constitutive model: Validation

As seen in the previous chapter, the proposed model can describe the mechanical behaviour observed in the material tests. However, these tests were directly used in the calibration of the model. In order to assess the model's performance for more complex stress states and its ability to extrapolate beyond the calibration data, additional tests are required. For this purpose, the tests presented in Chapter 4 are simulated with the calibrated constitutive model and compared with the experimental results. This chapter presents the numerical models of the validation tests and how the numerical results compare with the experimental ones.

8.1 Simulation of the lattice structure compression tests

The first validation case is the lattice compression tests presented in Chapter 4. These tests provide a complex combination of tension and compression, in contrast to the simpler stress states of the material tests. Additionally, the dynamic tests feature much higher strain rates than what the model has been calibrated for, which will test its ability to extrapolate beyond the calibration data.

8.1.1 Finite element model

The geometry of the octet-truss lattice structure is quite complex, which makes creating a structured mesh challenging. Due to the periodic nature of the structure, however, it is possible to mesh only a small part of the geometry and then assemble the rest through symmetries. The approach chosen herein is to create a structured mesh on one half of a single strut of the structure, and then use the radial and linear pattern tools in Abaqus CAE to assemble the rest of the structure. This procedure is illustrated in Figure 8.1.

The fracture parameters of the constitutive model were calibrated with an assignment element size of 0.2 mm. As such, the element size of the finite element model should not exceed this. The FE mesh of the lattice structure has eight elements over the thickness of each strut, which gives an element size of approximately 0.19 mm. The same element formulation as in the simulations of the material

tests was used, i.e., reduced-integration linear solid elements with "combined" hourglass control.

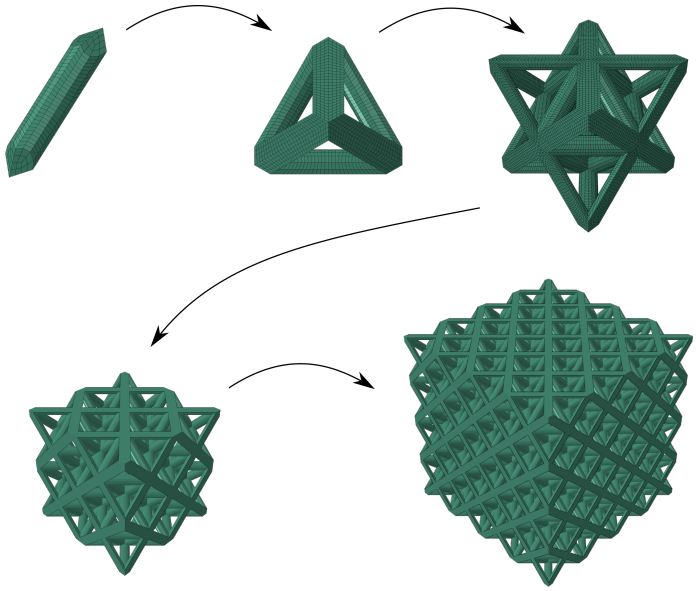

Figure 8.1: Assembly of the full lattice structure.

Two different models are used in the simulation of the lattice structures; one for quasi-static simulations and one for dynamic simulations. As the quasi-static test results showed a symmetric deformation mode, three-fold symmetry is used in the simulations of these tests, i.e., only one-eighth of the structure is modelled. Symmetry in the x- and z-directions is enforced through boundary conditions. Symmetry in the y-direction is enforced by including a rigid plate in the symmetry plane to simulate the contact between struts on each side of the symmetry plane. Another rigid plate with a prescribed velocity is used to represent the top platen from the experiment. Since the model uses symmetry about the xz-plane, half of the cross-head velocity, v, from the experiments is applied to the top plate. The velocity is gradually applied using a tabulated smooth amplitude where 10% of the simulation time is used to increase the velocity to its final value in order to avoid oscillations. Friction is included for the contact between the lattice and the plates and for lattice self-contact. In both cases, the coefficient of friction from the experiments is unknown and is simply set to 0.1 for both steel-polymer and polymer-polymer interactions. The "General Contact" formulation with a penalty friction tangential behaviour and "Hard" contact normal

behaviour is used in all analyses. An illustration of the numerical model is shown in Figure 8.2. Note that only boundary conditions in the x-direction are shown in the illustration, but similar boundary conditions also exist in the z-direction. Due to the quasi-static conditions, simulations were run with mass scaling. The material density was scaled by a factor 10^{10}, 10^8 and 10^6 in the simulations with $v = 3\,\text{mm/min}$, $v = 30\,\text{mm/min}$ and $v = 300\,\text{mm/min}$ respectively, such that the number of increments, and the CPU time, is similar for each analysis. The kinetic energy was checked for each analysis and found to be negligible compared to the external work.

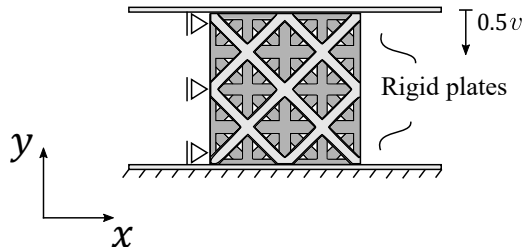

Figure 8.2: Illustration of the boundary conditions applied to the simulations of the quasi-static lattice compression tests.

The finite element model of the dynamic tests contains a mesh of the entire lattice structure, as an asymmetric deformation mode was observed in the experiments. The contact formulations and friction coefficients remain the same as for the quasi-static model. The top plate acts as the impactor from the experiment and is given a mass, m_p, and initial velocity, v_0. No boundary conditions are applied to the lattice structure and it is held in place purely by friction, like in the experiments. An illustration of the numerical model is shown in Figure 8.3. No mass scaling was used in the dynamic simulations.

In both models, the reaction force and the vertical displacement of the reference point of the top plate are extracted and used in the comparison with the experimental results.

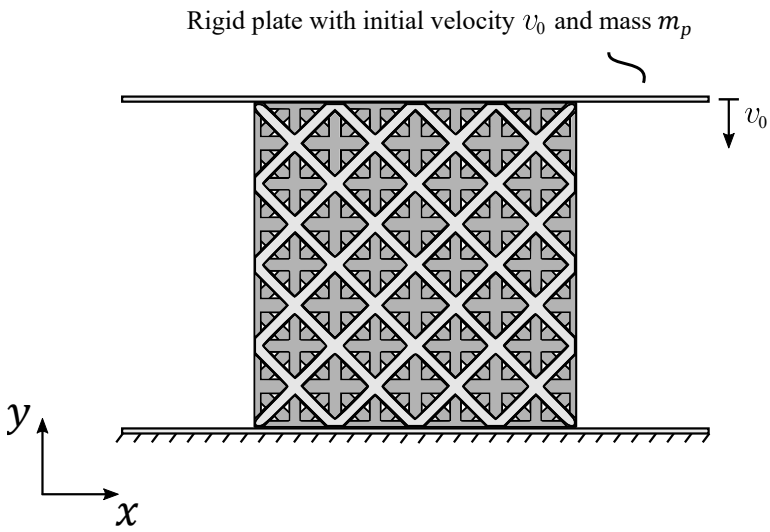

Figure 8.3: Illustration of the boundary conditions applied to the simulations of the dynamic lattice compression tests.

8.1.2 Results and discussion

Results from the simulations of the quasi-static tests are shown in Figure 8.4 in terms of force vs. displacement curves. The 300 mm/min simulation encountered convergence issues near the end of the simulation time due to excessive deformation arising from contact instabilities during the densification stage. As such, the force-displacement curve from the 300 mm/min simulation is cut off prematurely compared with the other simulations. Only one simulation was performed for each cross-head velocity as hardly any fractures were observed in the experiments. The simulated force-displacement curves follow the experimental ones closely but slightly overestimate the force levels. The largest discrepancy is seen for the simulation of the 300 mm/min test, where the peak force is overestimated by approximately 8%. One possible explanation for the overestimated peak force is that the strain rates in the 300 mm/min test are larger than any of the material tests used to calibrate the strain-rate sensitivity of the model. Thus, extrapolation beyond the calibration data might lead to an inaccurate representation of the strain-rate sensitivity of the material. The strain-rate dependent strain softening, however, seems to be well captured for all test velocities, as can be seen in the slope of the force-displacement curves immediately after the peak force is reached. A contour plot of the effective inelastic strain rate, $\dot{\gamma}_{\mathrm{B}}$, in the 300 mm/min simulation is shown in Figure 8.5 which shows that the strain rates

are of the order of $10^{-1}\,\mathrm{s}^{-1}$.

Figures 8.6, 8.7 and 8.8 show the deformed FE models throughout the simulations of the 3 mm/min, 30 mm/min and 300 mm/min tests respectively. Three images are shown from each simulation: one immediately after the peak force is reached, one during the plateau of the force-displacement curve and one from the last frame of the simulation. Note that the results have been mirrored for the sake of visualisation and recall that only one-eighth of the model was actually simulated. It is observed that all simulations result in quite similar deformation modes.

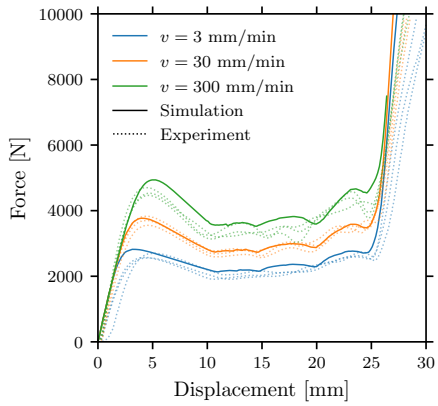

Figure 8.4: Force vs. displacement curves comparing numerical results with experimental results from the quasi-static octet-strut lattice structure compression tests.

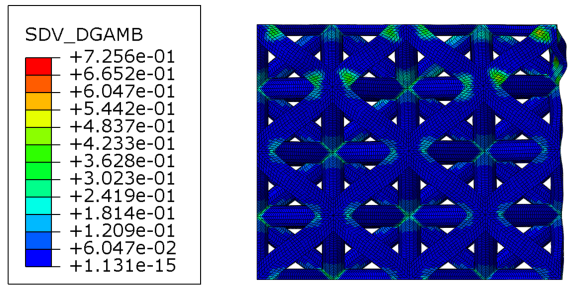

Figure 8.5: Contour plot of the equivalent inelastic strain rate, $\dot{\gamma}_{\mathrm{B}}$, from the simulation of a lattice structure compressed with a cross-head velocity of 300 mm/min. The contour plot is extracted from the point in the simulation time at which the peak force occurs.

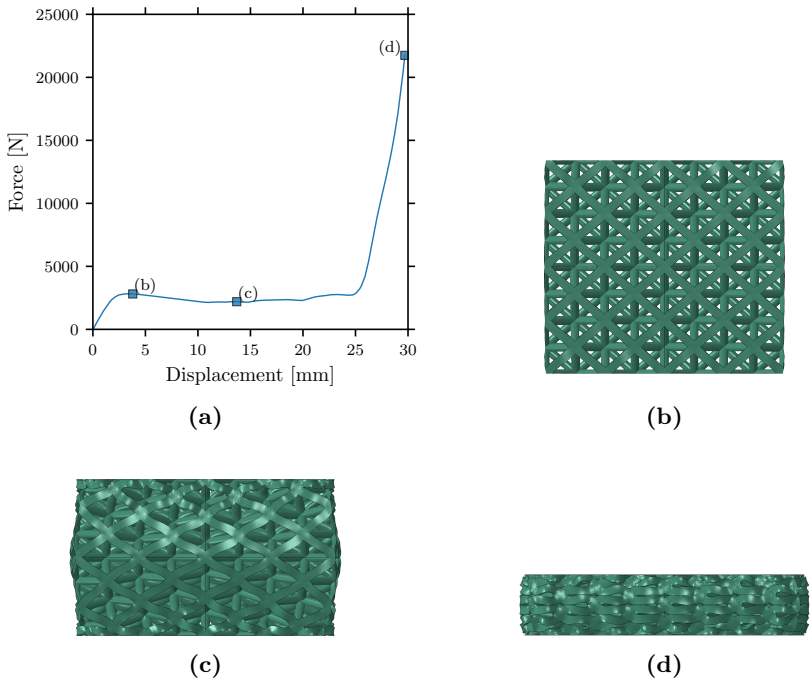

Figure 8.6: **(a)**: Force vs. displacement curve from the simulation of the quasi-static compression test with $v = 3\,\mathrm{mm/min}$ and **(b)-(d)**: the deformed shape of the lattice structure at points in the deformation history indicated in the force vs. displacement curve.

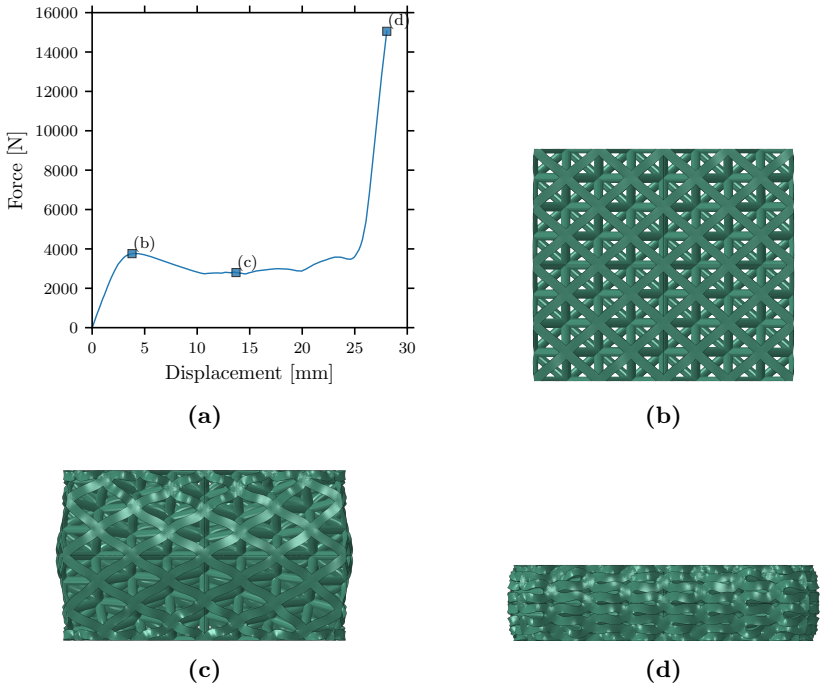

Figure 8.7: **(a)**: Force vs. displacement curve from the simulation of the quasi-static compression test with $v = 30\,\mathrm{mm/min}$ and **(b)-(d)**: the deformed shape of the lattice structure at points in the deformation history indicated in the force vs. displacement curve.

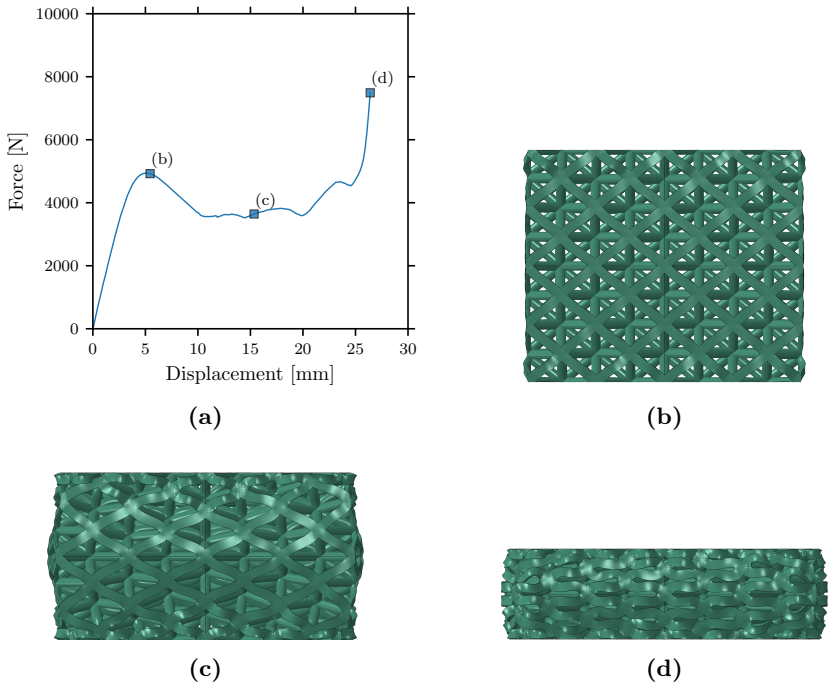

Figure 8.8: **(a)**: Force vs. displacement curve from the simulation of the quasi-static compression test with $v = 300\,\mathrm{mm/min}$ and **(b)-(d)**: the deformed shape of the lattice structure at points in the deformation history indicated in the force vs. displacement curve.

When simulating the dynamic compression tests, it became apparent that the value of the critical time interval for fracture initiation, Δt_c, has a significant impact on the simulated response of the lattice structure. Due to the combination of small elements and no mass scaling, the critical time increment of the simulations is on the order of 10^{-8} s, which is much smaller than the default value of Δt_c used so far, which is 10^{-4} s. When Δt_c is much larger than the critical time increment, the fracture propagation speed is underestimated in the simulations. To study how Δt_c affects the simulated dynamic compression of the octet-truss lattice structure, simulations of the test with $v_0 = 4\,\mathrm{m/s}$ were performed with different values of Δt_c.

The force vs. displacement curves from the simulations are shown in Figure 8.9. The curves show a reduction of the peak force and an increase of the maximum displacement as Δt_c is reduced, which indicates that the simulated material becomes more brittle for lower values of Δt_c. The observation above is confirmed in Figures 8.10 (a)-(f) which show the deformed shape of the lattice structure for different values of Δt_c – revealing a more brittle response as Δt_c is reduced. Figures 8.10 (g)-(h) show images from the experiments captured at the same point in time as the simulations. Among the different simulations, the values of $\Delta t_c = 10^{-5}$ s and $\Delta t_c = 2 \cdot 10^{-5}$ s seem to give results that best match with the experimental results, where the former value most closely matches the experimental deformation mode. In contrast, the latter most closely matches the experimental force-displacement curves. Since $\Delta t_c = 10^{-5}$ s gives a more accurate representation of the experimental failure mode, this value was chosen when simulating the dynamic compression test with $v_0 = 5\,\mathrm{m/s}$. Moreover, the chosen value underestimates the peak force and post-fracture force levels and gives conservative results in energy absorption applications, which is always preferable to the opposite case.

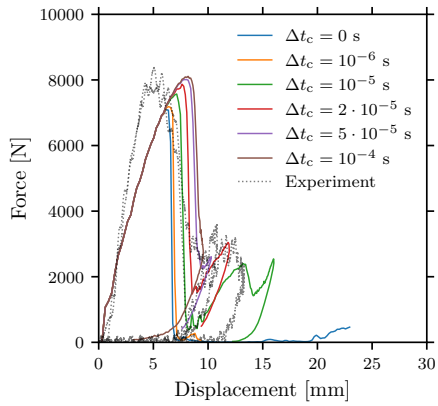

Figure 8.9: Force vs. displacement curves showing how the parameter Δt_c affects the response of the numerical model of the dynamic compression test with $v_0 = 4\,\mathrm{m/s}$.

With the choice of Δt_c out of the way, it is time to compare the response of the simulated dynamic compression tests with the experimental results. Figure 8.11 shows the force vs. displacement curves from both simulations and experiments for both initial velocities. Only one realisation of the critical stress distribution is used for each simulation. The first noticeable difference between the simulations and the experiments is the underestimation of the initial elastic stiffness in the simulations. The same observation can be seen in the simulations of the material tests in Chapter 7 and in the simulations of the quasi-static lattice compression tests, but the effect is made more significant in the dynamic compression tests due to the high strain rates. The underestimation of the initial stiffness consequently results in an overestimation of the displacement at peak force. The peak force is slightly underestimated for both simulations, but the trend of a higher initial velocity resulting in a higher peak force is captured. As a consequence of the chosen value of Δt_c, the force levels after the peak force are underestimated, while the maximum displacement is slightly overestimated. Overall, the simulated force vs. displacement curves agree with the experimental results quite well – especially considering how significantly higher the strain rates are in these tests compared with the calibration data.

As seen from the simulation results in this section, the calibrated material model is able to adequately predict the response of lattice structures compressed over a wide range of strain rates. This, in turn, demonstrates the ability of the material model to handle complex stress states and to extrapolate beyond the calibration

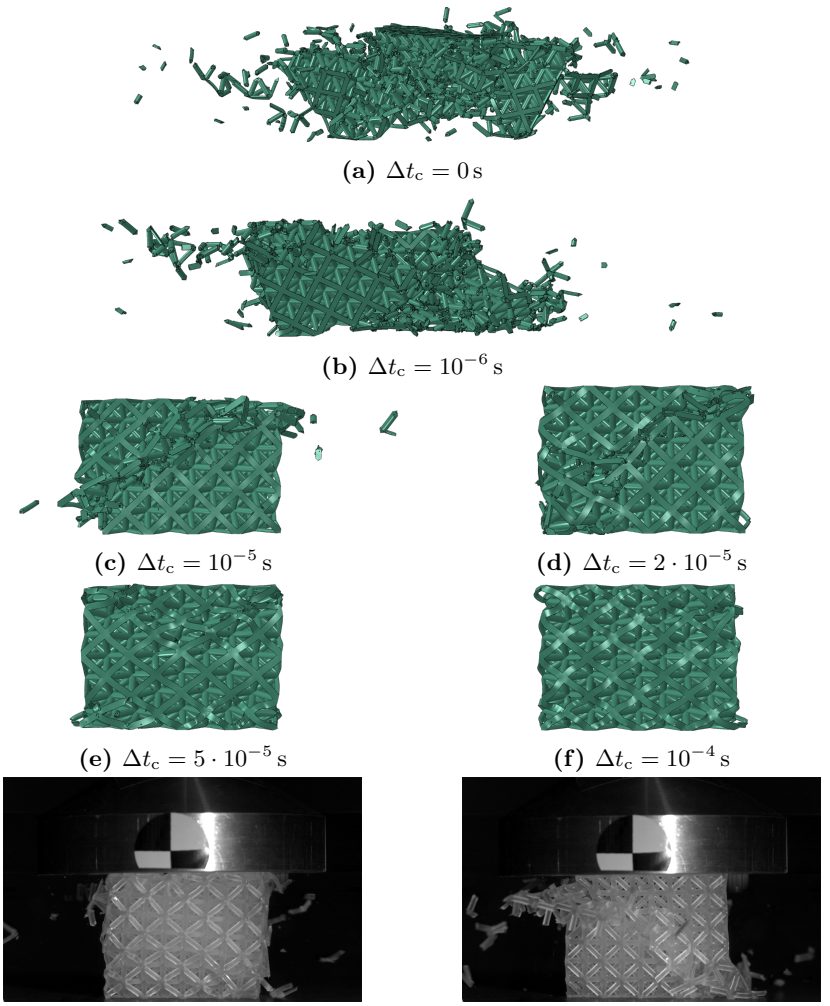

(a) $\Delta t_c = 0\,\mathrm{s}$

(b) $\Delta t_c = 10^{-6}\,\mathrm{s}$

(c) $\Delta t_c = 10^{-5}\,\mathrm{s}$

(d) $\Delta t_c = 2 \cdot 10^{-5}\,\mathrm{s}$

(e) $\Delta t_c = 5 \cdot 10^{-5}\,\mathrm{s}$

(f) $\Delta t_c = 10^{-4}\,\mathrm{s}$

(g)

(h)

Figure 8.10: **(a)-(f)**: Images from simulations of dynamic compression tests with $v_0 = 4\,\mathrm{m/s}$ performed with different values of the critical time interval for fracture initiation, Δt_c and **(g)-(h)**: images from the two experiments for reference. All images shown are captured 3 ms after impact.

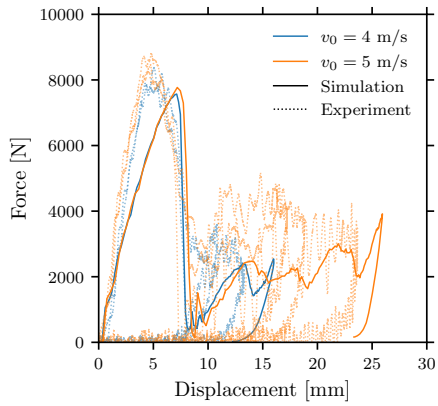

Figure 8.11: Force vs. displacement curves comparing numerical results with experimental results from the dynamic octet-strut lattice structure compression tests.

data. Even though the results were satisfactory, some improvements could still be made to the model. One way to implement a strain-rate-dependent elastic stiffness, as observed in the experiments, would be to extend the model to take multiple relaxation times. Thinking in terms of rheological models, this would mean adding additional spring-dashpot networks in parallel with the current model. This approach was applied by van Breemen et al. [48] to extend the Eindhoven Glassy Polymer model. Such an implementation is relatively straightforward but requires the identification of several additional material parameters. Another aspect not investigated in this work is the effect of imperfections in the 3D-printed lattice structures. The FE model is based on the CAD geometry, and any imperfections in the 3D-printed structures due to either warping or shrinkage are not taken into account in the simulations. Since the octet-truss lattice structure is a stretching-dominated structure [33], it is expected to fail from buckling of the struts when compressed. The buckling load of the struts will thus be overestimated by the idealised FE model when small eccentricities in the struts and deviations in the cross-sectional area of the struts are not taken into account. This might be part of why the force levels are slightly overestimated in the simulations of the quasi-static compression tests.

8.2 Simulation of the three-point-bending tests

The second validation case is the three-point bending tests on notched specimens presented in Chapter 4. These tests provide a combination of tension and compression without the strong geometric effects of the lattice tests. The fracture initiation and the fracture propagation behaviour of the model will be tested due to the off-centre notches in the test specimens.

8.2.1 Finite element models

The finite element model of the R1.25 three-point bending test is shown in Figure 8.12. The specimen actually consists of three parts joined together by "tie" constraints – two coarsely meshed parts on either side of the notch area, which are expected to undergo elastic deformation, and the finely meshed area around the notch where fracture and inelastic deformation are expected to occur. Only the part containing the notch area differs between the models of the R1.25 and R2.50 specimens. The supports and the punch were modelled as analytical rigid parts. Note that the parts of the mesh making contact with the supports are locally refined to improve the contact behaviour. Both structured and random meshing algorithms were studied in the simulations and the meshes can be seen in Figure 8.13. The transition from the coarse mesh to the fine mesh is shown in Figure 8.14. An element size of 0.1 mm was used around the notch together with an assignment mesh element size of 0.2 mm, as in the material test simulations. To reduce the computational time, symmetry boundary conditions were applied to the xy-plane. The element formulation was the same as for the simulations of the material tests and the lattice structures; reduced-integration solid elements with "combined" hourglass control. A mass-scaling factor of 10^8 was used to achieve reasonable computation times. The total kinetic energy was checked for all analyses and found to be negligible compared with the external work, indicating that the mass scaling was not too severe.

The supports and the punch interact with the mesh of the bending specimens through the "General Contact" algorithm. The normal and tangential contact behaviours are set to "Hard" contact and penalty friction respectively. The coefficient of friction was set to 0.1 as in the lattice compression simulations. To reduce spurious oscillations in the results, 10% of the analysis time is spent gradually ramping up the velocity of the punch to the experimental value of 3 mm/min. The reaction force and the displacement of the reference point of the punch were extracted from the analyses and compared with experimental force-displacement curves.

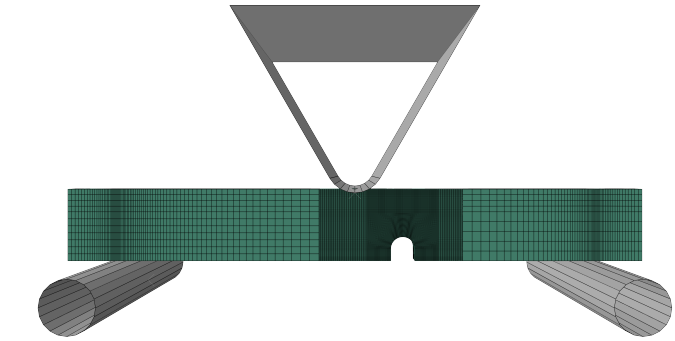

(a)

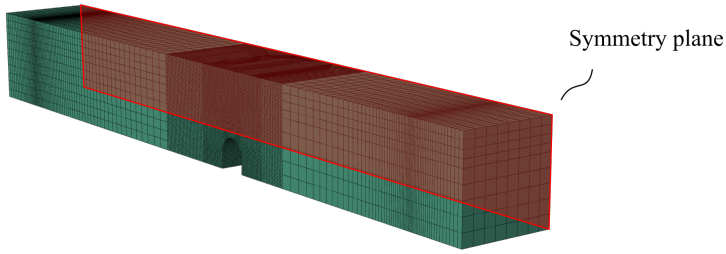

(b)

Figure 8.12: **(a)**: FE model of the three-point bending test of the R1.25 specimen and **(b)**: an alternate view showing the symmetry plane of the model.

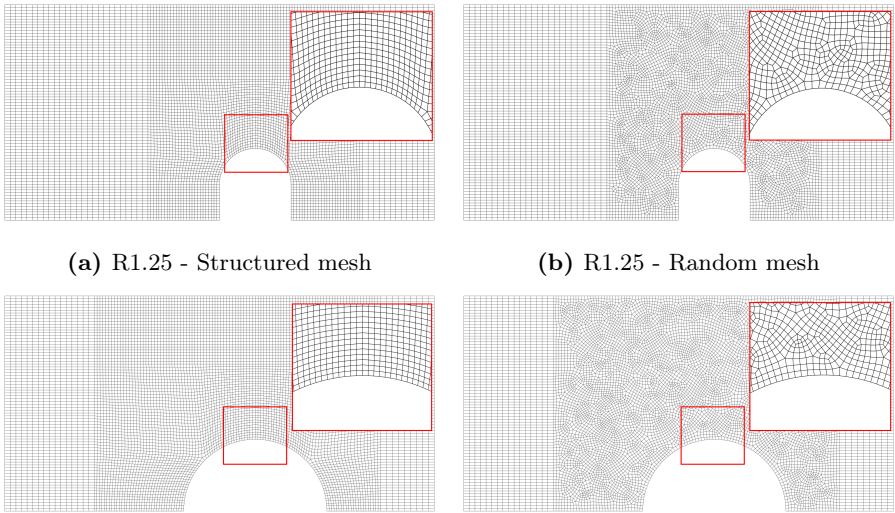

(a) R1.25 - Structured mesh

(b) R1.25 - Random mesh

(c) R2.50 - Structured mesh

(d) R2.50 - Random mesh

Figure 8.13: The mesh around the notch of the three-point bending specimens.

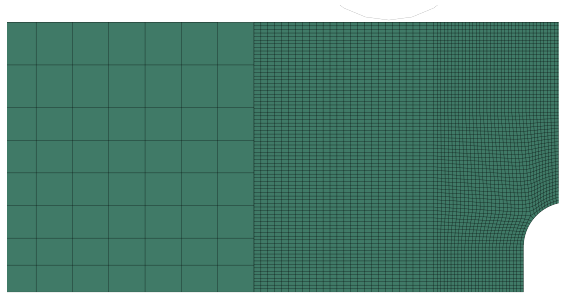

Figure 8.14: The transition from a coarse mesh to a fine mesh by a tie constraint.

8.2.2 Results and discussion

The force vs. displacement curves from the simulations are shown in Figure 8.15 and compared with the experimental results. Each simulation type was run three times with a different realisation of the critical stress distribution to compare the scatter in the force and displacement at failure between the simulations and the experiments. The results from both specimen types show an underestimation of the force at yielding and an overestimation of the displacement at failure, but the overall shape of the simulated force-displacement curves is similar to the experimental ones. The initial elastic stiffness, on the other hand, is well captured which indicates that the geometry and boundary conditions are properly modelled. The underestimated force levels contrast the simulations of the lattice compression tests and the notch material tests where the simulated results generally overestimated the forces and stresses. The reason for this underprediction is not clear. Since the model was able to predict the response of notched specimens in tension and compression, it is reasonable to expect the model to be able to predict the response of notched specimens experiencing bending as well. One possible explanation could be that the assumption of a linear pressure dependency of the effective shear strength, as shown in Eq. 5.28, is too simple to describe the pressure sensitivity of the material. A more accurate modelling of the pressure sensitivity could be to use an exponential pressure dependency of the effective shear strength [49] or by modelling inelastic flow with a pressure-dependent yield surface like the Raghava [50] model or the Deshpande-Fleck [51] model, though this last suggestion would substantially alter the model as it requires the inclusion of a friction element in the rheological model. Note that the calibrated model also underestimates the experimental results in some of the simulations of smooth and notched specimens in Chapter 7, but not to the same extent as observed in the three-point bending simulations.

As the external forces on a solid body need to be in equilibrium with the internal stresses, an underestimation of the force means that the stresses are underestimated as well. Since the fracture initiation criterion of the constitutive model is stress-based, fracture occurs too late in the simulations compared to the experiments, as seen in Figure 8.15. This goes to show that the fracture initiation model only gives good predictions as long as the stress-strain relationship is adequately captured. Nonetheless, the fracture model does predict scatter in the displacement at failure.

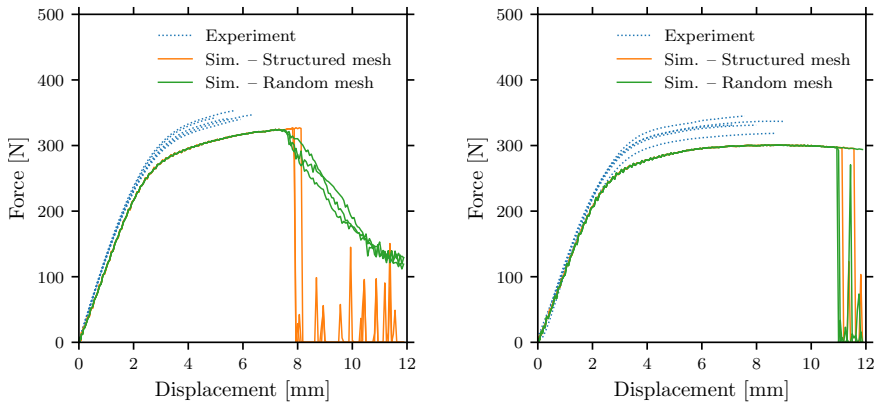

(a) R1.25 **(b)** R2.50

Figure 8.15: Force vs. displacement curves from repeat simulations of three-point bending tests and from experiments.

No difference is seen between the structured and random mesh before fracture. After fracture the random mesh results in a ductile fracture mode in the R1.25 specimen, while the structured mesh gives a brittle fracture mode which can be seen clearly in the post-fracture response in the force-displacement curves. The crack patterns from these simulations are shown in Figure 8.16 (a) and (b). The crack paths from the R1.25 structured mesh clearly follow the pattern of the mesh which results in straight cracks. The cracks start to propagate vertically and then change direction horizontally briefly before continuing on a vertical path. The change in direction as the crack propagates through the thickness of the beam is similar to the experimental results seen in Figure 8.16 (c). The crack paths from the R1.25 random mesh are noticeably shallower than those seen in the structured mesh. Interestingly, the crack paths slant towards the right-hand side in these simulations which is the opposite direction of the experimental results. Even though the mesh was intended to be random, there might still exist a bias in the mesh which promotes crack propagation in this direction. This might also explain why the random mesh gives a less brittle fracture mode. The mesh could promote fracture along a path which does not release enough elastic energy for a brittle fracture to occur. Note that neither mesh types produce a crack which fully propagates through the beam thickness.

In the case of the R2.50 simulations, both a structured mesh and a random mesh result in a brittle fracture mode as can be seen in Figure 8.15 (b). The crack paths in Figure 8.17 show that two out of six simulations produced realisations

of the stochastic fracture stress where the fracture stress values in the notch root were too low for fracture to occur during the analysis. Furthermore, the crack propagation in the structured mesh follows predominantly a vertical path that aligns with the pattern of the mesh similar to the R1.25 simulations. The random mesh, on the other hand, results in one simulation where the crack propagates slanted to the left and one simulation with a vertical crack direction. In both cases, the crack "zig-zags" from the non-uniform mesh. None of the R2.50 simulations produced a crack that propagated through the beam thickness.

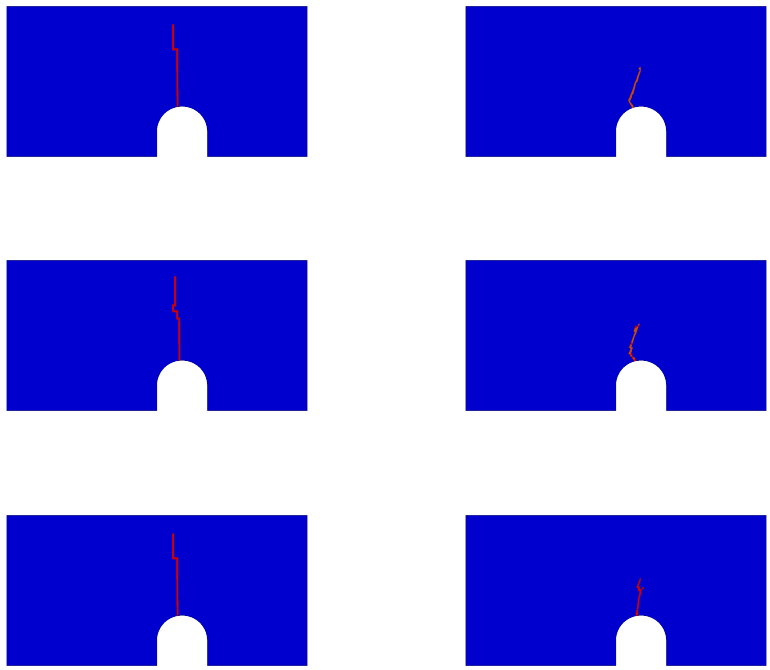

(a) Structured mesh **(b)** Random mesh

(c) Experiment

Figure 8.16: Crack paths from the last frame of the three repeat simulations of the R1.25 bending tests with **(a)** a structured mesh and **(b)** a random mesh. The cracks are visualised by plotting the damage variable, δ, in the reference configuration. The fracture path from an experiment is shown for reference in **(c)**.

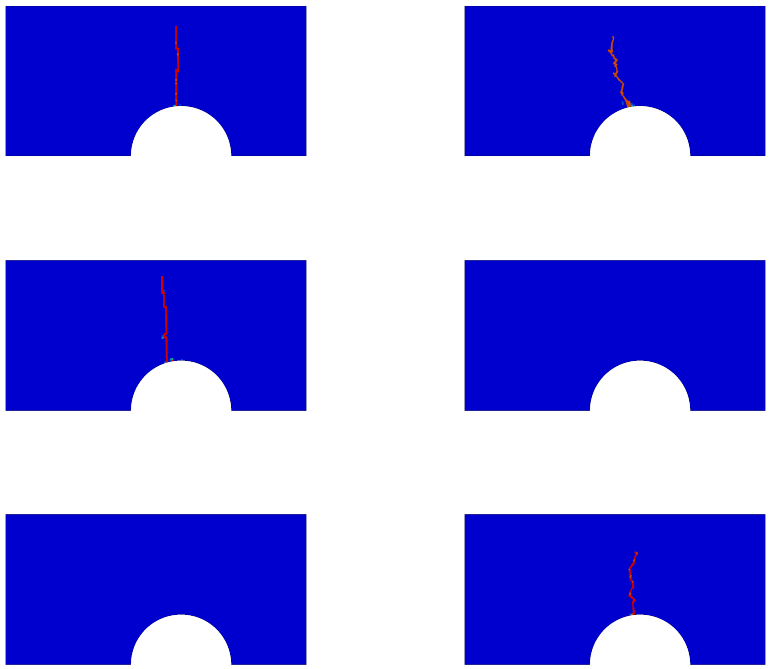

(a) Structured mesh **(b)** Random mesh

(c) Experiment

Figure 8.17: Crack paths from the last frame of the three repeat simulations of the R2.50 bending tests with **(a)** a structured mesh and **(b)** a random mesh. The cracks are visualised by plotting the damage variable, δ, in the reference configuration. The fracture path from an experiment is shown for reference in **(c)**.

8.3 Summary

- The validation tests were simulated with the calibrated constitutive model.
- Simulations of the quasi-static lattice compression tests agreed well with the experimental results, albeit with a slight overestimation of the plateau force. The largest discrepancy was observed in the $v = 300\,\mathrm{mm/min}$ simulations, which is attributed to the strain-rate sensitivity of the model not being calibrated for the strain rates occurring for this particular cross-head velocity.
- Simulations of the dynamic lattice compression tests captured the experimental trend where the lattice structure collapsed due to brittle fracture in the struts. The peak force and maximum displacement were also reasonably well captured considering the complexity of the experiments and simulations. The strain-rate sensitivity of the initial elastic stiffness was noticeably not captured due to the model's inability to describe this behaviour.
- Simulations of the three-point bending tests captured the overall shape of the force-displacement curves but the force at yield was underestimated for both specimen geometries. The underestimated force levels also led to fracture occurring too late, i.e., at a larger cross-head displacement than in the experiments. The fracture propagation was mesh dependent and neither a structured nor random mesh produced crack patterns that closely matched the experimental results.

9 Conclusions and outlook

This chapter wraps up the thesis by providing some concluding remarks and suggestions for further work.

9.1 Conclusions

This thesis presented a thorough characterisation of a commercial SLA resin. The effects of triaxiality, strain rate and print orientation were studied through tensile and compression tests on smooth and notched specimens. In addition, compression tests of octet-strut lattice structures and three-point bending tests of notched beams were performed to provide additional experimental data for the purpose of validating a constitutive model. Based on the experimental results, a constitutive model was formulated and implemented as a user material model in Abaqus/Explicit. The model was calibrated to the tensile tests and compression tests and validated against the lattice compression tests and three-point bending tests. The main findings from this work can be summarised as follows:

- The material exhibited a typical glassy polymer behaviour with an initial elastic response followed by inelastic flow, and strain hardening due to the orientation of the polymer chains. The flow stress of the material was found to be both strain-rate and pressure dependent, while the effect of the print orientation on the flow stress appeared to be negligible. The material behaviour differs from other glassy polymers, however, in the brittle fracture mode after significant inelastic deformation.
- Fracture occurred suddenly without any prior signs of strain localisation, which has a significant impact on the reliability of structures manufactured with such a material. A scatter in the fracture stress was observed in the tensile tests, where the largest scatter was observed in the smooth specimens and the smallest scatter was observed in the sharpest notched specimens. This observation, in turn, suggests that fracture in the material is governed by a size effect.
- The force-displacement curves from the quasi-static octet-strut lattice compression tests followed a typical cellular material behaviour with an initial elastic response followed by a plateau with near-constant force before reaching a densification stage where the force levels increase rapidly due to self-

contact between the lattice struts. The tests exhibited the same strain-rate sensitivity as in the tensile tests. The dynamic compression tests showed an extremely brittle response compared to the quasi-static tests as the high strain rates caused the struts of the structure to fracture before any significant inelastic deformation occurred.

- Three-point bending tests of beam specimens with off-centre notches exhibited the same general behaviour as the notch tensile tests. The specimens with the smallest notch radius exhibited higher force levels and lower ductility than the specimens with the largest notch radius. Both specimen types failed in a brittle fracture mode where the fracture initiated in the notch roots and propagated to the top of the beam with a slanted crack path.
- A material model consisting of a hyper-viscoelastic rheological model in conjunction with a stress-based fracture initiation criterion was implemented in Abaqus/Explicit. The numerical implementation was verified through an extensive study of the model's behaviour in single-element simulations for different stress states.
- The constitutive model was calibrated to the experimental results from the tensile and compression tests through inverse modelling. The overall shape of the stress-strain curves was accurately predicted by the model. The model captured the strain-rate- and pressure-dependent inelastic flow of the material and was able to predict the fracture initiation in the tensile tests. However, some viscoelastic aspects were not captured. The magnitude of the stress relaxation in the simulated relaxation test was underestimated by the model and the hysteresis in the loading/unloading tests was not accurately captured either. Furthermore, the model can not describe the strain-rate dependency of the initial elastic stiffness. The viscoelastic behaviour of the model could be improved by including additional viscous dashpots in the rheological model.
- The simulations of the lattice compression tests agreed well with the experimental results. The model captured both the deformation mode and the shape of the force-displacement curves of the quasi-static tests but the plateau force levels were slightly overestimated. For the simulations of the dynamic tests, the model was able to predict the brittle deformation mode observed in the experiments. The peak force and max. displacements were also reasonably captured, but a significant deviation between the simulated and experimental initial elastic stiffness was observed due to the model's inability to describe this behaviour.
- Simulations of the three-point bending tests captured the experimental trends, but the force at yield was underestimated for both specimen types.

The underestimation of the force levels led to fracture occurring at a larger cross-head displacement than observed experimentally. The scatter in the displacement at fracture was nonetheless captured by the fracture initiation model. Fracture propagation, however, was not accurately captured – neither with a structured mesh nor a random mesh around the fracture initiation zone.

The experimental campaign conducted in this work contributes to the research of SLA polymers, and other photopolymers, by providing a comprehensive experimental database for use in the validation of material models or for comparing with other polymers. The material model demonstrates how the classical hyper-viscoelastic modelling framework coupled with a fracture criterion can describe the most defining features of the studied resin: the inelastic flow and the brittle fracture mode.

9.2 Suggestions for further work

Although the presented work has contributed to the initial research objectives within the chosen scope, there are some aspects of both mechanical behaviour and constitutive modelling that would be interesting to study further. Some suggested topics for further work are:

- **Viscoelasticity**: The small-strain viscoelastic behaviour of the material was neglected in the constitutive model and no material tests were dedicated to studying this phenomenon. However, several of the numerical results in this work could be improved by including these effects. By taking additional relaxation times into account, i.e., adding additional viscoelastic networks to the rheological model, the unloading and relaxation behaviour of the model would most likely improve. The strain-rate dependency of the initial elastic stiffness would also be captured by such an extension of the model.
- **Fracture propagation**: Although the presented constitutive model was able to adequately predict fracture initiation, the fracture propagation in the sharpest notched tensile tests and in the three-point bending tests was not captured. The fracture model could be extended with a dedicated fracture propagation model to improve fracture propagation. Promising candidates for this task are classes of non-local fracture models such as gradient damage models [52, 53], phase field [54, 55] and eigen-erosion [56, 57].
- **Shear tests**: The effects of stress triaxiality were studied in the material test series, but no tests containing stress triaxiality in the interval (-1/3,1/3) were performed. A shear test, e.g. simple shear, could be performed to

provide experimental data where the stress triaxiality is approximately zero. The experimental data would be valuable for validating the constitutive model.

- **Comparison with a simpler model**: The constitutive model presented in this work is advanced and not straightforward to calibrate. It would be interesting to simulate the experiments with a simpler hypoelastic-viscoplastic model and compare the results from the presented constitutive model to assess whether or not the complexity of the presented model is necessary to adequately describe the studied material. A simple model could for instance be a non-associative viscoplastic Drucker-Prager model with isotropic hardening.
- **Thermomechanical behaviour**: The effects of temperature were out of scope for this thesis, but they are nonetheless critical for the mechanical behaviour of a polymer. Additional experiments at higher and lower temperatures should be performed to document the temperature sensitivity of the material.
- **SEM imaging**: We have postulated that fracture in the studied material is governed by defects in the material, but have not provided evidence of the existence of such defects. The fracture surfaces of fractured tensile specimens should be imaged with scanning electron microscopy (SEM) to study the fracture initiation zones for signs of these defects.

Bibliography

[1] N. A. Fleck, V. S. Deshpande and M. F. Ashby. 'Micro-architectured materials: past, present and future'. In: *Proceedings of the Royal Society A: Mathematical, Physical and Engineering Sciences* 466.2121 (2010), pp. 2495–2516. DOI: 10.1098/rspa.2010.0215.

[2] L. J. Tan, W. Zhu, K. Zhou, L. J. Tan, W. Zhu and K. Zhou. 'Recent Progress on Polymer Materials for Additive Manufacturing'. In: *Advanced Functional Materials* 30 (2020), p. 2003062. DOI: 10.1002/ADFM.202003062.

[3] *3D Printing Market Size, Share & Trends Analysis Report By Component (Hardware, Software, Services), By Printer Type, By Technology, By Software, By Application, By Vertical, By Region, And Segment Forecasts, 2022 - 2030*. Tech. rep. 978-1-68038-000-2. Grand View Research, Inc. 201 Spear Street 1100, San Francisco, CA 94105, United States: Grand View Research, 2021.

[4] J. Halary, F. Laupretre and L. Monnerie. *Polymer Materials: Macroscopic Properties and Molecular Interpretations*. Wiley, 2011.

[5] Formlabs. *Guide to Stereolithography (SLA) 3D Printing*. Accessed 05.05.2023. 2017.

[6] C. M. Cheah, J. Y. Fuh, A. Y. Nee, L. Lu, Y. S. Choo and T. Miyazawa. 'Characteristics of photopolymeric material used in rapid prototypes: Part II. Mechanical properties at post-cured state'. In: *Journal of Materials Processing Technology* 67.1-3 (1997), pp. 46–49. DOI: 10.1016/S0924-0136(96)02816-6.

[7] R. Hague, S. Mansour, N. Saleh and R. Harris. 'Materials analysis of stereolithography resins for use in Rapid Manufacturing'. In: *Journal of Materials Science* 39.7 (2004), pp. 2457–2464. DOI: 10.1023/B:JMSC.0000020010.73768.4a.

[8] D. L. Naik and R. Kiran. 'On anisotropy, strain rate and size effects in vat photopolymerization based specimens'. In: *Additive Manufacturing* 23 (2018), pp. 181–196. DOI: 10.1016/j.addma.2018.08.021.

[9] D. Miedzińska, R. Gieleta and E. Małek. 'Experimental study of strength properties of SLA resins under low and high strain rates'. In: *Mechanics of Materials* 141 (2020), p. 103245. DOI: 10.1016/j.mechmat.2019.103245.

[10] J. Martín-Montal, J. Pernas-Sánchez and D. Varas. 'Experimental characterization framework for SLA additive manufacturing materials'. In: *Polymers* 13.7 (2021), p. 1147. DOI: https://doi.org/10.3390/polym13071147.

[11] J. Saini, L. Dowling, J. Kennedy and D. Trimble. 'Investigations of the mechanical properties on different print orientations in SLA 3D printed resin'. In: *Proceedings of the Institution of Mechanical Engineers, Part C: Journal of Mechanical Engineering Science* 234.11 (2020), pp. 2279–2293. DOI: 10.1177/0954406220904106.

[12] C. Fry, A. Mihalko, R. Michael and D. Piovesan. 'Mechanical property determination of a stereolithographic resin subjected to compressive loading'. In: *ASME International Mechanical Engineering Congress and Exposition*. Vol. 52026. American Society of Mechanical Engineers. 2018, V003T04A008.

[13] R. Haward and G. Thackray. 'The use of a mathematical model to describe isothermal stress-strain curves in glassy thermoplastics'. In: *Proceedings of the Royal Society of London. Series A. Mathematical and Physical Sciences* 302.1471 (1968), pp. 453–472. DOI: 10.1098/rspa.1968.0029.

[14] H. Eyring. 'Viscosity, Plasticity, and Diffusion as Examples of Absolute Reaction Rates'. In: *The Journal of Chemical Physics* 4.4 (1936), p. 283. DOI: 10.1063/1.1749836.

[15] M. C. Boyce, D. M. Parks and A. S. Argon. 'Large inelastic deformation of glassy polymers. Part I: rate dependent constitutive model'. In: *Mechanics of materials* 7.1 (1988), pp. 15–33. DOI: https://doi.org/10.1016/0167-6636(88)90003-8.

[16] C. P. Buckley and D. C. Jones. 'Glass-rubber constitutive model for amorphous polymers near the glass transition'. In: *Polymer* 36 (17 1995), pp. 3301–3312. DOI: 10.1016/0032-3861(95)99429-X.

[17] T. A. Tervoort, R. J. Smit, W. A. Brekelmans and L. E. Govaert. 'A Constitutive Equation for the Elasto-Viscoplastic Deformation of Glassy Polymers'. In: *Mechanics of Time-Dependent Materials 1997 1:3* 1.3 (1997), pp. 269–291. DOI: 10.1023/A:1009720708029.

[18] J. S. Bergström and M. C. Boyce. 'Constitutive modeling of the large strain time-dependent behavior of elastomers'. In: *Journal of the Mechanics and Physics of Solids* 46.5 (1998), pp. 931–954. DOI: 10.1016/S0022-5096(97)00075-6.

[19] M. G. L. Anand. 'A theory of amorphous solids undergoing large deformations, with application to polymeric glasses'. In: *Internationa Journal of Solids and Structures* 40.6 (2003), pp. 1465–1487. DOI: 10.1016/s0020-7683(02)00651-0.

[20] M. Polanco-Loria, A. H. Clausen, T. Berstad and O. S. Hopperstad. 'Constitutive model for thermoplastics with structural applications'. In: *International Journal of Impact Engineering* 37.12 (2010), pp. 1207–1219. DOI: https://doi.org/10.1016/j.ijimpeng.2010.06.006.

[21] Z. Wu, A. A. Ogale, S. Ahzi, F. W. Paul and E. Hunt. 'Modeling of mechanical behavior of SLA parts'. In: *1997 International Solid Freeform Fabrication Symposium*. 1997.

[22] P. Zhang and A. C. To. 'Transversely isotropic hyperelastic-viscoplastic model for glassy polymers with application to additive manufactured photopolymers'. In: *International Journal of Plasticity* 80 (2016), pp. 56–74. DOI: 10.1016/j.ijplas.2015.12.012.

[23] S. Wang, Y. Ma, Z. Deng, K. Zhang and S. Dai. 'Implementation of an elastoplastic constitutive model for 3D-printed materials fabricated by stereolithography'. In: *Additive Manufacturing* 33 (2020), p. 101104. DOI: https://doi.org/10.1016/j.addma.2020.101104.

[24] C. Ling, A. Cernicchi, M. D. Gilchrist and P. Cardiff. 'Mechanical behaviour of additively-manufactured polymeric octet-truss lattice structures under quasi-static and dynamic compressive loading'. In: *Materials and Design* (2019). DOI: 10.1016/j.matdes.2018.11.035.

[25] F. Irgens. *Continuum Mechanics*. Springer Berlin Heidelberg, 2008.

[26] T. Belytschko, W. Liu, B. Moran and K. Elkhodary. *Nonlinear Finite Elements for Continua and Structures*. Wiley, 2013.

[27] J. S. Bergström. *Mechanics of solid polymers: theory and computational modeling*. William Andrew, 2015.

[28] S. N. Olufsen, M. E. Andersen and E. Fagerholt. 'μDIC: An open-source toolkit for digital image correlation'. In: *SoftwareX* 11 (2020), p. 100391. DOI: https://doi.org/10.1016/j.softx.2019.100391.

[29] I. Sobel. 'An Isotropic 3x3 Image Gradient Operator'. In: *Presentation at Stanford A.I. Project 1968* (2014).

[30] J. Johnsen, F. Grytten, O. S. Hopperstad and A. H. Clausen. 'Influence of strain rate and temperature on the mechanical behaviour of rubber-modified polypropylene and cross-linked polyethylene'. In: *Mechanics of Materials* 114 (2017), pp. 40–56. DOI: https://doi.org/10.1016/j.mechmat.2017.07.003.

[31] Formlabs. *Durable Resin v2 Technical Data Sheet*. United States, 2020.

[32] M. C. Messner. 'Optimal lattice-structured materials'. In: *Journal of the Mechanics and Physics of Solids* 96 (2016), pp. 162–183. DOI: https://doi.org/10.1016/j.jmps.2016.07.010.

[33] V. S. Deshpande, N. A. Fleck and M. F. Ashby. 'Effective properties of the octet-truss lattice material'. In: *Journal of the Mechanics and Physics of Solids* 49.8 (2001), pp. 1747–1769. DOI: 10.1016/S0022-5096(01)00010-2.

[34] T. Tancogne-Dejean, A. B. Spierings and D. Mohr. 'Additively-manufactured metallic micro-lattice materials for high specific energy absorption under static and dynamic loading'. In: *Acta Materialia* 116 (2016), pp. 14–28. DOI: https://doi.org/10.1016/j.actamat.2016.05.054.

[35] A. Reyes and T. Børvik. 'Low velocity impact on crash components with steel skins and polymer foam cores'. In: *International Journal of Impact Engineering* 132 (2019), p. 103297. DOI: https://doi.org/10.1016/j.ijimpeng.2019.05.011.

[36] E. Fagerholt. *eCorr v 4.0*. Accessed 20.02.2023.

[37] E. M. Arruda and M. C. Boyce. 'A three-dimensional constitutive model for the large stretch behavior of rubber elastic materials'. In: *Journal of the Mechanics and Physics of Solids* 41.2 (1993), pp. 389–412. DOI: 10.1016/0022-5096(93)90013-6.

[38] M. C. Boyce, G. G. Weber and D. M. Parks. 'On the kinematics of finite strain plasticity'. In: *Journal of the Mechanics and Physics of Solids* 37.5 (1989), pp. 647–665. DOI: 10.1016/0022-5096(89)90033-1.

[39] M. E. Gurtin and L. Anand. 'The decomposition F = FeFp, material symmetry, and plastic irrotationality for solids that are isotropic-viscoplastic or amorphous'. In: *International Journal of Plasticity* 21.9 (2005), pp. 1686–1719. DOI: 10.1016/j.ijplas.2004.11.007.

[40] P. H. Holmström, A. H. Clausen, T. Berstad, D. Morin and O. S. Hopperstad. 'A pragmatic orthotropic elasticity-based damage model with spatially distributed properties applied to short glass-fibre reinforced polymers'. In: *International Journal of Solids and Structures* 230-231 (2021), p. 111142. DOI: 10.1016/J.IJSOLSTR.2021.111142.

[41] Z. P. Bažant and B. H. Oh. 'Crack band theory for fracture of concrete'. In: *Matériaux et Constructions* 16.3 (1983), pp. 155–177. DOI: 10.1007/BF02486267.

[42] O. Knoll. 'A Probabilistic Approach in Failure Modelling of Aluminium High Pressure Die-Castings'. PhD thesis. Department of Structural Engineering, NTNU, 2015.

[43] J. Johnsen, A. H. Clausen, F. Grytten, A. Benallal and O. S. Hopperstad. 'A thermo-elasto-viscoplastic constitutive model for polymers'. In: *Journal of the Mechanics and Physics of Solids* 124 (2019), pp. 681–701. DOI: https://doi.org/10.1016/j.jmps.2018.11.018.

[44] J. F. Berntsen. 'Testing and modelling of multimaterial joints'. PhD thesis. Department of Structural Engineering, NTNU, 2020.

[45] G. Marsaglia and T. A. Bray. 'A Convenient Method for Generating Normal Variables'. In: *http://dx.doi.org/10.1137/1006063* 6.3 (2006), pp. 260–264. DOI: 10.1137/1006063.

[46] P. H. Holmström. 'An experimental and numerical study of the mechanical behaviour of short glass-fibre reinforced thermoplastics'. PhD thesis. Department of Structural Engineering, NTNU, 2019.

[47] J. Bergström and J. Bischoff. 'An advanced thermomechanical constitutive model for UHMWPE'. In: *The International Journal of Structural Changes in Solids* 2.1 (2010), pp. 31–39.

[48] L. Van Breemen, E. Klompen, L. Govaert and H. Meijer. 'Extending the EGP constitutive model for polymer glasses to multiple relaxation times'. In: *Journal of the Mechanics and Physics of Solids* 59.10 (2011), pp. 2191–2207. DOI: https://doi.org/10.1016/j.jmps.2011.05.001.

[49] L. Govaert, P. Timmermans and W. Brekelmans. 'The influence of intrinsic strain softening on strain localization in polycarbonate: modeling and experimental validation'. In: *Journal of Engineering Materials and Technology* 122.2 (2000), pp. 177–185.

[50] R. Raghava, R. M. Caddell and G. S. Yeh. 'The macroscopic yield behaviour of polymers'. In: *Journal of Materials Science* 8 (1973), pp. 225–232. DOI: https://doi.org/10.1007/BF00550671.

[51] V. Deshpande and N. Fleck. 'Isotropic constitutive models for metallic foams'. In: *Journal of the Mechanics and Physics of Solids* 48.6 (2000), pp. 1253–1283. DOI: https://doi.org/10.1016/S0022-5096(99)00082-4.

[52] S. Narayan and L. Anand. 'Fracture of amorphous polymers: A gradient-damage theory'. In: *Journal of the Mechanics and Physics of Solids* 146 (2021), p. 104164. DOI: https://doi.org/10.1016/j.jmps.2020.104164.

[53] Y. Mao and L. Anand. 'Fracture of elastomeric materials by crosslink failure'. In: *Journal of Applied Mechanics* 85.8 (2018). DOI: https://doi.org/10.1115/1.4040100.

[54] C. Miehe, M. Hofacker and F. Welschinger. 'A phase field model for rate-independent crack propagation: Robust algorithmic implementation based on operator splits'. In: *Computer Methods in Applied Mechanics and Engineering* 199.45 (2010), pp. 2765–2778. DOI: https://doi.org/10.1016/j.cma.2010.04.011.

[55] B. Yin and M. Kaliske. 'Fracture simulation of viscoelastic polymers by the phase-field method'. In: *Computational Mechanics* 65 (2020), pp. 293–309. DOI: https://doi.org/10.1115/1.4040100.

[56] A. Pandolfi, B. Li, M. Ortiz et al. 'Modeling failure of brittle materials with eigenerosion'. In: *Computational Modelling of Concrete Structures* 1 (2013), pp. 9–21.

[57] F. Stochino, A. Qinami and M. Kaliske. 'Eigenerosion for static and dynamic brittle fracture'. In: *Engineering Fracture Mechanics* 182 (2017), pp. 537–551. DOI: https://doi.org/10.1016/j.engfracmech.2017.05.025.

ISBN 978-82-326-7366-7 (printed ver.)
ISBN 978-82-326-7365-0 (electronic ver.)
ISSN 1503-8181 (printed ver.)
ISSN 2703-8084 (online ver.)

NTNU

Norwegian University of
Science and Technology